THE NONLINEAR DYNAMICS OF THE SEA BREEZE

A Thesis

by

KEVIN ROBERT WALTER

Submitted to the Office of Graduate Studies of
Texas A&M University
in partial fulfillment of the requirements for the degree of

MASTER OF SCIENCE

August 2004

Major Subject: Atmospheric Sciences

THE NONLINEAR DYNAMICS OF THE SEA BREEZE

A Thesis

by

KEVIN ROBERT WALTER

Submitted to the Office of Graduate Studies of
Texas A&M University
in partial fulfillment of the requirements for the degree of

MASTER OF SCIENCE

Approved as to style and content by:

John Nielsen-Gammon (Co-Chair of Committee)	Craig C. Epifanio (Co-Chair of Committee)
Benjamin Giese (Member)	Richard E. Orville (Head of Department)

August 2004

Major Subject: Atmospheric Sciences

ABSTRACT

The Nonlinear Dynamics of the Sea Breeze. (August 2004)

Kevin Robert Walter, B.S., Thomas More College

Co-Chairs of Advisory Committee: Dr. John Nielsen-Gammon
Dr. Craig C. Epifanio

The response of the land and sea breeze circulation to two highly simplified dynamical models is presented. The first dynamical model is the explicit specification of an oscillating interior heat source analogous to that from Rotunno (1983). Emphasis is placed on the variation of the response with heating amplitude and latitude. In addition, a weakly nonlinear analysis focuses on the dynamic forcing of nonlinear features such as a semi-diurnal gravity wave, fronts, and asymmetry in the magnitude of onshore and offshore flow. One surprising result is the identification of a cycle-mean surface divergence pattern at both 0º and 45º. At 45º, this divergence pattern is accompanied by a cycle mean shore-parallel response due to the Earth's rotation.

The second dynamical model is the explicit specification of an oscillating surface heat flux. Again, comparison is made between simulations at different heating amplitudes, and between simulations at different latitudes. To address changes in the solution due to the heating method itself, comparison is made between solutions from the surface heating method and solutions from the interior heating method. Finally, solutions across the planetary continuum are explored for critical latitude dependence in high-amplitude simulations.

DEDICATION

I'd like to dedicate this trying journey to those who instilled in me the belief that it was possible. Thank you first to my mother who, through actions, taught me to be an optimist, even when you feel like cursing the world. To my father, whose financial and moral support have goaded me to new heights. To my grandmother, whose straight country attitude has taught me what's really important in life. To my sister Erin, who always has a kind or encouraging word and always seems to be interested in what I'm doing. Finally, to my wife Abby, who believes in me more than I believe in myself, and who isn't afraid to say as much.

ACKNOWLEDGEMENTS

I'd like to primarily acknowledge my advisors, Dr. John Nielsen-Gammon, Dr. Craig Epifanio, and Dr. Benjamin Giese. Thanks to Dr. N-G for taking me on and giving me the freedom to succeed in both the research and community arenas here at Texas A&M. Thanks also to Dr. Craig Epifanio, who has provided me with an immense amount of guidance and positive support on a topic that I knew little or nothing about initially. In addition, his countless hours of description and patient re-description have guided me through the technical jungle of the numerical model. Thanks so much to all of the Atmospheric Science support staff – mainly (but not limited to) Jean Stanley, Mary Gammon, Barbara Straube, Rebecca Angel, Neil Smith, and Brandon Martin. Last but certainly not least, Pat Price, whose professional yet personal congeniality put Texas A&M at the top of the pile, and who, since my transfer, has provided the guidance necessary for me to succeed.

TABLE OF CONTENTS

LIST OF TABLES

LIST OF FIGURES

Figure Page

Figure Page

Figure Page

Figure Page

CHAPTER I

INTRODUCTION

The phenomenon of the sea breeze has been observed and documented for centuries. The sea breeze is of interest because it can have pronounced effects on a coastal environment, such as on the timing and location of near-coast precipitation. During the daytime hours, surface convergence due to the onshore sea breeze can initiate precipitation over land in a quiescent synoptic regime. Recent studies including data from remote sensing platforms such as infrared and microwave satellites are now suggesting that offshore rainfall distributions may also be influenced by the coastal circulation. For example, Figure 1 shows the difference between morning and evening special sensor microwave imager (SSM/I) mean rainfall rates for 1998, as derived by Imaoka and Spencer (2000). Note that the highest amplitude morning precipitation rates are found along coastlines, and not in open-ocean regions. Why the morning maximum is so much more pronounced near land is still under debate, but many hypothesize the coastal circulation to play a significant role.

Negri et al. (1994) use SSM/I data to document a nocturnal precipitation maximum parallel to the northeastern coast of Brazil, while noting a coast-parallel afternoon maximum just inland – a diurnal pattern consistent with the daytime sea breeze and nocturnal land breeze as convective triggering mechanisms. They also find an oscillation in precipitation intensity that continues southwestward from the coast, linking on the opposite side of the continent with the topography of the Andes

---

This thesis follows the style and format of the *Journal of the Atmospheric Sciences.*

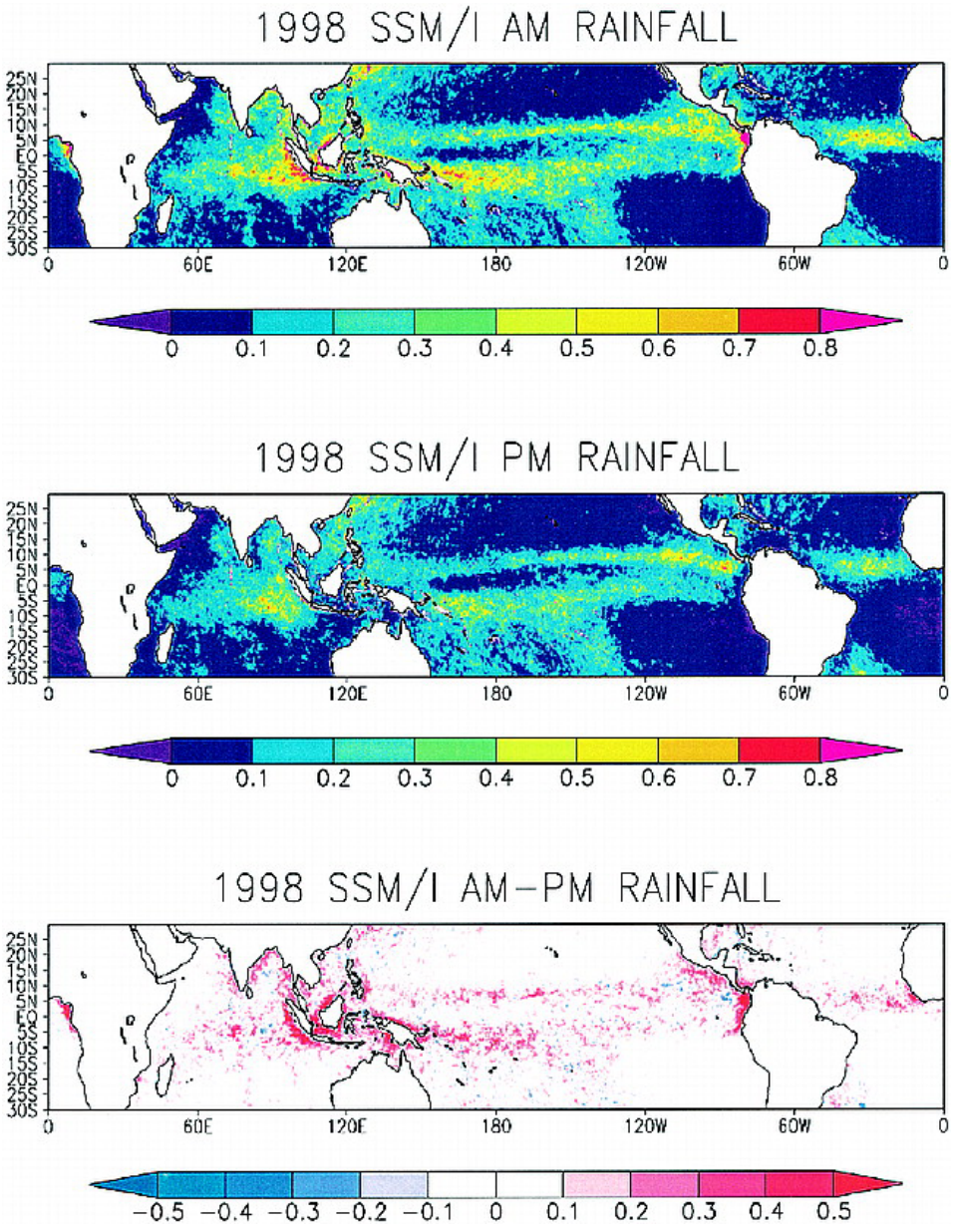

Fig. 1. SSM/I am rainfall (top), SSM/I pm rainfall (middle), SSM/I am/pm difference (bottom). From Imaoka and Spencer (2000) (their Fig. 5). Units are in mm h^{-1}

Mountains. In a subsequent study, Negri et al. (2000) comment on this phenomenon, explaining, "the pattern…suggests an analogy to that of waves in a string fixed at both ends. In this case, the 'ends' are the Andes to the southwest and the land-ocean boundary to the northeast." The cause of this wavelike structure is not well understood.

Yang and Slingo (2001) observed a signal in infrared brightness temperature values that propagated directly off the Indian coastline into the Bay of Bengal in the early morning hours. They comment, "a striking result…has been the extent to which the strong diurnal signal over land is spread out over the adjacent oceans, probably through gravity waves of varying depths. These coherent signals can be seen for several hundred kilometers and in some instances, such as over the Bay of Bengal, can lead to substantial diurnal variations in convection and precipitation." They note finally that through the redistribution of heat and moisture, precipitation in convective "hot spots" such as the Maritime Continent has a significant impact on global circulation.

The sea breeze also has important implications for urban air quality due to its impacts on atmospheric chemistry and pollutant transport in the coastal environment. As found by Nielsen-Gammon (2001), the direction of the large-scale flow is very important in determining the geographic distribution of ozone. For instance, periods with large-scale synoptic flow from the southeast (onshore in the Houston/Galveston area) can cause stagnation periods during the mid-morning, when offshore land-breeze flow is strong enough to cancel the opposing synoptic flow. Periods with shore-parallel or offshore flow can advect pollutants toward Galveston Bay during the morning hours, after which time they are advected back over the Houston area with the arrival of the

sea/bay breeze. Finally, periods with light winds have the potential to have "one day's emissions execute a complete loop and return to the city on the following day" as the local hodograph traces a circular path. Numerical modeling of the transport of pollutants in coastal regions requires correct simulation of the evolution of the planetary boundary layer and the associated thermally forced regional circulations. However, simulations using the 5th generation PSU/NCAR mesoscale model (MM5) exhibit maximum temperatures that are too low and minimum temperature that are too high (Nielsen-Gammon 2001). If this inaccuracy extends at any depth into the boundary layer, simulation of the thermodynamic profile, and thus of the local circulation, will be erroneous.

The sample set of works described above illustrates that there is ample motivation for wanting to understand the specific dynamical factors underlying coastal circulations. Further motivation is provided by the fact that current numerical simulations of the sea breeze typically display fundamental errors. Finding the source of errors such as these is often not simple, as operational models such as the MM5 or Weather Research and Forecasting Model (WRF) are very complex. In many cases, the method adopted for correcting such model errors is nudging. However, a more desirable approach is to find the cause of the problem and implement a permanent fix. For this to happen, the problem must first be understood at a fundamental and typically idealized level. With this in mind, the present thesis is aimed at a more thorough exploration of coastal circulation dynamics than that considered previously.

The overall objective of this work is to identify the processes governing the sea breeze in two simplified models: 1) the response to an oscillating heat source which is specified explicitly throughout the domain (hereafter referred to as "interior heating"), and 2) the response to an oscillating specified surface heat flux (hereafter referred to as "surface heating"). Emphasis is placed on the dependence of these two models on variations in latitude and heating amplitude.

The following chapter describes the body of previous work that most significantly affects the development of this investigation. A scale analysis for the problem is presented in Chapter III, along with a description of the numerical model to be used and a brief preliminary survey of model simulations. Chapter IV discusses simulations in which the diurnal heating is specified throughout the interior of the domain, particularly the dependence of the response on latitude and heating amplitude. Chapter V investigates the importance of the vertical distribution of heating. Conclusions are presented in Chapter VI.

CHAPTER II

PREVIOUS WORK

Among the scores of publications that in one way or another have addressed the sea breeze, a smaller set of works have dealt with the problem on a more fundamental level. These works can be separated into investigations of the problem using linear theory or nonlinear numerical modeling.

i) Linear Theory

Though the treatment of the linear theory of the sea breeze has a long history, there was no systematic investigation of solutions to the full set of linear equations until Rotunno (1983). Rotunno investigates the sea breeze as a response to a specified interior heating Q in a two-dimensional (x,z) coordinate plane, as represented by the linearized Boussinesq equations in the form

$$(1) \qquad \frac{\partial u}{\partial t} - fv = -\frac{\partial P}{\partial x} + F_x$$

$$(2) \qquad \frac{\partial v}{\partial t} + fu = F_y$$

$$(3) \qquad \frac{\partial w}{\partial t} = -\frac{\partial P}{\partial z} + b + F_z$$

$$(4) \qquad \frac{\partial b}{\partial t} + N^2 w = Q$$

$$(5) \qquad \frac{\partial u}{\partial x} + \frac{\partial w}{\partial z} = 0$$

where P is the Boussinesq disturbance pressure, b is the perturbation buoyancy, N^2 is the background static stability, and F_x, F_y, and F_z represent irreversible processes. The heating Q is specified to be a monochromatic function of time $H(x,z)\sin\omega t$, where

$$(6) \qquad H(\mathrm{x},\mathrm{z}) = A\left[\left(\frac{\pi}{2}\right) + \tan^{-1}\left(\frac{x}{x_0}\right)\right]e^{\left(-z/z_0\right)}$$

In (6), A is the heating amplitude (positive definite), and ω is the forcing frequency (diurnal for the sea breeze). The variables x_0 and z_0 are the horizontal and vertical length scales that control the width of the coastal transition zone and the depth of the heating, respectively. Rotunno sets x_0 to 10000 m and y_0 to 500 m. The function H (x,z) is such that the heating far offshore approaches zero. In the coastal transition zone, the heating increases to a maximum value (set by A) and remains roughly constant over land. This whole structure decays exponentially with height.

With this simple representation of the heating, the above equations can be combined to yield the following equation for the streamfunction ψ:

$$(7) \qquad N^2\frac{\partial^2\psi}{\partial x^2} + (f^2 - \omega^2)\frac{\partial^2\psi}{\partial z^2} = -\frac{\partial H}{\partial x}$$

Immediately, it is clear that the magnitude of f (the coriolis parameter) relative to ω has a profound effect on the nature of the solution. If f^2 is greater than ω^2 (latitudes poleward of 30°), the Coriolis parameter is dominant, making the solution evanescent and therefore bound primarily to the coastline. However, if f^2 is less than ω^2 (latitudes equatorward of 30°), the solution is wavelike, so that the response is not bound to the coast but rather consists of gravity waves traveling along ray paths that extend upward

and outward. At 30° latitude, $f^2 = \omega^2$ and the solution is singular and cannot be analyzed without the presence of other processes, such as friction. Rotunno (1983) hypothesizes that at other latitudes, friction would serve to lessen the phase difference between the poleward and equatorward solutions. Finally, linear theory predicts the aspect ratio of the response to be

$$(8) \qquad \frac{(f^2 - \omega^2)}{N}$$

and that the amplitude of the response will be proportional to the heating amplitude A.

To illustrate the difference in atmospheric response across 30° without the inclusion of friction, solutions to (7) analogous to those shown by Rotunno (1983) are presented in Figure 2 for the latitudes of 0º, 29º, 31º, and 45º. Note the drastic change in the nature of the response across the critical latitude of 30º as described. In addition, the aspect ratio of the gravity wave ray paths has dramatically decreased from the 0º to the 29º case, as predicted by (8).

The linear theory makes an interesting prediction about how the phase of the bulk atmospheric response varies with latitude. Via the linear Bjerknes circulation theorem, Rotunno found the circulation C to be

$$(9) \qquad C = \left[\frac{\sin(\omega t)}{(f^2 - \omega^2)} \right]_{z=0}^{\infty} \int [H(\infty, z) - H(-\infty, z)] dz$$

Note that if f^2 is greater than ω^2 (latitudes poleward of 30°), the circulation is in phase with the heating, resulting in onshore flow at the surface and upward motion over land

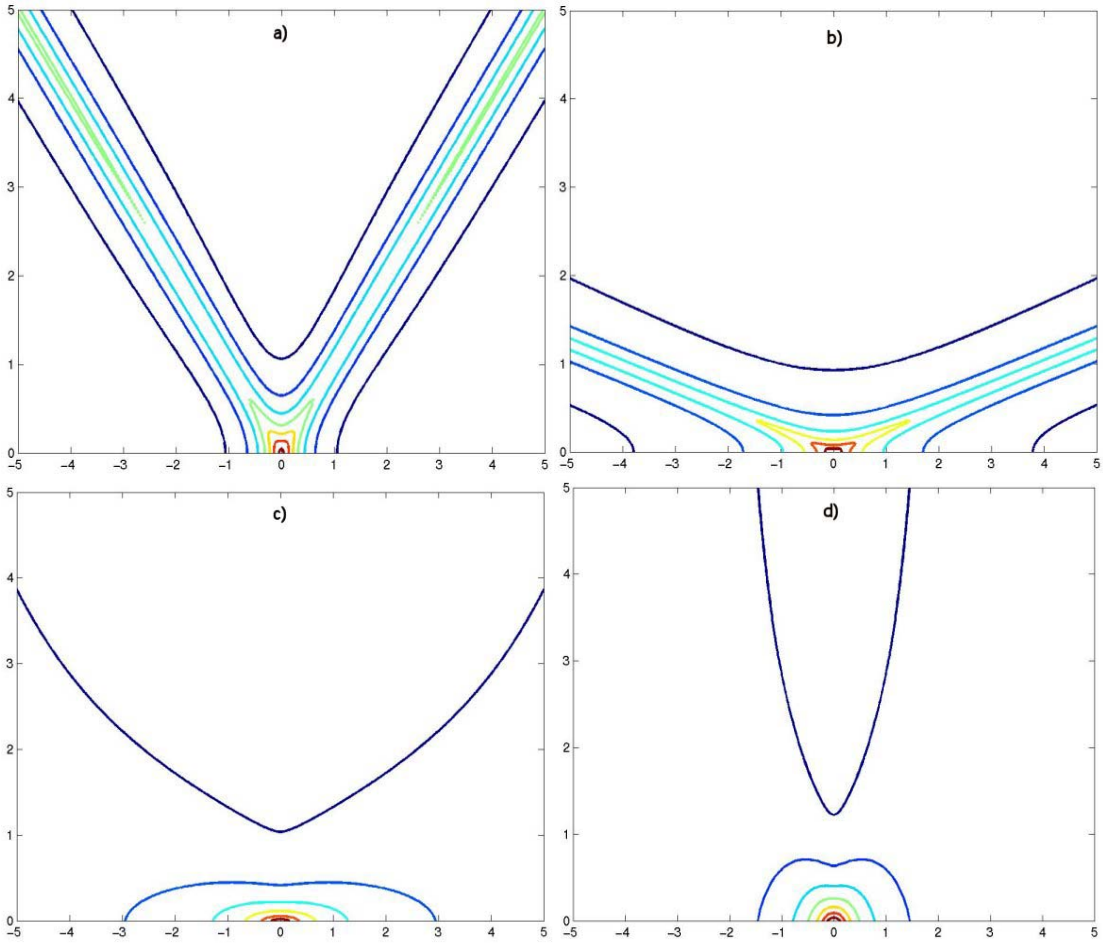

Fig. 2. Nondimensionalized u velocity analogous to the results of Rotunno (1983) for a) 0° at the end of the heating, b) 29º at the end of the heating, c) 31º at peak heating, and d) 45° at peak heating. Horizontal and vertical axes are nondimensional x and z, respectively. Contour interval is 0.25 for a) and d), and is 2.0 for b) and c).

during the day. Equatorward of 30°, where f^2 is less than ω^2, the circulation is exactly 180° out of phase with the heating, resulting in nocturnal onshore flow at the surface and offshore flow during the daylight hours. With regards to the coast-local response, the times depicted in Figure 2 correspond to the time of maximum horizontal shore-perpendicular wind. This is the time of peak heating at latitudes poleward of 30º, where u is in phase with the heating (and thus also with the circulation). However, the time necessary to depict the same field equatorward of 30º is the end of the heating, since u is out of phase with the forcing by $-\pi/2$ (and thus out of phase with the circulation by $\pi/2$).

Several studies of note expand the linear theory beyond the work of Rotunno. Dalu and Pielke (1989) studied the sea breeze first as a response to a step-function forcing of finite duration, then as a response to sinusoidal periodic forcing. They found that friction will likely prevent the occurrence of the gravity wave signal found by Rotunno (1983) equatorward of 30º. Even for small values of friction, the sea breeze at low latitudes may take days to begin radiating gravity waves. Niino (1987), in using linear theory to assess the horizontal extent of the land and sea breeze circulation, determined also that this inertial gravity wave must be drastically affected by the presence of non-zero viscosity.

ii) Numerical Modeling

Yan and Anthes (1987) test the linear predictions of Rotunno (1983) using a nonlinear numerical model. Besides the inclusion of nonlinearity, there are two main differences between the problems studied by Yan and Anthes (1987) and Rotunno

(1983). First, instead of specifying a simple heat source across the interior of the two-dimensional domain, Yan and Anthes specify the temperature across the bottom surface of the domain, forcing that to oscillate sinusoidally with time. In this setup, the transfer of heat across the lower boundary is then determined by the gradient in temperature between the surface and the first interior grid level. Second, Yan and Anthes include friction in their numerical simulations.

Yan and Anthes (1987) ultimately find some features that agree roughly with linear theory and some that do not. In an attempt to mitigate transients in the solution, they used 5-day variable averages at 3-hour intervals for their analysis. Three hours into the positive phase of the heating cycle, simulations at 20° and 45° show circulations that are 180º out of phase with each other. The atmospheric response at 20° shows evidence of a gravity wave signal, with an aspect ratio that roughly agreed with that predicted by linear theory. In addition, the disturbance at 20º exhibits a much larger horizontal and vertical extent than at 45°, where linear theory predicts the solution to be bound to the coast. Later in the heating phase, the solutions at both 20º and 45º show a classic sea breeze with onshore flow at the coast and upward motion over the land, while the large-scale gravity wave response evident earlier in the cycle has weakened. The authors attribute this similarity between latitudes towards the end of the heating cycle to the effects of the subgrid-scale turbulent eddy viscosity, which is largest during this phase of the heating. Interestingly, at 0º Yan and Anthes (1987) found that there is a net onshore bias to the circulation, which they attributed to the lack of a Coriolis force. In addition,

at 30º they found the circulation to steadily increase in intensity, hypothesizing this to be due to the resonant nature of the sea breeze at that latitude.

The results of a nonlinear numerical simulation by Niino (1987) depict a breakdown of the symmetries found in the linear solution with interior heating. This asymmetry was attributed by Niino mainly to the variation in the stratification. Due to the limits of the numerical model, the study was unable to address the effects of strong nonlinearity.

Previous work has taken great strides in describing the dynamic nature of the sea breeze. However, much of this previous work has only speculated on the cause of differences between linear theory and a more complex solution. The work presented here uses a nonlinear numerical model to address both the linear and nonlinear sea breeze problem. Highly idealized experiments are performed to investigate variations in heating amplitude, heating method, and latitude. As computational power is much more readily available in the present day, the simulations performed for this thesis are at a greater resolution than in the previous work described above.

CHAPTER III

SCALE ANALYSIS, MODEL DESCRIPTION, AND PRELIMINARY COMPARISON

i) Scale Analysis

In Chapter II, the two-dimensional linear equations of motion were presented. Those same equations including non-linear terms are:

$$\frac{\partial u}{\partial t} + u\frac{\partial u}{\partial x} + w\frac{\partial u}{\partial z} - fv = -\frac{\partial p}{\partial x} + S_u \tag{10}$$

$$\frac{\partial v}{\partial t} + u\frac{\partial v}{\partial x} + w\frac{\partial v}{\partial z} + fu = S_v \tag{11}$$

$$\frac{\partial w}{\partial t} + u\frac{\partial w}{\partial x} + w\frac{\partial w}{\partial z} = -\frac{\partial p}{\partial z} + b + S_w \tag{12}$$

$$\frac{\partial b}{\partial t} + u\frac{\partial b}{\partial x} + w\frac{\partial b}{\partial z} + N^2 w = Q + S_b \tag{13}$$

$$\frac{\partial u}{\partial x} + \frac{\partial w}{\partial z} = 0 \tag{14}$$

where S_u, S_v, S_w, and S_b represent parameterized, subgrid-scale mixing processes. For now, we assume that the diabatic heating Q is a specified function of time and space as in Rotunno (1983). In order to simplify these equations, we select space and time scales such that

$$t = \frac{1}{\omega}\hat{t} \qquad x = L\hat{x} \qquad z = H\hat{z}$$

where all "hatted" variables are of order of magnitude unity.

Either the horizontal or the vertical scale must be set by the heating. Rotunno (1983) argues that because the horizontal scale is much larger than the vertical scale, then the vertical scale must be set externally by the heating and the horizontal scale is set internally by the dynamics. We adopt this assumption as well, making H the depth scale of the heating and L the length scale to be determined internally. We continue choosing the scalings and say that

$$u = U\hat{u} \qquad v = V\hat{v} \qquad w = W\hat{w} \qquad p = P\hat{p} \qquad b = B\hat{\phi} \qquad Q = Q_0\hat{q}\ .$$

Assuming hydrostatic flow and these scale selections, equation (12) now yields

$$P \sim BH.$$

Similarly, from (14) we know that

$$\frac{U}{L} \sim \frac{W}{H}, \text{ or } U \sim L\frac{W}{H}.$$

Turning now to (13), we assume that the forcing Q will be similar in size to both $N^2 w$ and $\partial b/\partial t$. From this, it follows that

$$B \sim \frac{Q_0}{\omega} \quad \text{and} \quad W \sim \frac{Q_0}{N^2}.$$

Now, we consider equation (10) in the context that $\omega > f$ (equatorward of 30º). Here the dominant balance is between the local time tendency of the flow and the pressure gradient force:

$$\frac{\partial u}{\partial t} \sim -\frac{\partial P}{\partial x}$$

Substituting in our scale selections, this yields $U\omega \sim P/L$, or $P \sim LU\omega$. From the hydrostatic balance, recall that $P \sim BH$; substituting this into the above equation leaves $BH \sim LU\omega$, or $B \sim (L/H)U\omega$. To further simplify, we substitute $U \sim L(W/H)$ into the above equation, eventually yielding

$$(15) \qquad L \sim \frac{NH}{\omega}.$$

From these results, each variable of interest can be expressed in terms of the forcing Q_0:

$$u = \frac{Q_0}{N\omega}\hat{u} \qquad v = \frac{f}{\omega}\frac{Q_0}{N\omega}\hat{v} \qquad w = \frac{\omega}{N}\frac{Q_0}{N\omega}\hat{w} \qquad p = \frac{H}{\omega}Q_0\hat{p} \qquad b = \frac{Q_0}{\omega}\hat{\phi}$$

$$x = \frac{NH}{\omega}\hat{x} \qquad t = \frac{1}{\omega}\hat{t} \qquad z = H\hat{z} \qquad Q = Q_0\hat{q}.$$

Substituting these scaled variables back into (10) – (14) and neglecting the subgrid-scale viscous effects, the equations become:

$$(16) \qquad \frac{\partial \hat{u}}{\partial \hat{t}} + \varepsilon\left(\hat{u}\frac{\partial \hat{u}}{\partial \hat{x}} + \hat{w}\frac{\partial \hat{u}}{\partial \hat{z}}\right) - \frac{1}{R_o^{\,2}}\hat{v} = -\frac{\partial \hat{p}}{\partial \hat{x}}$$

$$(17) \qquad \frac{\partial \hat{v}}{\partial \hat{t}} + \varepsilon\left(\hat{u}\frac{\partial \hat{v}}{\partial \hat{x}} + \hat{w}\frac{\partial \hat{v}}{\partial \hat{z}}\right) + \hat{u} = 0$$

$$(18) \qquad \delta^2\left[\frac{\partial \hat{w}}{\partial \hat{t}} + \varepsilon\left(\hat{u}\frac{\partial \hat{w}}{\partial \hat{x}} + \hat{w}\frac{\partial \hat{w}}{\partial \hat{z}}\right)\right] - \hat{\phi} = -\frac{\partial \hat{p}}{\partial \hat{z}}$$

$$(19) \qquad \frac{\partial \hat{\phi}}{\partial \hat{t}} + \varepsilon\left(\hat{u}\frac{\partial \hat{\phi}}{\partial \hat{x}} + \hat{w}\frac{\partial \hat{\phi}}{\partial \hat{z}}\right) + \hat{w} = \hat{q}$$

$$\frac{\partial \hat{u}}{\partial \hat{x}} + \frac{\partial \hat{w}}{\partial \hat{z}} = 0 \qquad (20)$$

where the control parameters are

$$\varepsilon = \frac{Q_0}{N^2 \omega H} \qquad R_0 = \frac{\omega}{f} \qquad \delta = \frac{\omega}{N} = \frac{H}{L}.$$

Here, ε is the non-linearity control parameter. In all of our specified heating experiments we fix the Brunt-Väisälä frequency (N), the heating frequency (ω), and the heating depth (H) so that ε is directly determined by Q_0. It is worthy to note that the non-linearity parameter ε can be physically interpreted as a measure of how much the stratification changes relative to the background stratification due to the applied heating. The parameter R_0 is the Rossby number, a measure of the importance of inertia versus the Coriolis force. Finally, $\delta = H/L$ is the aspect ratio, a measure of the response's depth versus length. The standard variables can now be expressed in terms of these three control parameters

$$u = \varepsilon NH\hat{u} \qquad v = \frac{1}{R_0}\varepsilon NH\hat{v} \qquad w = \delta\varepsilon NH\hat{w} \qquad p = \varepsilon N^2 H^2 \hat{p} \qquad b = \varepsilon N^2 H\hat{\phi}.$$

These variables, expressed in nondimensionalized form, are then

$$\hat{u} = \frac{u}{\varepsilon NH} \qquad \hat{v} = \frac{R_0}{\varepsilon NH}v \qquad \hat{w} = \frac{w}{\delta\varepsilon NH} \qquad \hat{p} = \frac{p}{\varepsilon N^2 H^2} \qquad \hat{\phi} = \frac{b}{\varepsilon N^2 H}.$$

Currently, this scale analysis assumes a balance between the pressure gradient force and the local acceleration of the horizontal wind. North of 30º, this scale analysis should be repeated assuming a balance between the pressure gradient force and the Coriolis force. However, since f is never greater than 2ω, the present scaling will still be

reasonable there. Also, this scale analysis does not capture a latitude dependence of the response amplitude, particularly the resonance predicted by linear theory at 30º.

ii) Model Description

The numerical model used in this study is a variation of the non-hydrostatic, compressible Boussinesq solver described in Epifanio and Durran (2001). The model handles acoustic propagation by means of the split-time-step algorithm pioneered by Klemp & Wilhelmson (1978). The subgrid-scale eddy parameterization follows Lilly (1962). Vertical mixing in this parameterization is accomplished via a first order closure formulation that is Richardson number dependant.

The coast lies at the center of a two-dimensional domain of 1600 km horizontal extent, with 0 km < x < 800 km representing water, and 800 km < x < 1600 km representing land. To ensure the resolution of nonlinear features, the horizontal grid spacing is set to 2 km.

In the vertical, the domain is 6 km deep. Persson and Warner (1991) showed that consistency in horizontal and vertical grid spacing is important for avoiding the generation of spurious gravity waves by flows with slablike, sloping layers of ascent and descent. Consistency means that a numerical model must be able to resolve the vertical features that are physically related to resolvable horizontal features. From this, it is necessary for $\Delta z/\Delta x$ to be on the order of the aspect ratio (δ). This suggests a vertical grid spacing on the order of 15 m. As a compromise between consistency and computational feasibility, a vertical grid spacing of 25 m is chosen.

Note that this relatively small grid spacing near the lower boundary is also necessary to adequately represent the diffusive transfer of heat across the boundary in our simulations with specified heat flux. Because the majority of the atmospheric response occurs at low levels, we can afford to lose resolution near the domain top. A simple vertical grid stretching scheme is used to allow $\Delta z = 25$ m near the domain surface to stretch to $\Delta z > 60$ m near the upper boundaries (avg. $\Delta z = 43$ m), thus gaining computational efficiency.

Sponge layers at the boundaries are 250 km wide in the horizontal and 3 km deep in the vertical, yielding an effective simulation domain of 1100 km x 3 km. Sensitivity tests show that our basic results are not strongly sensitive to domain size and resolution.

Dalu and Pielke (1989) found the sea breeze to be of transient nature. In the absence of friction, it only asymptotically approached a steady state under periodic sinusoidal forcing on the order of days. Niino (1987) substantiates this, finding nonlinear simulations taking 7 days for the fractional change of domain-wide kinetic energy to change less than 0.5% from a chosen time to the same time one cycle later. As a compromise between "steadiness" and computational efficiency, model integrations in this work are over a period of 5 days. To mitigate the effect of transient waves resulting from the introduction of the heat source, the first day of each simulation is used as a linear ramping cycle.

In all cases, the atmosphere is initially at rest with a background thermodynamic profile of $N = 0.01$. A background viscosity is incorporated for a Reynolds number

$$R_e = \frac{\omega H^2}{K} \approx 100$$

However, K is Richardson number dependent with the subgrid scale eddy parameterization, thus decreasing the local Reynolds number in high-amplitude simulations. At the lower boundary, the background viscosity is constrained to maintain the background profile $N = 0.01$, and the simulations are free-slip.

As mentioned in Chapter I, the goal of this work is to describe the character of the sea breeze as a response to two highly simplified dynamical models – the interior heating case and the surface heating case. For the interior heating case, we experiment with an oscillating specified interior heating shape identical to that used by Rotunno (1983) and discussed in detail in Chapter II of this work. In previous work (Rotunno (1983), Yan and Anthes (1987)), the forcing has been specified to oscillate at $\sin(\omega t)$. In these experiments, for reasons to be discussed later, the heating shape will oscillate temporally at $\cos(\omega t)$. This change will shift the phase of the results in this work with respect to previous results by $\pi/2$. In other words, time 0 here corresponds to maximum heating (local noon), whereas time 0 in previous work corresponds to the start of the heating (local sunrise).

To test the effects of amplitude in the interior heating case, a set of simulations are computed in which the amplitude of the heating (Q_0) is varied. Because the relationship between the heating amplitude and the nonlinearity of the solution is

$$\varepsilon = \frac{Q_0}{N^2 \omega H}, \qquad (21)$$

and because N, ω, and H are all held constant within the simulation set, the nonlinearity of each simulation can be assigned through the choice of the constant Q_0. Simulations are done for 0º latitude at ε = 0.001, 0.01, 0.10, 0.20, 0.30, 0.40, and 0.50. When the heating shape corresponding to the highest heating amplitude (ε = 0.50) is integrated vertically to obtain energy per unit horizontal distance, it roughly corresponds to a one-dimensional surface flux of 100 W/m. Although actual observed surface fluxes are several times this value, preliminary results show atmospheric responses that have significantly departed from the small-amplitude linear solution, which is the desired result. Though simulations at higher amplitudes are feasible for the interior heating case, preliminary results also showed that in the surface heating case, the simulations quickly become nonlinear and computational efficiently rapidly deteriorates on this domain above ε = 0.50. Therefore, this experiment has been limited to that heating magnitude. Finally, to address the effects of latitude in the interior heating case, the simulations outlined above at 0º are computed and analyzed at 45º latitude.

The second idealized dynamical model to be tested is an oscillating specified surface heat flux. In these experiments, the effective heating shape is not specified explicitly, but essentially determined by model parameterizations. In this way, the heating shape is not constrained in time and space, but is allowed to evolve freely as it might in the real atmosphere. To investigate the effects of non-linearity in the surface heating case, an approach similar to that used in the interior heating instance is taken, where experiments are designed to make comparisons between simulations at varying heating amplitude and between simulations at varying latitude.

iii) Preliminary Comparison

To give the reader an indication of the scope of this work, included here is a preliminary comparison between the most basic and most complex simulations performed. Presentation here is strictly qualitative. The details of each simulation and a quantitative explanation of the progression from simple to complex will follow in subsequent chapters.

Figure 3 a and b shows vertical velocity from the simplest case – the low amplitude interior heating at 0º and 45º respectively. Vertical velocity from the most complex simulation – a high amplitude surface-heating simulation with a simple radiative damping parameterization - appears for 0º in Figure 3c, and at 45º in Figure 3d. Notably, the structure of the response at the equator has gone from a relatively simple gravity-wave (for the simplest case) to one containing complex near-coast frontal discontinuities (for the most complex case). At 45º, the simplest case (low amplitude) has no gravity wave response and maximum positive vertical velocity over land at the time of maximum heating, not at the end of the heating as in the equatorial case. Nonetheless, the most complex simulation at 45º closely resembles that at 0º.

This thesis will attempt to explain the differences observed here by starting with the simplest solution and adding degrees of complexity involving changes in the heating source amplitude and structure. Out of this progression will come a better understanding of the nonlinear dynamics that govern the sea breeze circulation.

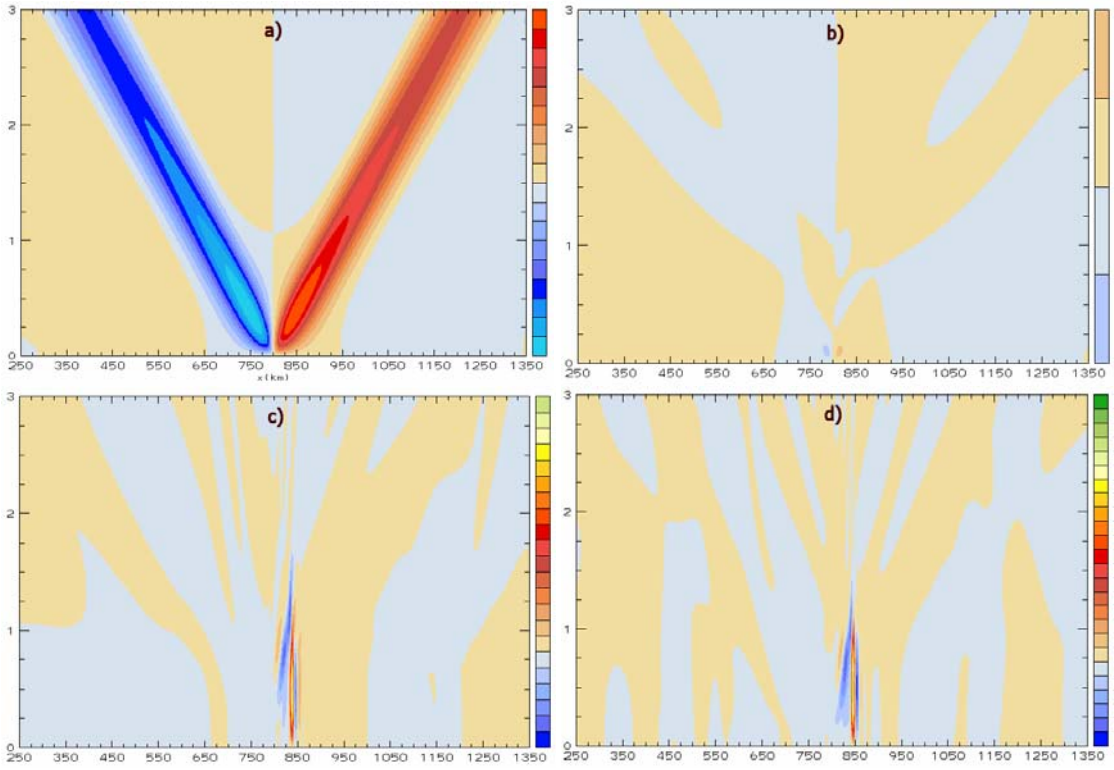

Fig. 3. Dimensional vertical velocities from the simplest model simulation at a) 0º and b) 45º; and the most complex model simulation at c) 0º and d) 45º. All figures at 4.25 days. Contour interval in c,d is 4 x 10^3 larger than that in a,b.

CHAPTER IV

INTERIOR HEATING

The interior heating model of the sea breeze involves explicitly specifying the amount and structure of heat added to the two-dimensional domain. The experiments in this chapter use a functional form of the interior heating identical to that used in Rotunno (1983):

$$Q(\mathrm{x},\mathrm{z},\mathrm{t}) = Q_0\left[\left(\frac{\pi}{2}\right) + \tan^{-1}\left(\frac{x}{x_0}\right)\right] e^{\left(-z/z_0\right)} \cos(\omega t)\,. \tag{22}$$

Here, as before, Q_0 represents the positive definite heating amplitude (which is linearly ramped from 0 to Q_0 during the first cycle), ω is the forcing frequency (diurnal for the sea breeze), x_0 = 10000 m, and z_0 = 500 m. This forcing is used to test the effects of amplitude and latitude variation on the sea breeze response. Prior to experimentation with this heating method, it is desirable to first verify that our numerical model, with the selected domain, can accurately reproduce the analytical results of Rotunno (1983). As discussed in Chapter III Section ii, the linearity of the model solutions here can be controlled via the magnitude of the heating Q_0. In this manner, linear solutions can be obtained with the non-linear numerical model by making Q_0 very small.

To match the Rotunno analytical solution, a zero-viscosity simulation was run at very low amplitude (ε = 1 x 10^{-8}) for 0º latitude. For this test only, the simulation was run to 10 cycles to maximize the steadiness of the solution. Figure 4 shows a direct comparison between the analytical results of Rotunno and the simulations using this

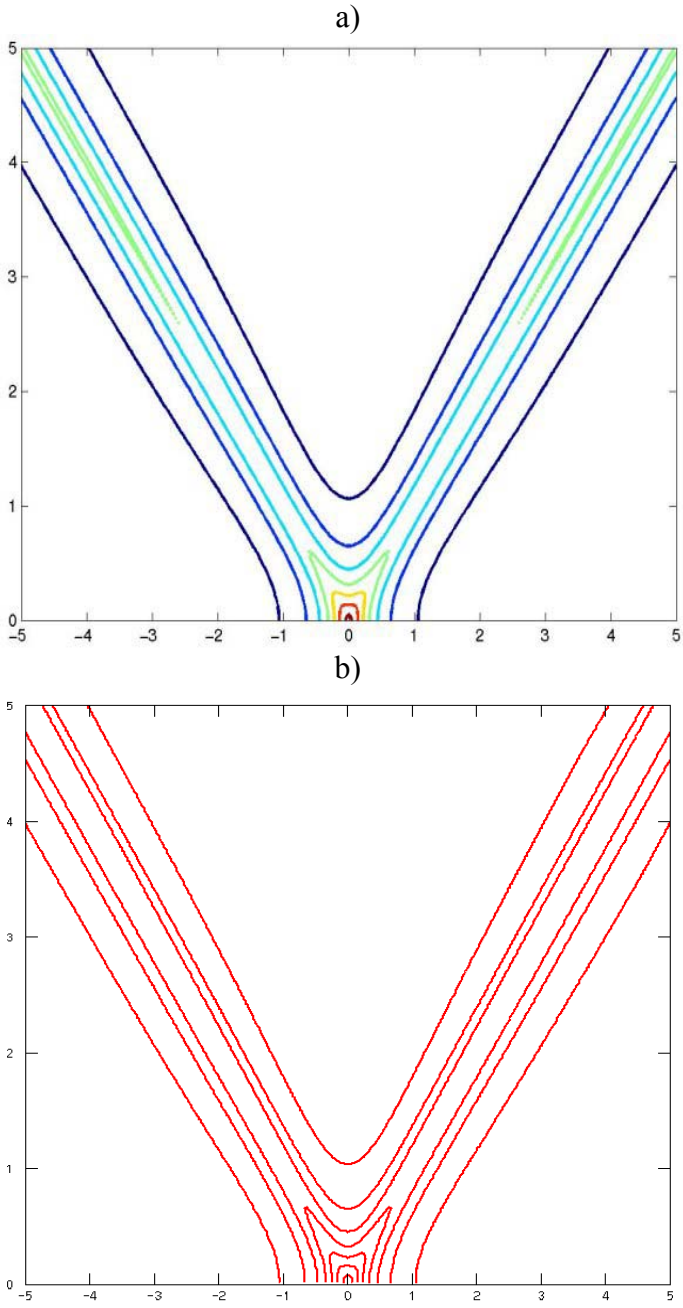

Fig. 4. Nondimensional u velocities at 8.25 days from a) Rotunno (1983) analytical solution and b) current model simulation. Horizontal and vertical axes are nondimensional x and z, respectively. Contour interval is 0.25.

model. Note that the small amplitude simulation matches the analytical results of linear theory almost exactly. Because the linear simulations match the analytical theory so well, this study will have the luxury of more quantitatively comparing complex simulations to the simple linear theory, something not previously done.

Since it is clear that this model can adequately capture the linear sea breeze response, the goal now is to begin building on the linear theory in an attempt to progress toward a more complex solution. All simulations in the remainder of this work have a small background viscosity. As discussed in Chapter III Section ii, this viscosity yields an effective Reynolds number of 100. Both Dalu and Pielke (1989) and Niino (1987) predict viscosity to damp the diurnal gravity wave signal with respect to the nonviscous case. Our work substantiates that prediction, as shown in the comparison of nondimensionalized vertical velocity from an inviscid low-amplitude interior heating simulation at 0º and an analogous viscous simulation with Reynolds number of 100 (Figure 5). The inclusion of viscosity has led to a 33% decrease in the strength of the maximum vertical velocities of the diurnal gravity wave signal local to the coast, a 25% domain-wide decrease in kinetic energy, and to a smoothing of slower wave harmonics. Niino (1987) found a damping that was larger than that found here. This is because Niino calculated damping due to a larger viscosity that was more indicative of vigorous eddy mixing. The magnitude of damping calculated in this work is that due to the effects of the background viscosity alone, where more vigorous eddy mixing is represented through parameterized processes.

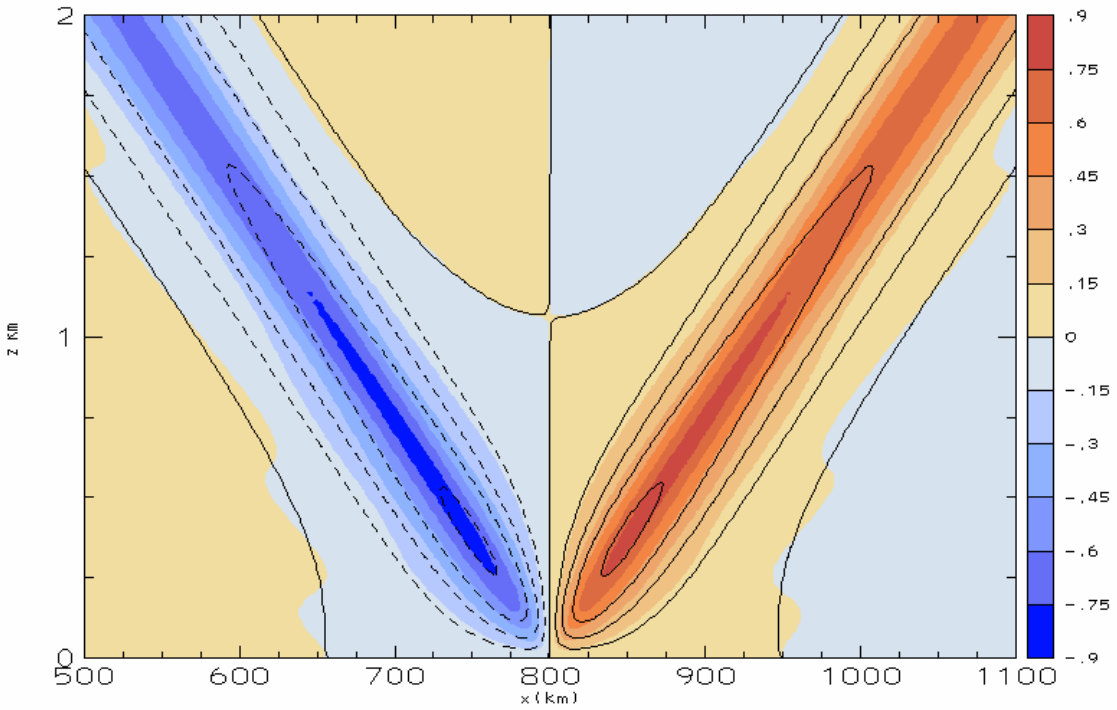

Fig. 5. Nondimensional vertical velocity from inviscid (color) and viscous (line) $\varepsilon = 0.001$ interior heating simulations at 0º latitude. Line contour interval is same as color fill.

i) Dependence on Heating Amplitude

The next experiment varies the heating amplitude for the equatorial interior heating case. Again, the nonlinearity of a simulation is controlled by the magnitude of the constant heating amplitude Q_0. As illustrated by Figure 6, various heating amplitudes lead to various magnitudes of nonlinearity. In the most linear simulation (Figure 6 a,b) the solution is the diurnal gravity wave response described by Rotunno (1983). In the weakly nonlinear simulation (Figure 6 c,d), faster, nonlinear wave modes that oscillate at a higher frequency and have larger aspect ratios (i.e. steeper phase lines) than the diurnal wave appear. In the strongly nonlinear simulation (Figure 6 e,f), frontal discontinuities begin to form and propagate away from the coastline.

Some quantitative measures of the progression to nonlinearity are illustrated in Figure 7. In this figure, the maximum is defined as the maximum surface quantity at any (x,t) throughout the simulation. Due to the symmetry in the linear solution, the maximum onshore *u* and maximum offshore *u* both occur at the coastline and are of equal magnitude at the two smallest amplitudes. However, as nonlinearity becomes more substantial, their intensities diverge, with the onshore sea breeze flow increasing faster than the linear rate. Not illustrated by this figure is the location of maximum onshore/offshore wind. In the low-amplitude simulation, the maximum onshore/offshore wind is located at the coast. In simulations with higher heating amplitude, the location of the maximum shifts onshore/offshore away from the coastline. At nonlinearity values $\varepsilon = 0.20$ and above, maximum *db/dx* surpasses the linear magnitude and increases more rapidly than the heating magnitude.

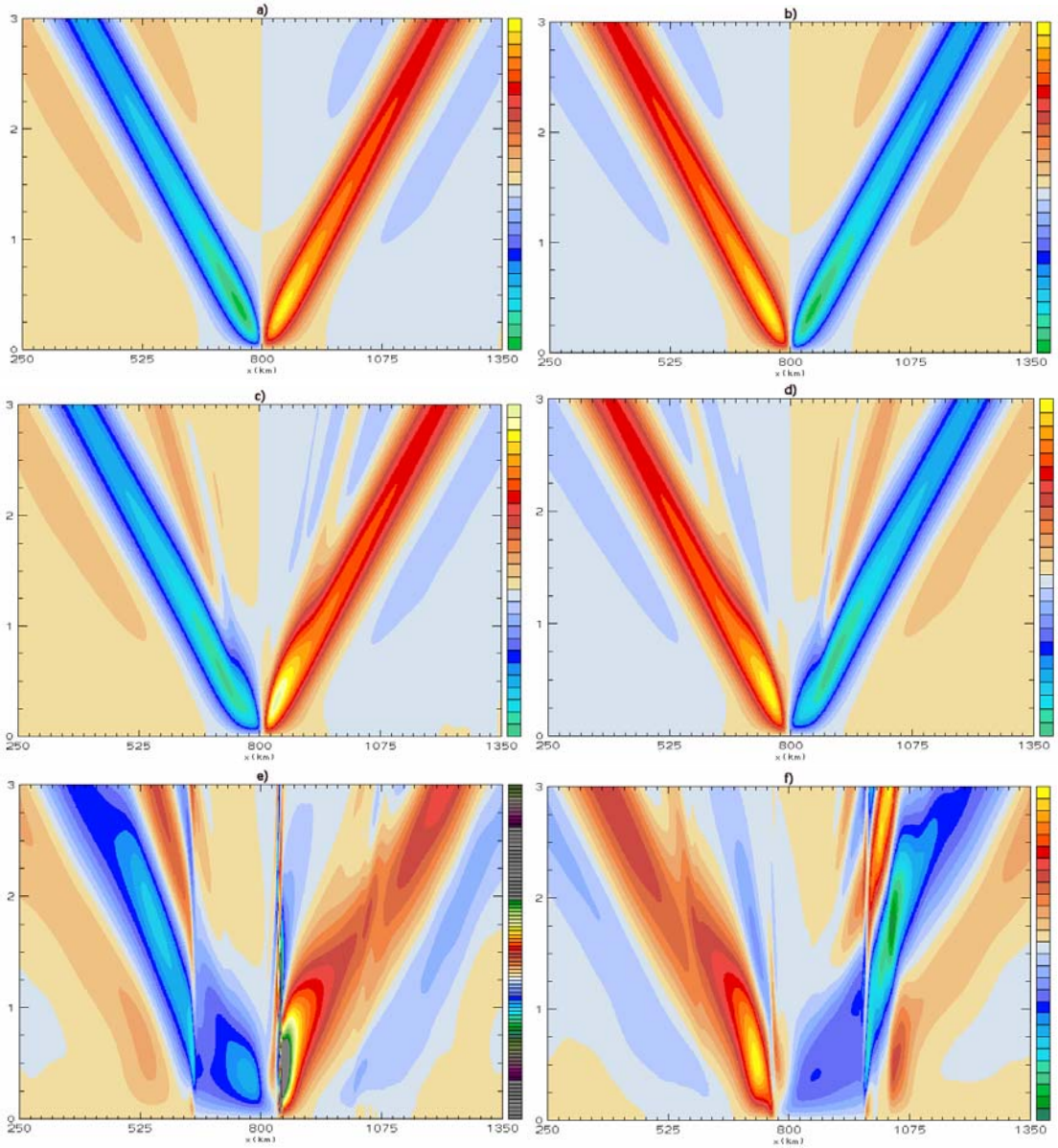

Fig. 6. Nondimensional vertical velocities for the 0º interior heating simulation a) ε = 0.001 at 4.25 days, b) ε = 0.001 at 4.75 days, c) ε = 0.10 at 4.25 days, d) ε = 0.10 at 4.75 days, e) ε = 0.50 at 4.25 days, f) ε = 0.50 at 4.75 days. Horizontal and vertical axes are x and z (respectively) in kilometers. Contour interval is constant throughout.

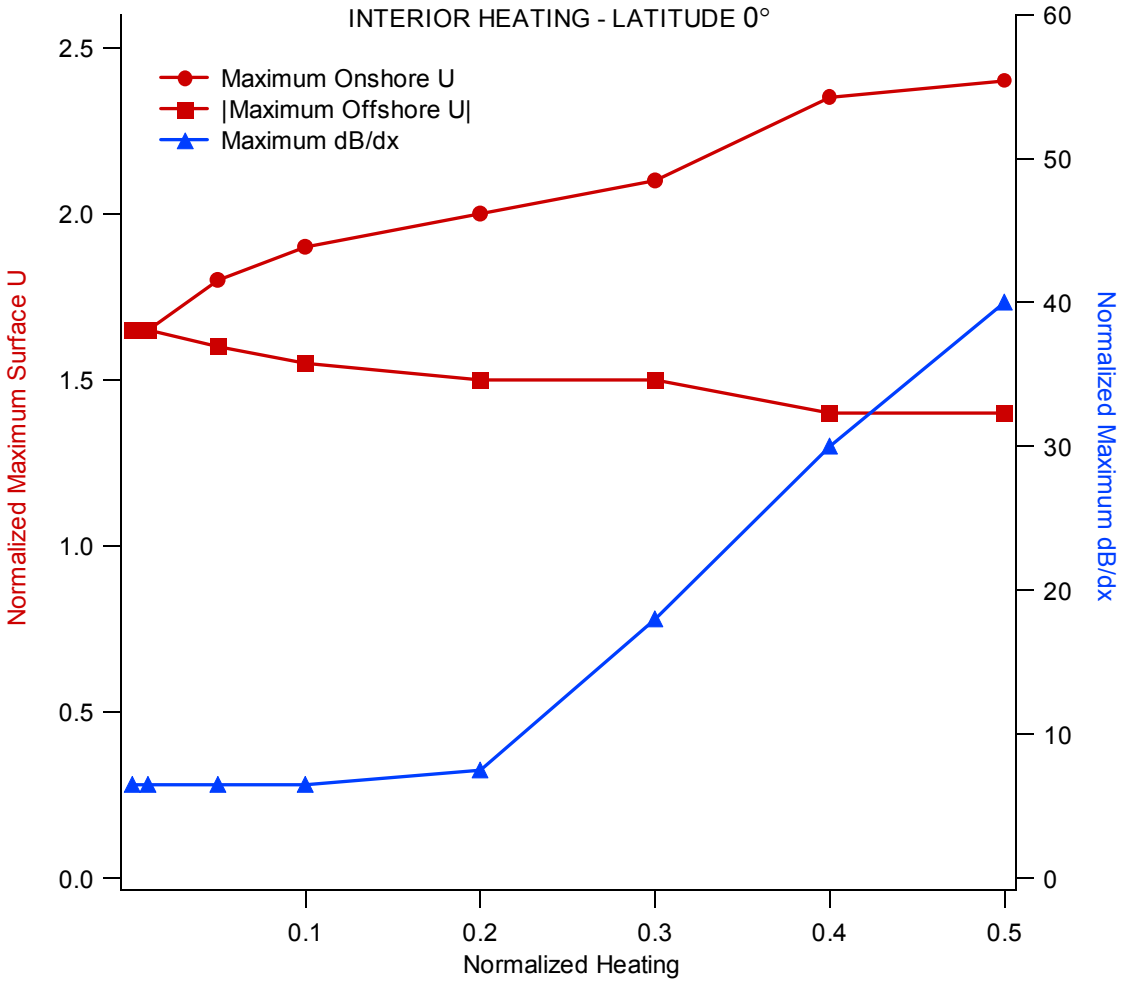

Fig. 7. Nondimensionalized maximum surface onshore u, offshore u, and db/dx vs. nondimensionalized heating (ε) for interior heating at 0º latitude.

To get a more quantitative handle on this progression to nonlinearity, we note that any nondimensionalized variable in any simulation can be expressed as a function of x, z, t, and the non-linearity parameter ε (since δ and R_0 are fixed). Using a Taylor series expansion, any of these solutions can theoretically be expressed as the summation of a base solution (linear theory) and subsequent corrections:

$$\hat{\phi}(\varepsilon) = \hat{\phi}(\varepsilon = 0) + \left.\frac{\partial \hat{\phi}}{\partial \varepsilon}\right|_{\varepsilon=0} \varepsilon + \frac{1}{2}\left.\frac{\partial^2 \hat{\phi}}{\partial \varepsilon^2}\right|_{\varepsilon=0} \varepsilon^2 + \ldots$$

$$= \hat{\phi}^{(0)} + \varepsilon\hat{\phi}^{(1)} + \varepsilon^2\hat{\phi}^{(2)} + \ldots \quad . \tag{23}$$

Recall that $\hat{\phi}$ here represents the nondimensionalized departure of buoyancy from the background state. Once this expansion is performed on each variable, it is substituted into the original set of nondimensionalized equations. For example, the $\hat{\phi}$ equation (19)

$$\frac{\partial \hat{\phi}}{\partial \hat{t}} + \varepsilon\left(\hat{u}\frac{\partial \hat{\phi}}{\partial \hat{x}} + \hat{w}\frac{\partial \hat{\phi}}{\partial \hat{z}}\right) + \hat{w} = \hat{q}$$

becomes:

$$\frac{\partial}{\partial \hat{t}}(\hat{\phi}^{(0)} + \varepsilon\hat{\phi}^{(1)} + \ldots) + \varepsilon\begin{pmatrix} \left(\hat{u}^{(0)} + \varepsilon\hat{u}^{(1)} + \ldots\right)\left(\frac{\partial \hat{\phi}^{(0)}}{\partial \hat{x}} + \varepsilon\frac{\partial \hat{\phi}^{(1)}}{\partial \hat{x}} + \ldots\right) + \\ \left(\hat{w}^{(0)} + \varepsilon\hat{w}^{(1)} + \ldots\right)\left(\frac{\partial \hat{\phi}^{(0)}}{\partial \hat{z}} + \varepsilon\frac{\partial \hat{\phi}^{(1)}}{\partial \hat{z}} + \ldots\right) \end{pmatrix} + \hat{w}^{(0)} + \varepsilon\hat{w}^{(1)} + \ldots = \hat{q} \tag{24}$$

Expanding this and grouping by ε coefficient leaves:

$$\frac{\partial \hat{\phi}^{(0)}}{\partial \hat{t}} + \hat{w}^{(0)} + \varepsilon\left[\frac{\partial \hat{\phi}^{(1)}}{\partial \hat{t}} + \hat{u}^{(0)}\frac{\partial \hat{\phi}^{(0)}}{\partial \hat{x}} + \hat{w}^{(0)}\frac{\partial \hat{\phi}^{(0)}}{\partial \hat{z}} + \hat{w}^{(1)}\right] + \varepsilon^2[\ldots] = \hat{q} \tag{25}$$

where higher order terms are neglected. For (25) to be true regardless of ε, every set of bracketed terms must necessarily equal zero. This simplification leads to the system:

(26) ε^0 system: $$\frac{\partial \hat{\phi}^{(0)}}{\partial \hat{t}} + \hat{w}^{(0)} = \hat{q}$$

(27) ε^1 system: $$\frac{\partial \hat{\phi}^{(1)}}{\partial \hat{t}} + \hat{w}^{(1)} = -\left(\hat{u}^{(0)} \frac{\partial \hat{\phi}^{(0)}}{\partial \hat{x}} + \hat{w}^{(0)} \frac{\partial \hat{\phi}^{(0)}}{\partial \hat{z}} \right)$$

where the forcing for each subsequent correction is the advection from the previous order. In this way, we can investigate the forcing of the second order response by analyzing fields from the linear solution.

When applied to each equation in the nondimensionalized equations of motion, we find that the first order linear advection terms responsible for forcing the second order nonlinear corrections are

$$-\hat{u}^{(0)} \frac{\partial \hat{u}^{(0)}}{\partial \hat{x}} \qquad -\hat{w}^{(0)} \frac{\partial \hat{u}^{(0)}}{\partial \hat{z}} \qquad -\hat{u}^{(0)} \frac{\partial \hat{v}^{(0)}}{\partial \hat{x}}$$

$$-\hat{w}^{(0)} \frac{\partial \hat{v}^{(0)}}{\partial \hat{z}} \qquad -\hat{u}^{(0)} \frac{\partial \hat{\phi}^{(0)}}{\partial \hat{x}} \qquad -\hat{w}^{(0)} \frac{\partial \hat{\phi}^{(0)}}{\partial \hat{z}}$$

Since most of the forcing is near the surface, we'll assume vertical motions are zero. At the equator, *v* is also zero. Thus, the only two advections left are

$$-\hat{u}^{(0)} \frac{\partial \hat{u}^{(0)}}{\partial \hat{x}} \quad \text{and} \quad -\hat{u}^{(0)} \frac{\partial \hat{\phi}^{(0)}}{\partial \hat{x}}$$

The first correction for non-linearity itself can be approximated as the subtraction of any nondimensionalized variable in the ε =0.001 solution from the ε =0.01 solution divided by (0.01-0.001). Figure 8 is the first correction of nondimensionalized *u* velocity. At an instant within the cycle (Figure 8a), one can clearly see the second

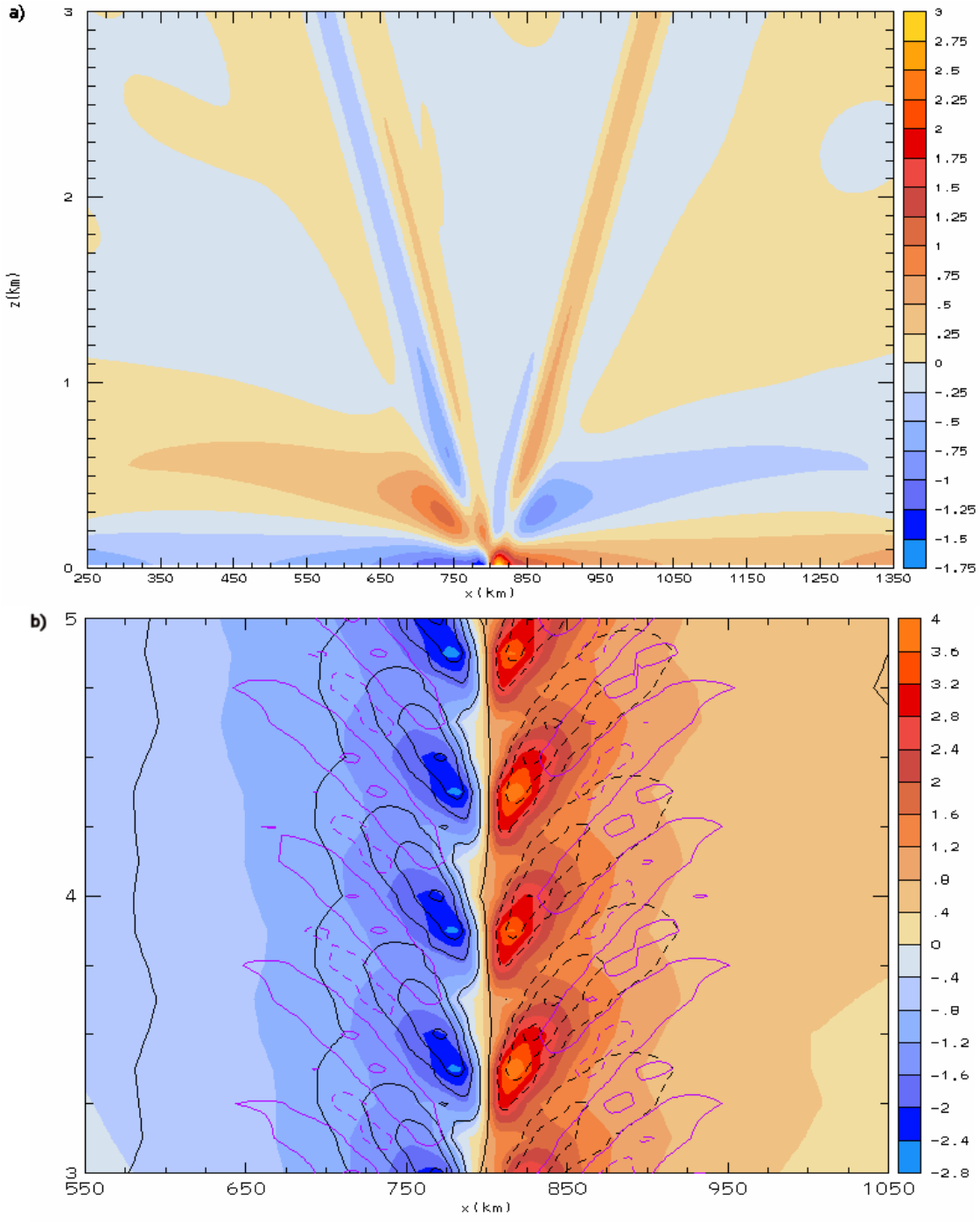

Fig. 8. First correction of nondimensional *u* velocity a) at cycle time 4.25, and b) from cycle 3 to cycle 5 at the surface (color fill), at 250m (black line), and at 1km (color line) altitude at 0º latitude. Solid line is positive, dash is negative. Line contour interval is same as color fill.

gravity-wave harmonic, which was shown in Figure 6 to be one of the first manifestations of nonlinearity. The semi-diurnal wave harmonic has twice the slope of the primary diurnal harmonic and thus oscillates with twice the frequency, and its presence in the nonlinear solution is not surprising. We have seen that the forcing terms for the first correction for nonlinearity are all product terms. Since each variable in the linear solution oscillates at frequency ω, multiplication of these variables yields a product that oscillates as a forcing for nonlinearity at 2ω. Thus the generation of the semi-diurnal wave harmonic.

Another result from the first correction in *u* comes from examining its time dependence. It appears that throughout one cycle (Figure 8b) the response is distinctly divergent at the surface and convergent aloft near 250 meters near the coast. Above this, the sign of the flow oscillates with the semi-diurnal gravity wave harmonic described previously.

Another feature of interest, found in the highest amplitude heating simulations, is the presence of a cycle-mean coastal cold anomaly that appears to be the result of near constant cold advection at the equatorial coast. The cold anomaly first develops as colder, more stable air is advected inland behind the sea breeze front near the end of the heating cycle (Figure 9). The pocket of cold air is then over land when the cooling cycle begins, making it cool more than air farther inland before being advected offshore again by the nighttime land breeze. From here, the cycle repeats and the anomaly persists. This feature is quantitatively found in the first nonlinearity correction for $\hat{\phi}$ averaged

over one cycle (Figure 10), with the maximum cycle-mean cold bias found directly at the coastline and decaying with distance.

Analyzing the magnitude of the six advective forcing terms for nonlinearity, we find that maximum $-u(db/dx)$ is about twice as large as maximum $-u(du/dx)$, and is about four times as large as the largest of the neglected *w* forcing terms which, because *w* is zero at the surface, reach a maximum at about 250 m altitude. We thus hypothesize the presence of the coastal cold anomaly, which itself is due to the cold bias in linear temperature advection at the coast, is the cause of the both the instantaneous and mean atmospheric responses seen in Figure 8.

Figure 11 depicts the $-u(db/dx)$ field, which is negative for cold advection. Consistent with linear theory, the cold advection during the day with the sea breeze is nearly equal in magnitude to the cold advection at night due to the land breeze, leading to a semi-diurnal pulsation of cold air advection, and thus a semi-diurnal oscillation in the intensity of the coastal cold anomaly.

To test the hypothesis that the semi-diurnal gravity wave and net surface divergence seen in Figure 8 are a result of this feature, we perform a model simulation where the heating shape

$$H(\mathrm{x},\mathrm{z},\mathrm{t}) = A\frac{\partial}{\partial x}\left(\tan^{-1}\frac{x}{x_0}\right)e^{\left(-z/z_0\right)}\cos(\omega t+\alpha)+B$$

$$= A\left(\frac{x_0}{x_0^2+x^2}\right)e^{\left(-z/z_0\right)}\cos(\omega t+\alpha)+B \qquad (28)$$

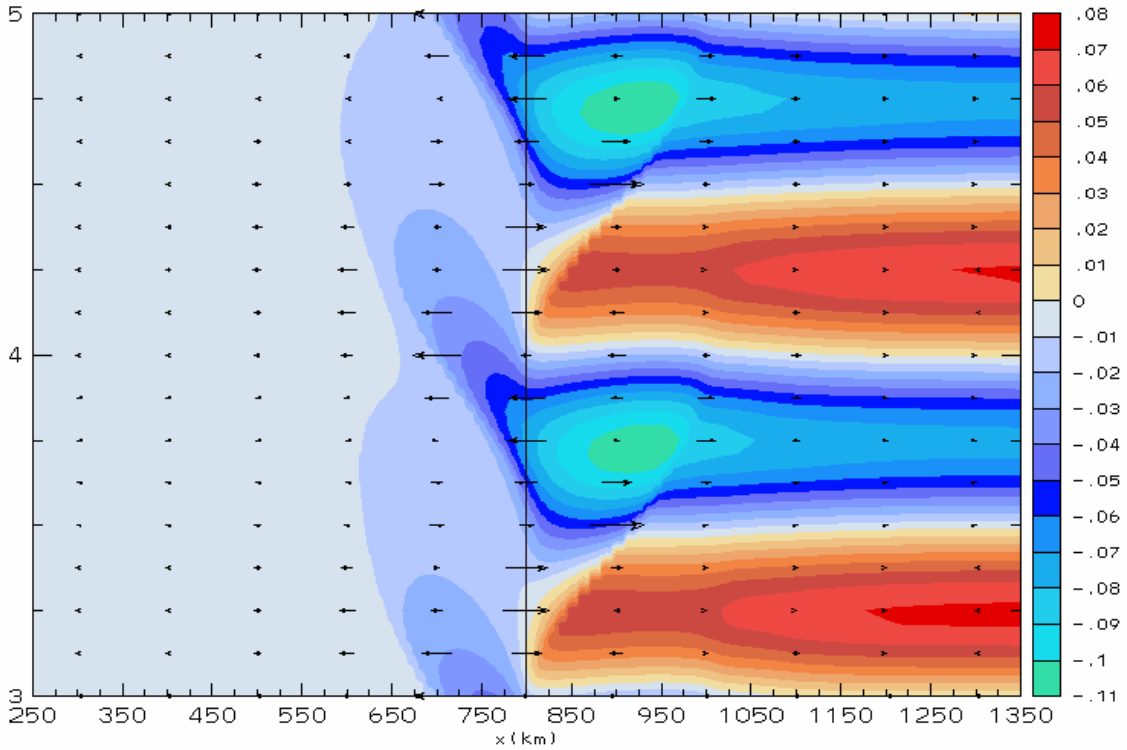

Fig. 9. Hovmoller diagram (days 3 to 5) of perturbation buoyancy (ϕ, color) and surface wind (arrow) for interior heating $\varepsilon = 0.50$, 0º latitude. Vertical line indicates coast.

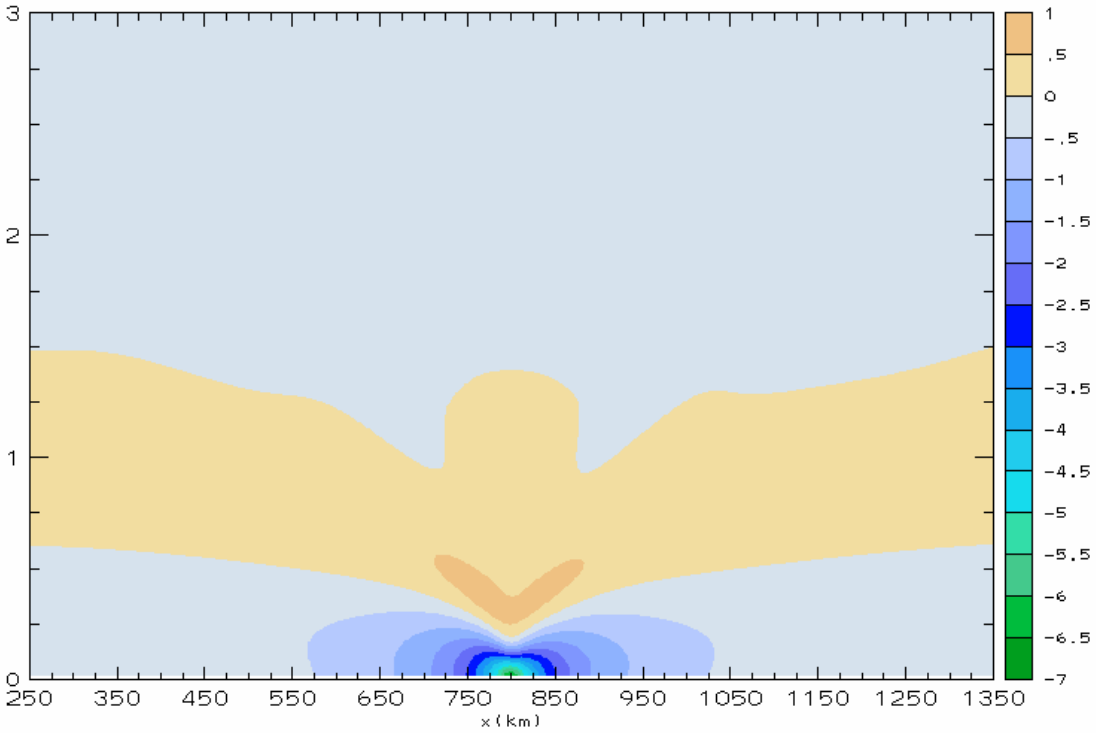

Fig. 10. First correction of nondimensional perturbation buoyancy averaged over days 4-5, 0º latitude. Axes are horizontal and vertical distance in km.

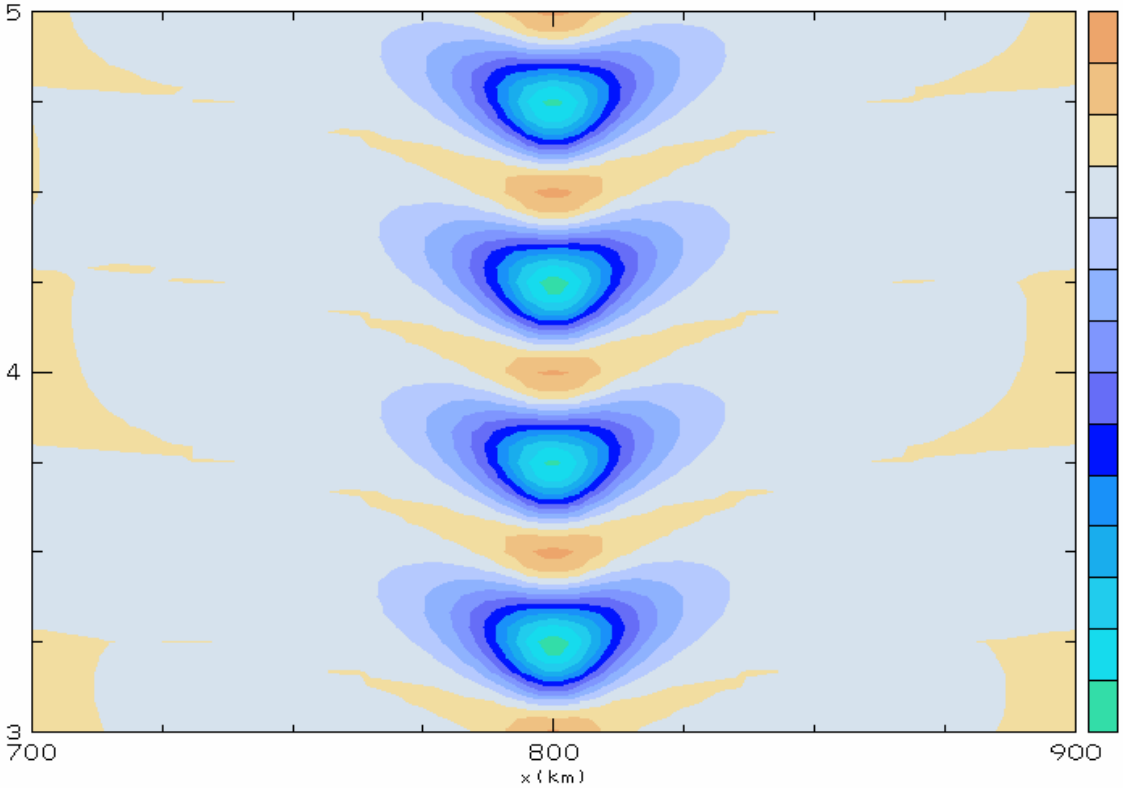

Fig. 11. Hovmoller diagram (cycles 3 to 5) of $-u(db/dx)$ for interior heating $\varepsilon = 0.001$, 0º latitude. Contour interval is 3 x 10^{-12}.

which approximately represents $-u(db/dx)$ in the x,z plane, is applied as a low-amplitude interior heat source oscillating at twice the diurnal frequency at 0º latitude. The phase α and bias B of the oscillation are set to mimic the oscillation of $-u(db/dx)$ seen in Figure 11. In this simulation, x_0 and z_0 are 10000 m and 500 m, respectively. Figure 12 shows the atmospheric response to this forcing at 4.25 days into the simulation. Not only is the semi-diurnal gravity wave harmonic captured, but the mean domain-wide surface divergence circulation is also evident as a response to this forcing. Thus, it is clear that near constant cold advection at the coast, and thus the development of a coastal cold anomaly, is significant in determining the character of the first correction for nonlinearity.

Applying this same method of successive corrections, we can obtain a measure of frontogenesis by finding the Lagrangian tendency of the linear flow field to increase the horizontal temperature gradient, i.e.

$$\frac{\mathrm{D}}{\mathrm{Dt}}\frac{\partial\theta}{\partial x}.$$

Substituting $\theta = b + N^2$, expanding the material derivative, and simplifying with respect to the forcing Q leaves

$$\text{(29a)} \qquad \frac{\mathrm{D}}{\mathrm{Dt}}\frac{\partial b}{\partial x} = \frac{\partial Q}{\partial x} - \frac{\partial u}{\partial x}\frac{\partial b}{\partial x} - \frac{\partial w}{\partial x}\left(N^2 + \frac{\partial b}{\partial z}\right)$$

To properly interpret whether or not the sign of each term in (29a) matches the tendency of the time rate of change of $\partial b/\partial x$, we multiply both sides of the equation by

$$\partial b/\partial x \,/\, \left|\partial b/\partial x\right|,$$

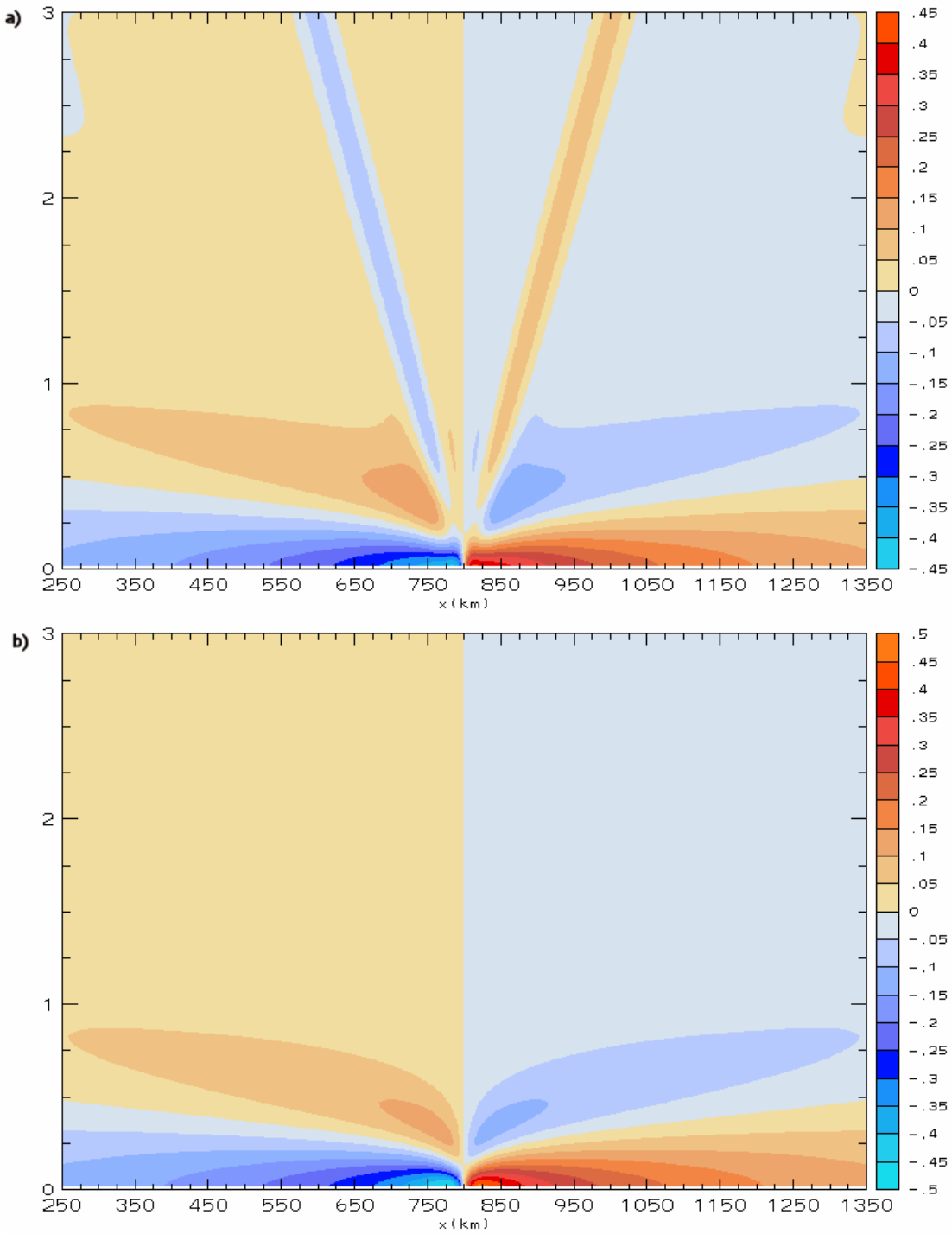

Fig. 12. Nondimensionalized u velocity as a response to semi-diurnal cold advection forcing a) at cycle time 4.25, and b) averaged over days 4-5. Vertical axis is height in km. 0º latitude.

thus yielding

$$\text{(29b)} \qquad \frac{\mathrm{D}}{\mathrm{Dt}}\left|\frac{\partial b}{\partial x}\right| = \left[\frac{\partial Q}{\partial x} - \frac{\partial u}{\partial x}\frac{\partial b}{\partial x} - \frac{\partial w}{\partial x}\left(N^2 + \frac{\partial b}{\partial z}\right)\right]\frac{\dfrac{\partial b}{\partial x}}{\left|\dfrac{\partial b}{\partial x}\right|}.$$

From (29b), the system of corrections for the Lagrangian frontogenesis equation is found to be

$$\text{(30)} \qquad \varepsilon^0 \text{ system:} \qquad \frac{\partial}{\partial t}\frac{\partial b^{(0)}}{\partial x} = \frac{\partial Q}{\partial x} - N^2\frac{\partial w}{\partial x}$$

$$\text{(31)} \qquad \varepsilon^1 \text{ system:}$$

$$\frac{\partial}{\partial t}\left|\frac{\partial b^{(1)}}{\partial x}\right| + u^{(0)}\frac{\partial}{\partial x}\left|\frac{\partial b^{(0)}}{\partial x}\right| + w^{(0)}\frac{\partial}{\partial z}\left|\frac{\partial b^{(0)}}{\partial x}\right| = -\frac{\partial u^{(0)}}{\partial x}\left|\frac{\partial b^{(0)}}{\partial x}\right| - \left(\frac{\partial w^{(0)}}{\partial x}\frac{\partial b^{(0)}}{\partial z} + N^2\frac{\partial w^{(0)}}{\partial x}\right)\frac{\dfrac{\partial b^{(0)}}{\partial x}}{\left|\dfrac{\partial b^{(0)}}{\partial x}\right|}.$$

The three terms on the right-hand side of (31) can be interpreted as (respectively) the contraction of a temperature gradient by convergence of the horizontal wind, the tilting of a vertical perturbation buoyancy gradient, and the tilting of the specified background atmospheric profile. The advection terms on the left-hand side of (31) do not contribute to Lagrangian frontogenesis.

Since we are most concerned with frontogenesis at the surface, and since vertical velocity at the surface is zero, the following analysis will neglect the terms in (31) that involve *w*. This leaves the contraction term (hereafter referred to as "contraction"),

$$-\frac{\partial u^{(0)}}{\partial x}\left|\frac{\partial b^{(0)}}{\partial x}\right|$$

to describe the Lagrangian frontogenesis tendency. Figure 13 shows this forcing term at the surface of the domain in an equatorial small-amplitude interior heating simulation. Strictly for comparison, the advective term (hereafter referred to as "advection")

$$u^{(0)} \frac{\partial}{\partial x} \left| \frac{\partial b^{(0)}}{\partial x} \right|$$

is also plotted so that some comment can be made regarding the net local tendency of the temperature gradient at any time. At peak heating (Figure 13a), contraction of the isentropes is underway. Three hours before sunset, contraction reaches a maximum, though it is still relatively large at the end of the heating (Figure 13c), when the coastal onshore flow at 0º is largest.

At night, a similar pattern develops in the offshore regime, with maximum frontogenesis occurring near the end of the cooling. Interestingly, the advection term at 0º is three hours out of phase with the contraction term during some parts of the cycle. Finally, above the surface the tilting terms (not shown) are nonzero. However, they contribute to frontogenetic forcing at one order of magnitude smaller than the horizontal contraction and advection terms. Since frontogenetic forcing occurs even within the small-amplitude solution, we must conclude that some tendency to contract the isentropes exists at all heating amplitudes. However, it is only at approximately $\varepsilon = 0.20$ (as seen in Figure 7), that its magnitude exceeds the linear gradient.

At this point, it must be said that the weakly nonlinear analysis can only tell us the nonlinear tendencies of the solution, and cannot describe the full nature of nonlinearity itself. To illustrate this point, we recall that nondimensional db/dx can be

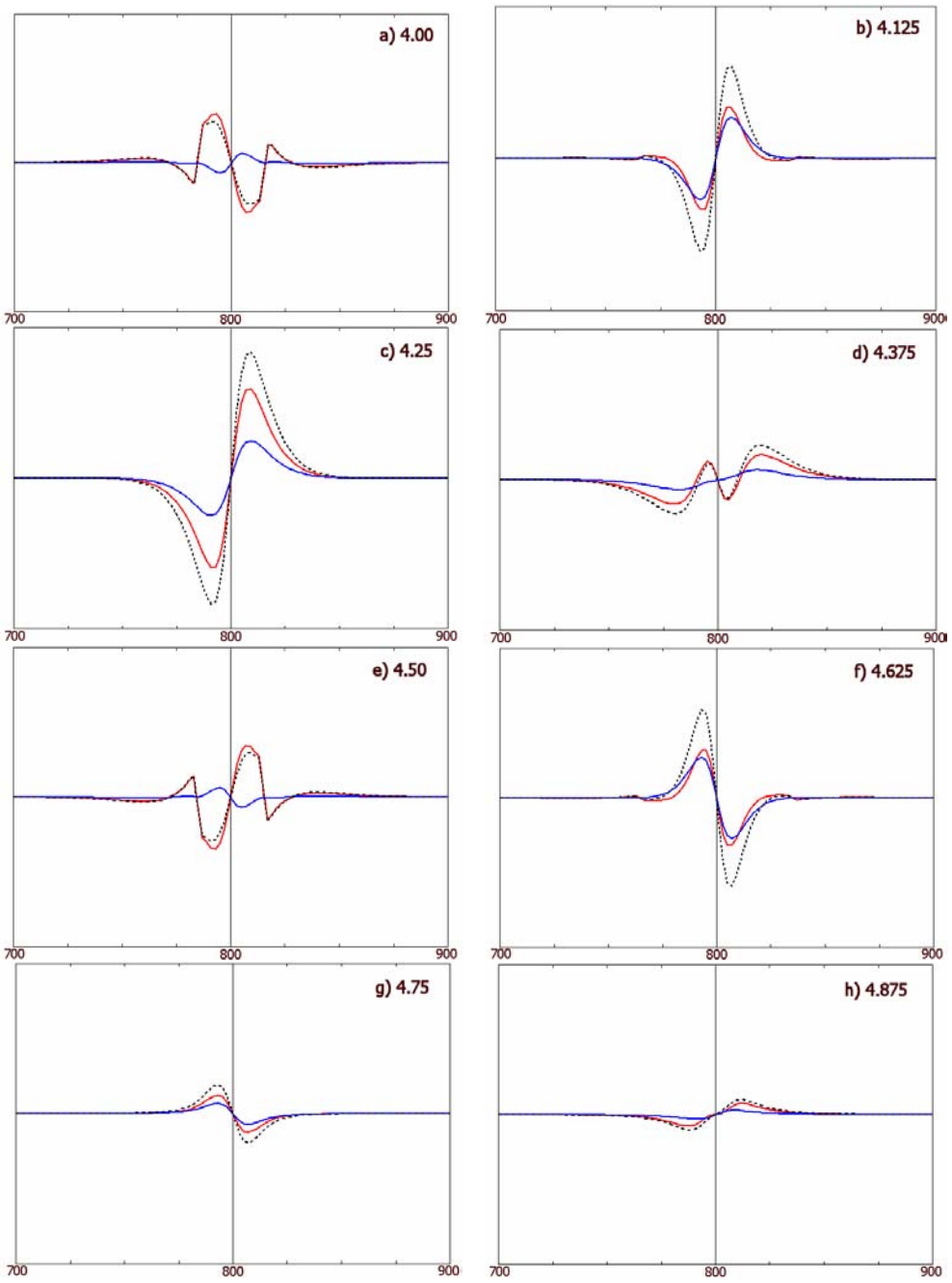

Fig. 13. Surface frontogenetic forcing in the interior heating $\varepsilon = 0.001$ simulation due to advection (red), and contraction (blue), at day a) 4.00, b) 4.125, c) 4.25, d) 4.375, e) 4.50, f) 4.625, g) 4.75, and h) 4.875. The sum of the forcing terms is black dash. 0º latitude. Vertical line indicates coast. Vertical axis scale is 1.5×10^{-15}.

expanded as a Taylor series to

$$\frac{\partial \hat{b}}{\partial \hat{x}} = \left(\frac{\partial \hat{b}^{(0)}}{\partial \hat{x}} + \varepsilon \frac{\partial \hat{b}^{(1)}}{\partial x} + \ldots \right).$$

From this, we can get an estimation for $d\hat{b}/d\hat{x}$ at any value of ε from the linear solution and first correction. The linear term plus the first correction predictions $d\hat{b}/d\hat{x}$ at ε = 0.50 to be about 15. From Figure 7, the actual simulated value of $d\hat{b}/d\hat{x}$ at ε = 0.50 is around 40. So again, these first corrections yield insight into the nonlinear tendencies of the solution, but there are clearly more complex higher order terms that contribute significantly to the total nonlinearity of the system.

Scores of observational studies indicate that fronts (nonlinear entities) are a distinctive part of the sea breeze phenomenon. Figure 14 illustrates the importance of such frontal structures in determining the near-coast circulation through comparison to a small-amplitude solution. In the near-coast regime of the high-amplitude solution, where nonlinear features such as frontal discontinuities dominate the response, linear theory predicts the general phase of the solution, but of course does not predict the magnitude or timing of the maximum vertical motion or the vertically propagating non-hydrostatic gravity waves associated with passing fronts (Figure 14a). In the far-field, linear theory continues to predict the atmospheric response well (Figure 14b), generally predicting both the magnitude and the phase of the response.

Finally, a common bulk measure of the atmospheric response to the heating is circulation. Via Stokes's theorem, the circulation of a two-dimensional region is calculated as the total vorticity of the region, or

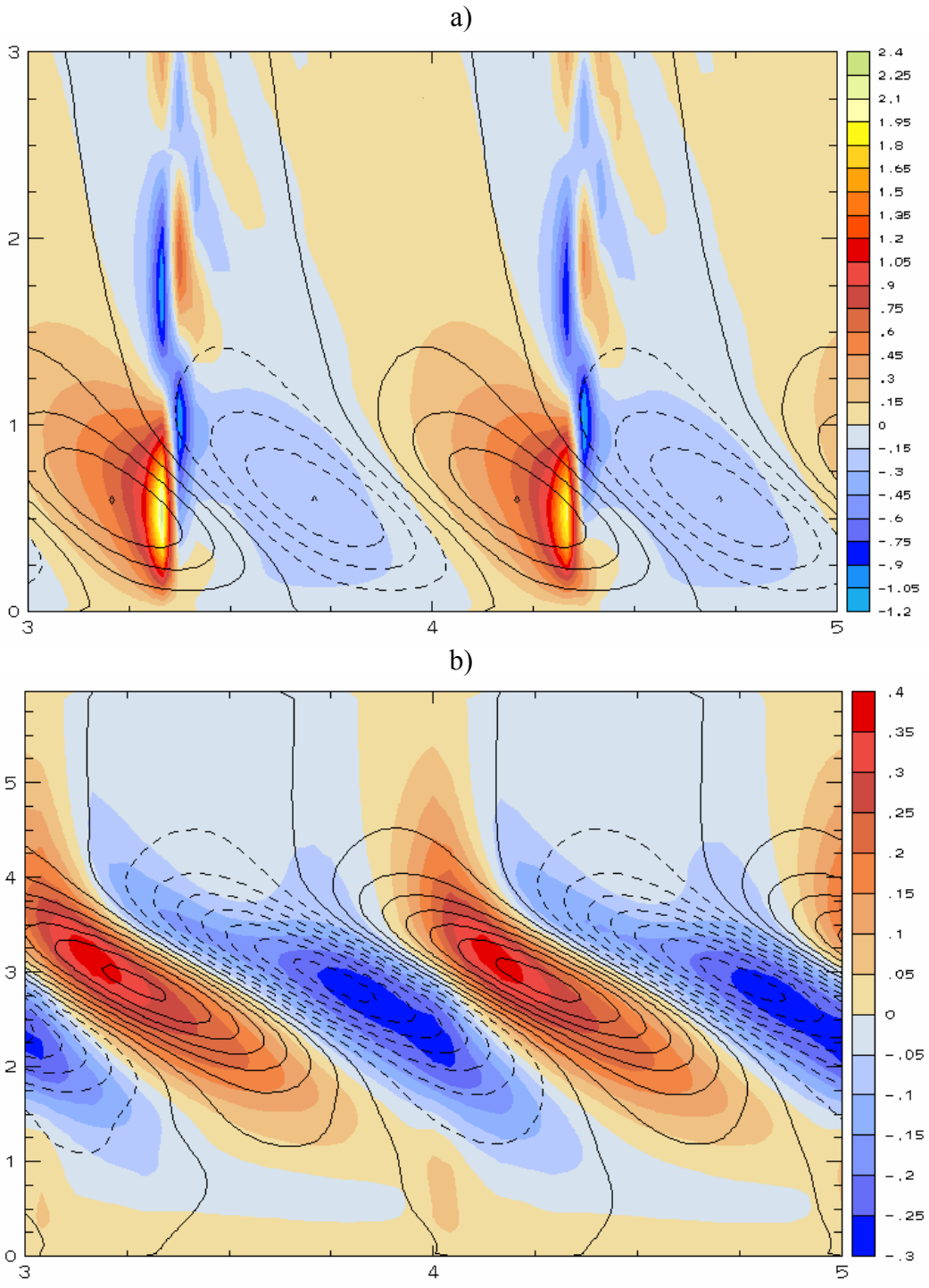

Fig. 14. Nondimensional vertical velocities from days 3 to 5 of $\varepsilon = 0.50$ (color) and $\varepsilon = 0.001$ (line) at a) 75 km inland, and b) 400 km inland. 0º latitude. In a) and b), line contour interval is same as color fill for that figure. Axes are height (ordinate, in km) and time (abscissa, in days).

$$(32) \qquad C = \iint \left(\frac{\partial u}{\partial z} - \frac{\partial w}{\partial x} \right) dA$$

For our circulation calculations, a region bounded by the lower boundary and the inside of the lateral and upper sponge layers was selected. In agreement with Rotunno (1983), the circulation at 0º is found to lag the heating by -π. The magnitude of the circulation increases linearly with heating amplitude, even as nonlinear features local to the coast become present. In addition, the -π phase lag remains unchanged as heating amplitude is increased, solidifying the notion that linear theory does quite well in describing the large-scale atmospheric response for the interior heating case at 0º.

Plotting the nondimensionalized vertical velocities at 2 km altitude across the domain reinforces the general description provided by Figure 14. For the linear case (Figure 15a), the diurnal gravity wave is the sole contributor to the circulation and is located approximately 175-450 km from the coast (at this altitude). In this display, one can see that the aspect ratio of the diurnal wave matches the prediction of linear theory. At 2 km altitude, the peak of the wave is ~ 275 km inland, thus

$$\delta = \frac{H}{L} = \frac{2km}{275km} = \frac{7.272 \times 10^{-5} \sec^{-1}}{0.01 \sec^{-1}} \approx \frac{\omega}{N}$$

In the nonlinear simulation (Figure 15b), the diurnal gravity wave is still evident, but with sharper, much shorter gravity waves propagating upward from fronts in the near coast environment. The most pronounced gravity waves occur above the sea breeze fronts over land, with the waves above offshore land breeze fronts being much weaker. The largest differences between the linear and nonlinear solutions occur in the near-coast environment, and are associated with short-wavelength disturbances generated by frontal

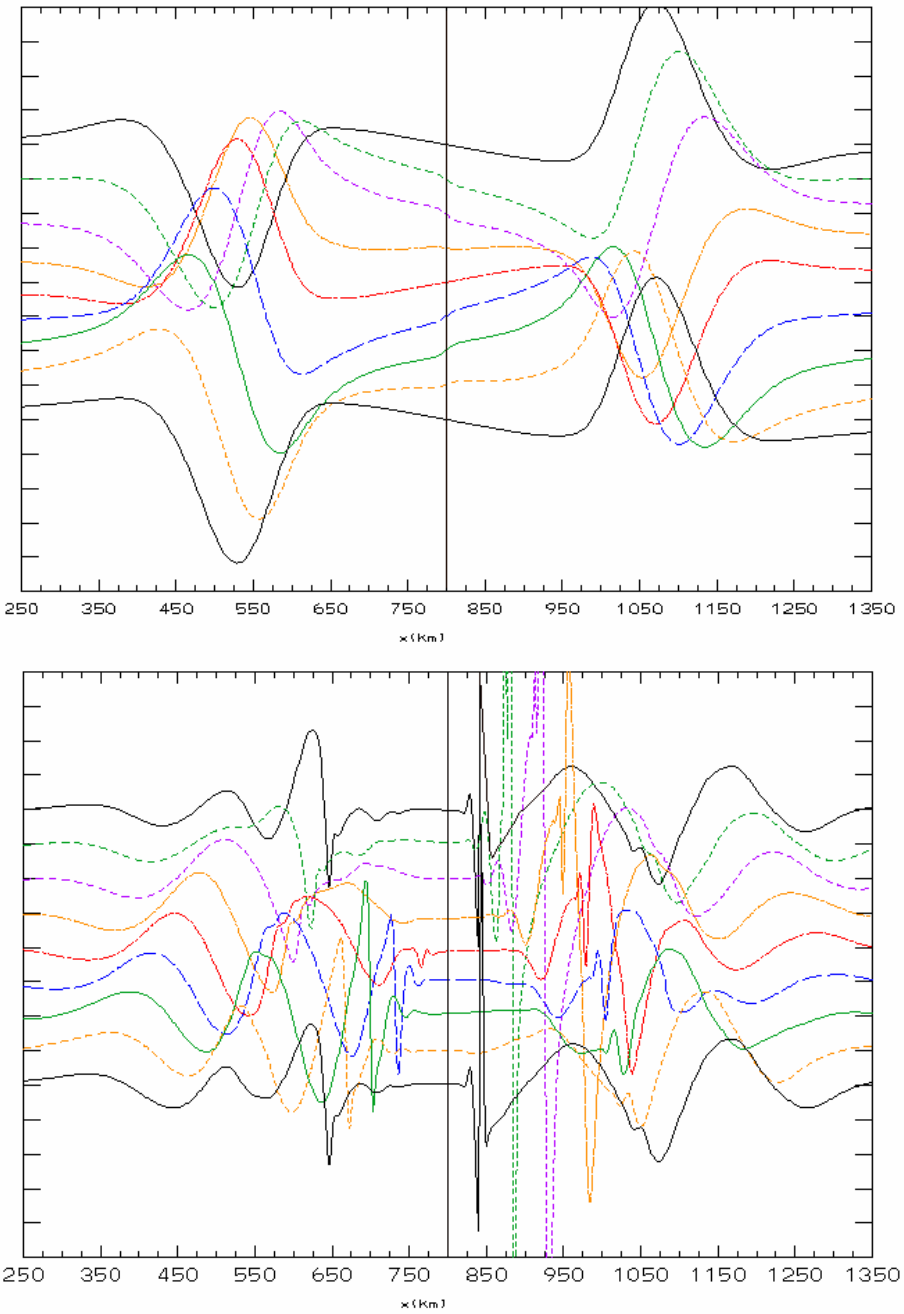

Fig. 15. Horizontal distribution of nondimensional vertical velocity at 2 km altitude for $\varepsilon = 0.001$ (top figure) and $\varepsilon = 0.50$ (bottom figure). Top curve in each figure (solid black) is at the end of the heating (day 3.25), with each subsequent curve 3 h later than the previous, and shifted down by 0.1 for display. Bottom curve (solid black) completes the cycle at day 4.25. Vertical line indicates coast. Vertical tick interval is 0.1.

collapse.

ii) Dependence on Latitude

To investigate the effects of latitude on the circulation, simulations analogous to those used in the previous section were computed at 45˚ (i.e. $R_0 = \omega/f = 1/\sqrt{2}$). After Rotunno (1983), a response much different in both structure and phase is anticipated at 45º. Here, the maximum vertical velocity over land occurs at the 0.00 cycle time (Figure 16c), corresponding to the time of maximum heating. At 0º, the maximum vertical velocity over land occurs at the 0.25 cycle time, out of phase with the heating by $-\pi/2$. As predicted by linear theory, the circulation is in phase with the heating (and thus $-\pi$ out of phase with the equatorial case) at 45º. And as in the equatorial case, the magnitude of the circulation increases linearly with heating amplitude. The progression of the simulation to nonlinearity with increased ε is illustrated qualitatively in Figure 17. It is immediately seen that the progression to nonlinearity is much less dramatic at 45º. Even in the high-amplitude simulations, higher harmonic gravity waves appear to be the dominant nonlinear feature. Figure 18 shows a quantitative progression of the simulations to nonlinearity. One can see that linear theory actually does quite well in predicting the magnitude of the response even at high amplitude. In the most nonlinear simulation, *db/dx* only slightly increases, showing signs of weak frontal collapse. Interestingly, the onshore-offshore asymmetry at 45º is weaker and reversed with respect to the equatorial case.

Also interesting is that the coastal cold anomaly found in the equatorial case is

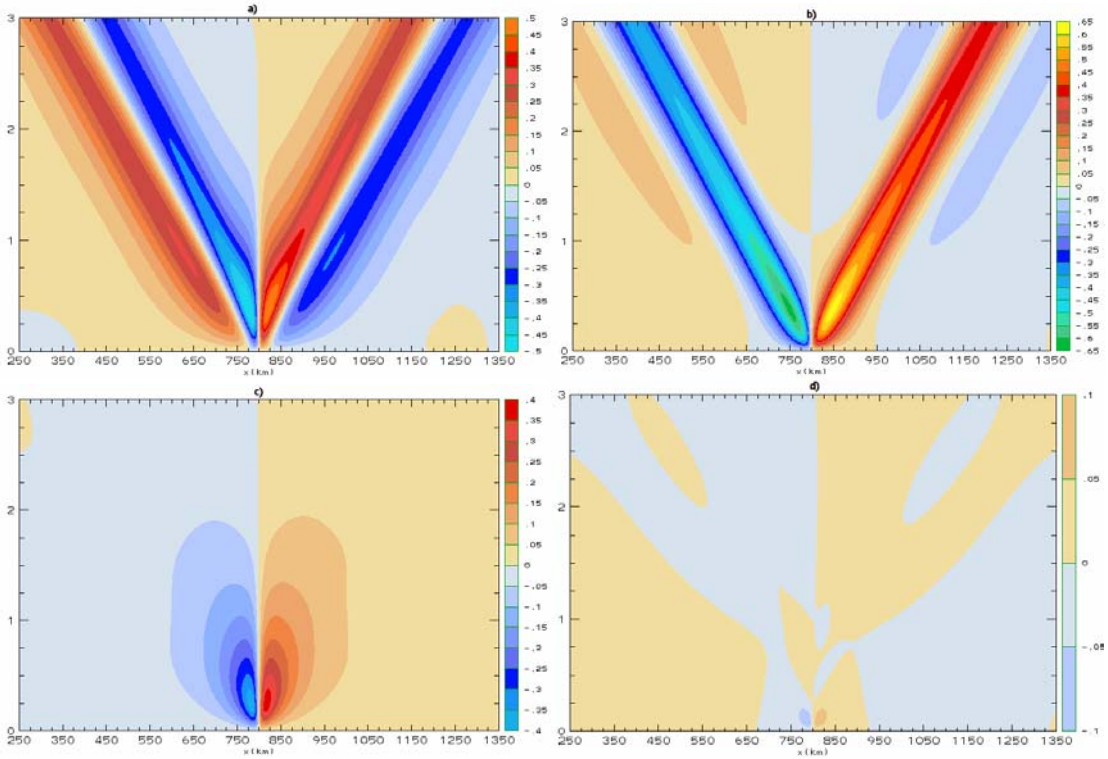

Fig. 16. Nondimensional vertical velocities for interior heating ε = 0.001 at a) 0º day 5.00, b) 0º day 4.25, c) 45º day 5.00, and d) 45º day 4.25. Horizontal and vertical axes are x and z (respectively) is kilometers. Contour interval is constant throughout.

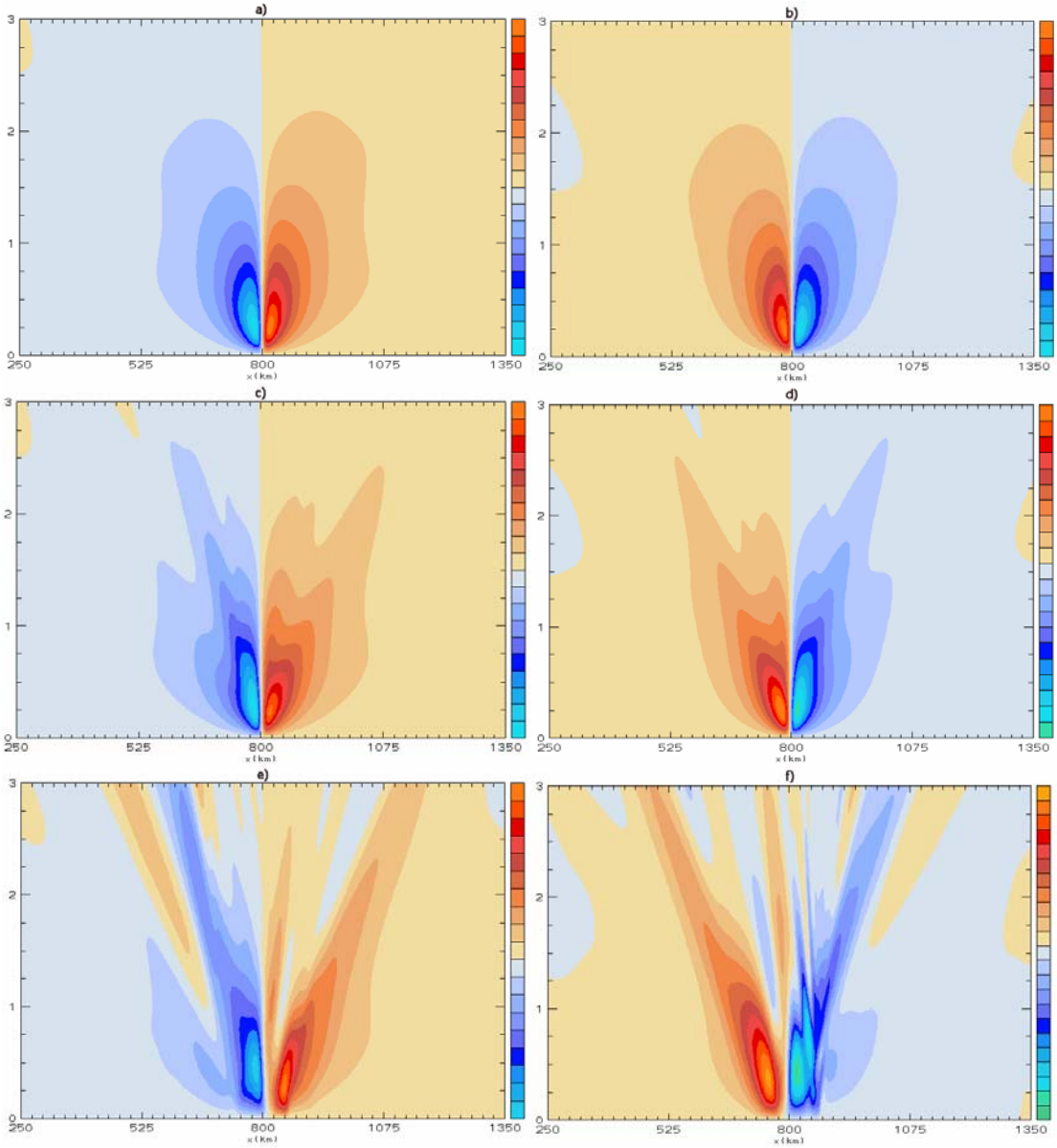

Fig. 17. Nondimensional vertical velocities for the 45º interior heating simulation a) ε = 0.001 at 4.00 days, b) ε = 0.001 at 4.50 days, c) ε = 0.10 at 4.00 days, d) ε = 0.10 at 4.50 days, e) ε = 0.50 at 4.00 days, f) ε = 0.50 at 4.50 days. Horizontal and vertical axes are x and z (respectively) in kilometers. Contour interval is constant throughout.

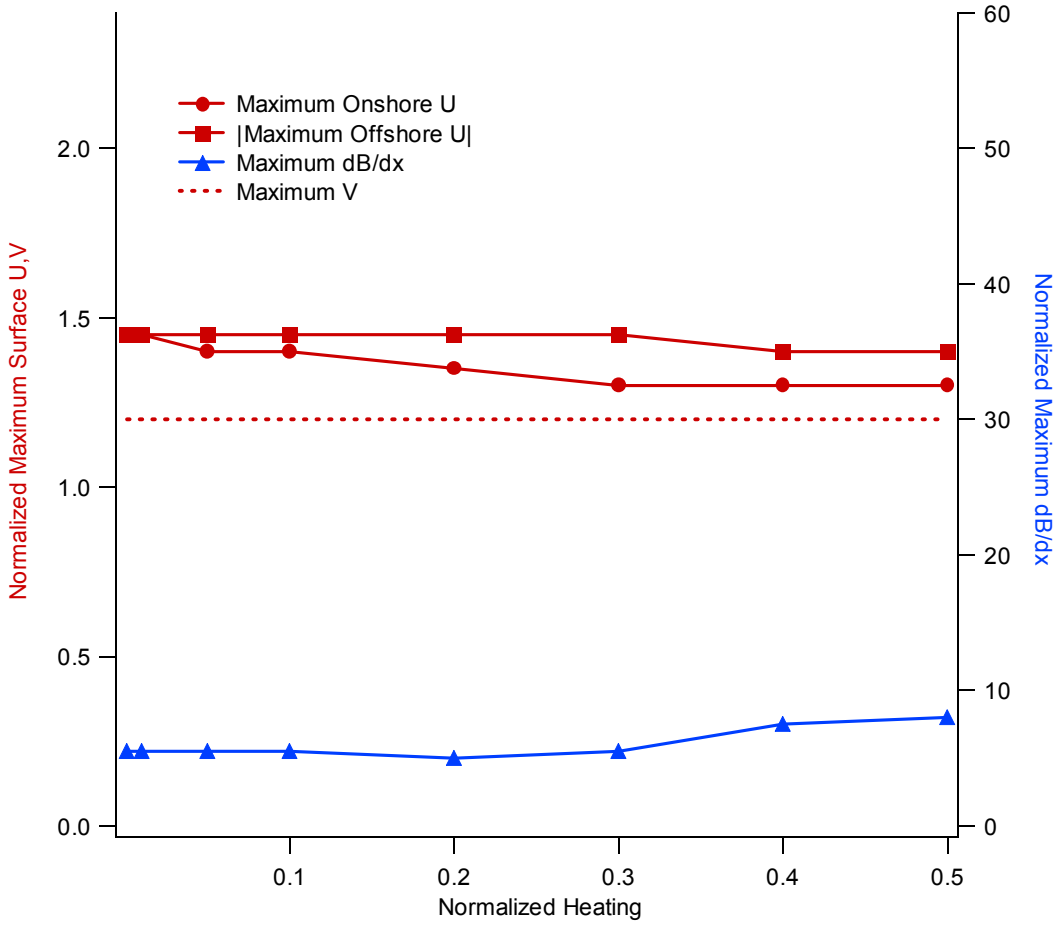

Fig. 18. Nondimensional maximum surface onshore u, offshore u, maximum v, and db/dx vs. nondimensional heating (ε) for interior heating at 45º latitude.

again present in the high-amplitude 45º simulations (Figure 19). However, due to the phase of the maximum horizontal wind and presence of the Coriolis force, we expect the effects of the cold anomaly to be different at this latitude. So to find the sources of nonlinearity on the simulation at 45º, we again employ the method of successive corrections.

Recall that in the equatorial case, the variables in the nondimensionalized equations of motion were expanded in a Taylor series consisting of a linear component with successive corrections. This process yields six linear advection terms that could potentially drive nonlinear responses:

$$-\hat{u}^{(0)}\frac{\partial \hat{u}^{(0)}}{\partial \hat{x}} \qquad -\hat{w}^{(0)}\frac{\partial \hat{u}^{(0)}}{\partial \hat{z}} \qquad -\hat{u}^{(0)}\frac{\partial \hat{v}^{(0)}}{\partial \hat{x}}$$

$$-\hat{w}^{(0)}\frac{\partial \hat{v}^{(0)}}{\partial \hat{z}} \qquad -\hat{u}^{(0)}\frac{\partial \hat{\phi}^{(0)}}{\partial \hat{x}} \qquad -\hat{w}^{(0)}\frac{\partial \hat{\phi}^{(0)}}{\partial \hat{z}}$$

Again, since most of the forcing is near the surface, we'll neglect the vertical advection terms. However, at 45º v is not necessarily zero due to the presence of the Coriolis force. Thus, we are left with three advections:

$$-\hat{u}^{(0)}\frac{\partial \hat{u}^{(0)}}{\partial \hat{x}} \qquad -\hat{u}^{(0)}\frac{\partial \hat{\phi}^{(0)}}{\partial \hat{x}} \qquad -\hat{u}^{(0)}\frac{\partial \hat{v}^{(0)}}{\partial \hat{x}}$$

As before, the first correction for non-linearity itself is approximated as the subtraction of $\hat{\phi}$ in the ε =0.001 solution from the ε =0.01 solution divided by (0.01-0.001). Figure 20 shows this first nonlinearity correction for $\hat{\phi}$ at 45º averaged over one cycle. Again, the cold anomaly is the dominant feature throughout the cycle, causing a negative temperature perturbation on average in the near-coast regime. Note also that the cold

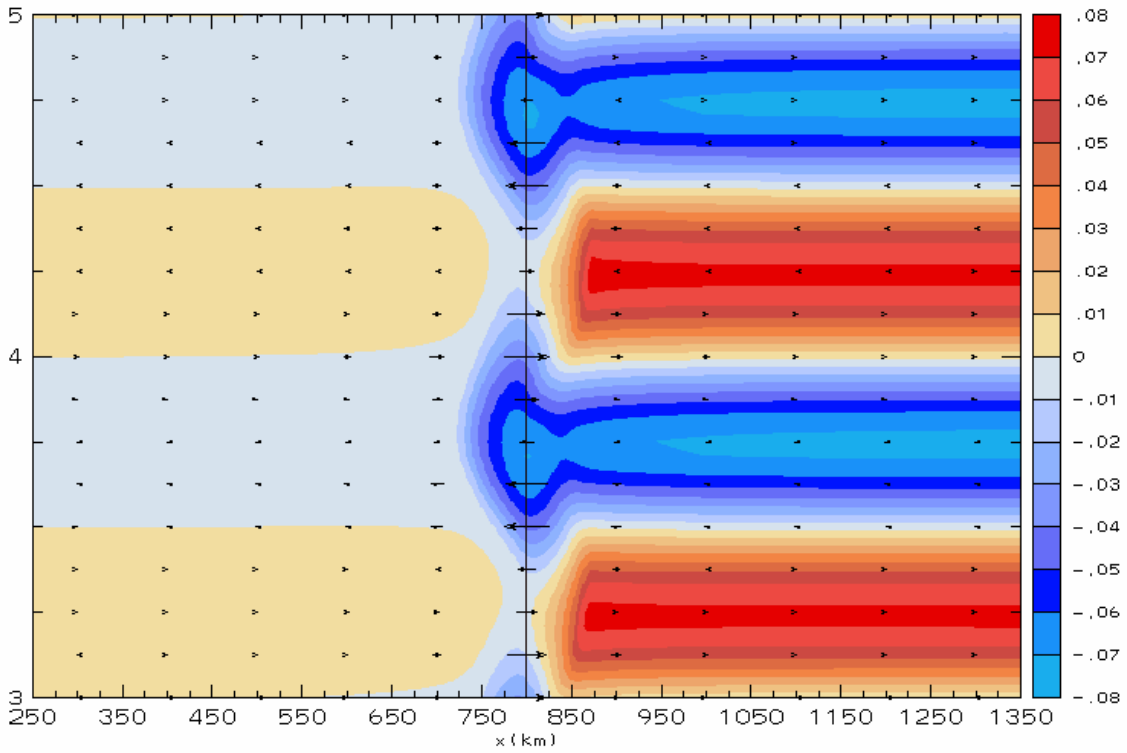

Fig. 19. Hovmoller diagram (days 3 to 5) of perturbation buoyancy (ϕ, color) and shore-perpendicular component to the surface wind (arrow) for interior heating ε = 0.50, 45º latitude. Vertical line indicates coast.

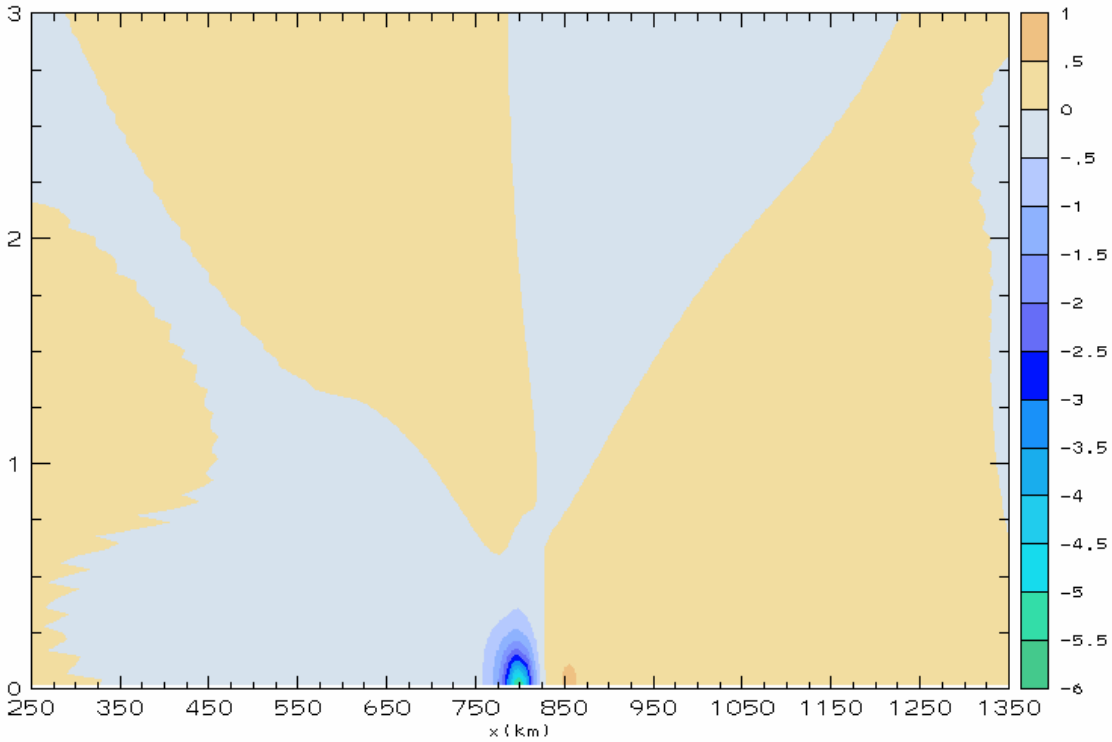

Fig. 20. First correction of nondimensional perturbation buoyancy averaged over days 4-5, 45º latitude. Vertical axis is height in km.

anomaly at 45º does not spread across the domain surface towards the sponge layer as it did in the equatorial case. From this result, and with the knowledge that the Coriolis force is significant at 45º latitude, we hypothesize that the corrections in horizontal velocity will not be permitted to expand outward away from the coastline, as found at 0º.

The first correction in nondimensionalized shore-perpendicular (u) wind is shown in Figure 21. At the 4.00 cycle time (Figure 21a), the correction field exhibits a semi-diurnal gravity wave emanating from the near-coast vicinity. As a function of time (Figure 21b), the net flow at the surface is divergent. As hypothesized, the net surface divergence does not extend horizontally beyond the coastal regime. Also, the flow response at 250 m is only very weakly convergent on average. At 1 km altitude, the semi-diurnal gravity wave is the main component of the flow response. Due to the significant Coriolis force at 45º, this mean surface divergence near the coast is reflected in v as a net along-shore circulation.

This atmospheric response of downward motion and divergence at the coast is consistent with the presence of a mesoscale high-pressure center on average. Indeed such a mesoscale high would be caused by the presence of a cycle-mean cold anomaly at that location, with cold air driving subsidence and thus surface divergence. The Coriolis force would then act to partly balance the pressure gradient force by creating a mean along-shore velocity component. Because of this, and because the cold anomaly so adequately described the first correction atmospheric response at 0º, we hypothesize that the $-u(db/dx)$ forcing term is again responsible for the observed semi-diurnal gravity wave and mean circulation in the first correction fields.

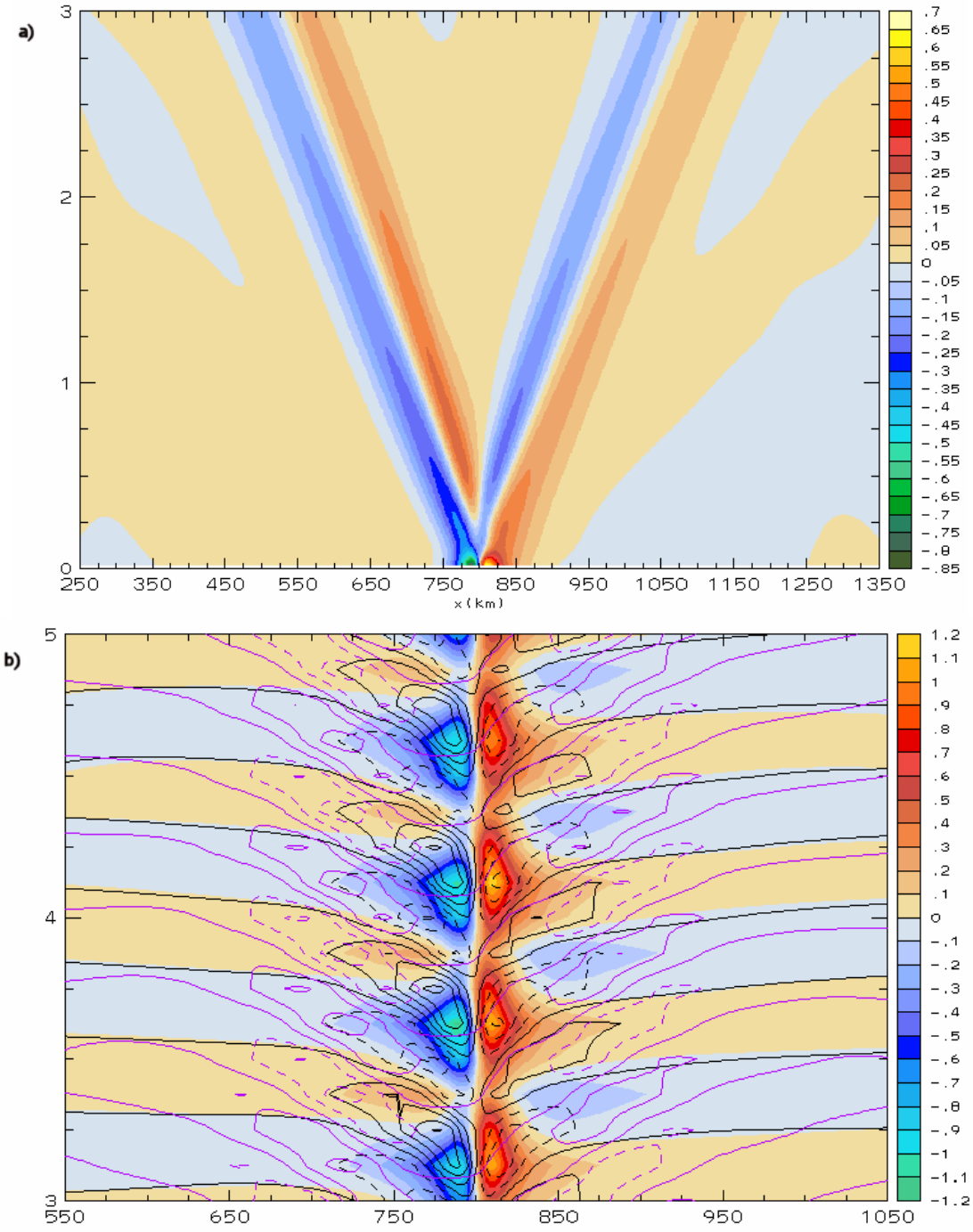

Fig. 21. First correction of nondimensional *u* velocities a) at day 4.00, and b) from day 3 to day 5 at the surface (color fill), at 250m (black line), and at 1km (color line) altitude at 45º latitude. Solid line is positive, dash is negative. Line contour interval is same as color fill.

The advection field $-u(db/dx)$ for the linear 45º simulation is shown in Figure 22. The cold advection pattern here looks very similar in magnitude to that found at 0º, however the phase of the advection is shifted such that the maximum cold advection occurs here 0.125 cycles (3 hours) earlier. To isolate the atmospheric response to this linear advection term, and thus to test the above hypothesis, a heating shape analogous to that used in the equatorial case

$$H(x,z,t) = A\left(\frac{x_0}{x_0^2 + x^2}\right)e^{\left(-z/z_0\right)}\cos(\omega t + \lambda) + B \tag{33}$$

is applied as a small-amplitude interior heat source oscillating at twice the diurnal frequency. The phase λ and bias B of the oscillation is set to mimic the oscillation of $-u(db/dx)$ at 45º. Again, x_0 and z_0 are 10000 m and 500 m, respectively.

Figure 23 shows the atmospheric response to this forcing at 4.00 days into the simulation. Though the applied forcing excites a semi-diurnal gravity wave, it is very weak and of the opposite phase from that found in the net correction. However, averaged over one cycle, nonlinearity due to the linear advection of the linear temperature gradient does account for the net surface divergence and weak convergence aloft near the coast. We must then conclude that though the $-u(db/dx)$ term is responsible for driving the cycle-mean response, the semi-diurnal gravity wave response at 45º is a result of the remaining linear advection terms

$$-\hat{u}^{(0)}\frac{\partial \hat{u}^{(0)}}{\partial \hat{x}} \qquad -\hat{u}^{(0)}\frac{\partial \hat{v}^{(0)}}{\partial \hat{x}}.$$

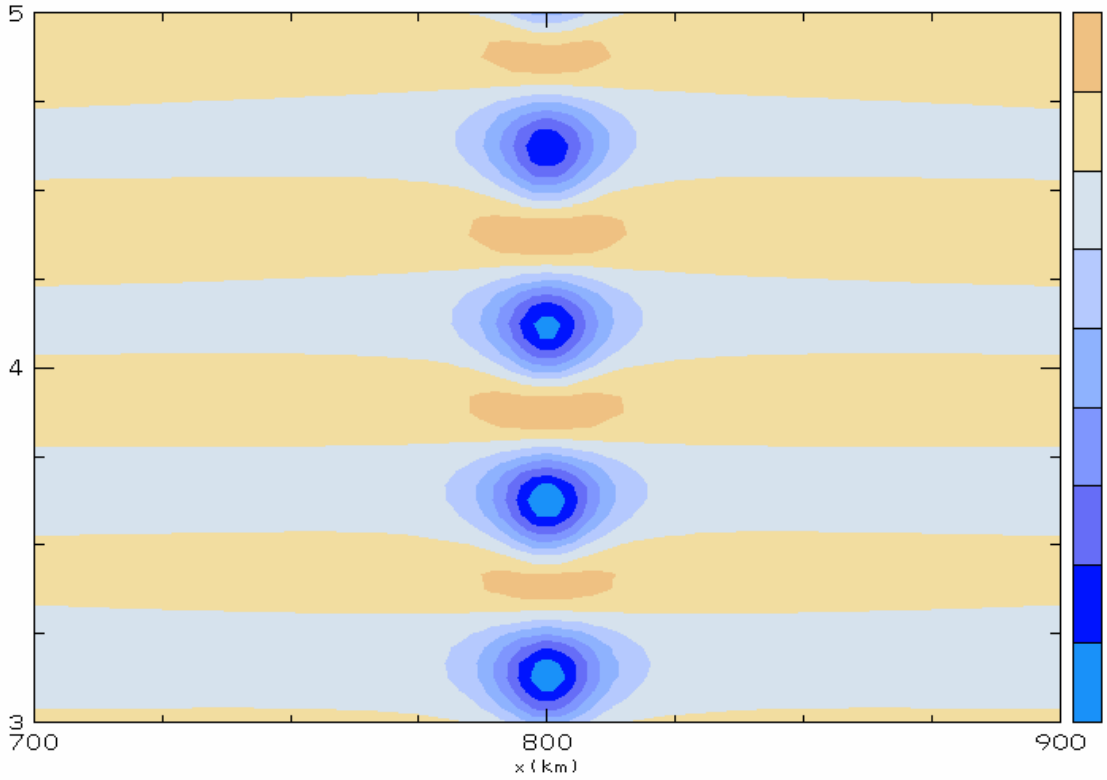

Fig. 22. Hovmoller diagram (days 3 to 5) of $-u(db/dx)$ for interior heating $\varepsilon = 0.001$, 45º latitude. Contour interval is 3 x 10^{-12}.

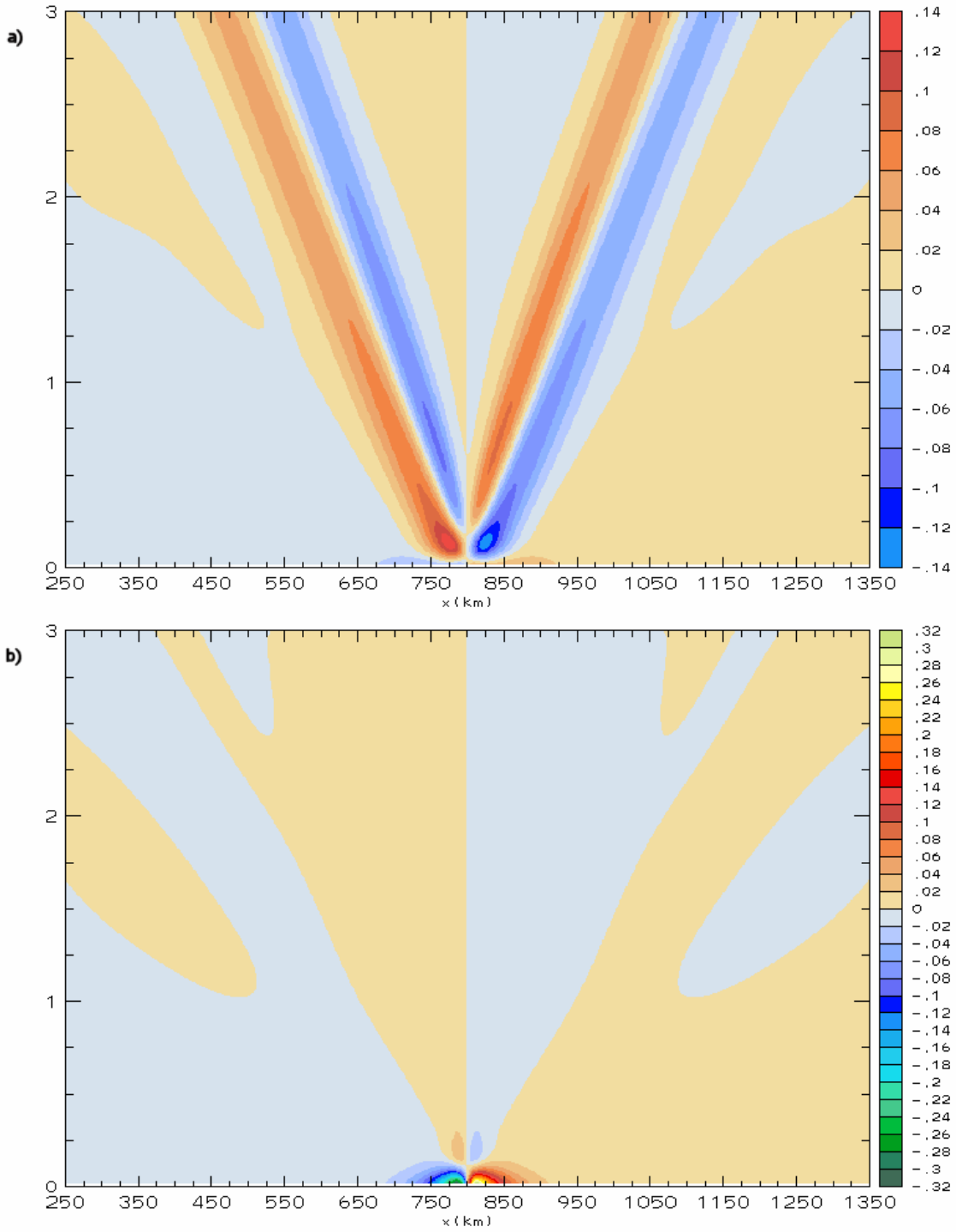

Fig. 23. Nondimensionalized u velocity as a response to semi-diurnal cold advection forcing a) at cycle time 4.00, and b) averaged over days 4-5. Vertical axis is height in km. 45º latitude.

As mentioned, frontal collapse does not seem to be occurring as strongly in the 45º simulations as at the equator. We again compute frontogenetic advection, contraction, and tilting terms

(34) $\varepsilon^{(1)}$ system:

$$\frac{\partial}{\partial t}\left|\frac{\partial b^{(1)}}{\partial x}\right| + u^{(0)}\frac{\partial}{\partial x}\left|\frac{\partial b^{(0)}}{\partial x}\right| + w^{(0)}\frac{\partial}{\partial z}\left|\frac{\partial b^{(0)}}{\partial x}\right| = -\frac{\partial u^{(0)}}{\partial x}\left|\frac{\partial b^{(0)}}{\partial x}\right| - \left(\frac{\partial w^{(0)}}{\partial x}\frac{\partial b^{(0)}}{\partial z} + N^2\frac{\partial w^{(0)}}{\partial x}\right)\frac{\frac{\partial b^{(0)}}{\partial x}}{\left|\frac{\partial b^{(0)}}{\partial x}\right|}$$

from the small amplitude interior heating 45º simulation. As before, the terms that involve *w* are neglected, leaving only the contraction term

$$-\frac{\partial u^{(0)}}{\partial x}\left|\frac{\partial b^{(0)}}{\partial x}\right|$$

to describe the Lagrangian frontogenesis tendency. For comparison, the advective term

$$u^{(0)}\frac{\partial}{\partial x}\left|\frac{\partial b^{(0)}}{\partial x}\right|$$

is also plotted so that some comment can be made regarding the net local tendency of the buoyancy gradient at any time.

Figure 24 shows these terms and their sum throughout the cycle. The time evolution of the Lagrangian frontogenesis term (contraction) at 45º is similar to its equatorial evolution in that the maximum value over land is reached 3 hours after peak heating. However, one glaring difference in the contraction term is that the magnitude is about 50% smaller at 45º.

This weaker isentropic collapse at 45º is due to the presence of the Coriolis force. Coriolis dictates that the maximum linear horizontal wind at the coast occur at the time of peak heating, rather than the end of the heating as at the equator. At this time, the

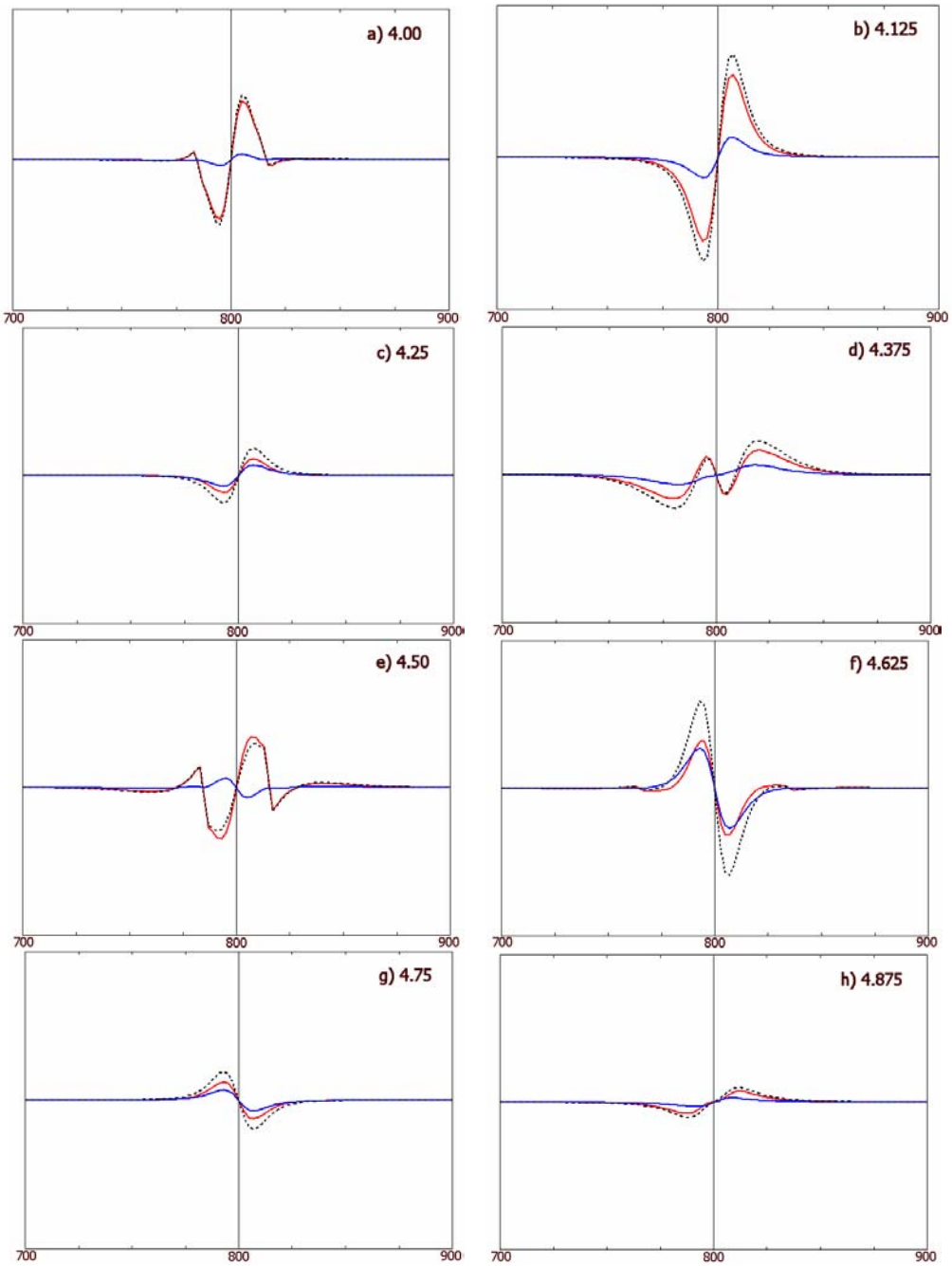

Fig. 24. Surface frontogenetic forcing in the interior heating $\varepsilon = 0.001$ simulation due to advection (red), and contraction (blue), at day a) 4.00, b) 4.125, c) 4.25, d) 4.375, e) 4.50, f) 4.625, g) 4.75, and h) 4.875. The sum of the forcing terms is black dash. 45º latitude. Vertical line indicates coast. Vertical axis scale is 1.5×10^{-15}.

temperature gradient created by the heating has not reached maximum intensity. By the time the temperature gradient reaches its maximum at the end of the heating cycle, the Coriolis force has introduced an alongshore component to the wind, weakening onshore flow and thus weakening horizontal convergence near the coast. Finally, because maximum *u* at the coast is out of phase with the equatorial *u*, the contraction and advection terms of frontogenesis are always in phase.

Frontal propagation is also inhibited at 45º latitude. As fronts form and begin to propagate inland, the onshore component of motion is acted upon by the Coriolis force, turning it in the alongshore direction. The Coriolis force then acts on this alongshore wind, forcing it in an offshore direction, and inhibiting the horizontal propagation of any fronts that form. Figure 25 shows silhouettes of sea breeze fronts at 3 hour intervals for $\varepsilon = 0.50$ interior heating simulations at 0º and 45º. Since the fronts do not rapidly propagate away from the coastline at 45º as they do at 0º, there are no non-hydrostatic gravity waves that propagate vertically from the front. In addition, while the equatorial sea breeze front lasts over 9 hours and propagates several hundred kilometers inland, the Coriolis force has inhibited the propagation and sustainment of the front at 45º. In fact, there is only an appreciable signal at the end of the heating cycle (model time 4.25).

Since the gravity waves emanating vertically from fronts at 45º are very weak, linear theory does even better at predicting the nature of the near-coast response (Figure 26a) than it did at the equator. In the far-field (Figure 26b) linear theory predicts the 0-1.5 km response well. Above that, there appears to be the introduction of a faster gravity wave mode. This nonlinear feature has an approximate frequency of 1.2×10^{-4} sec^{-1}.

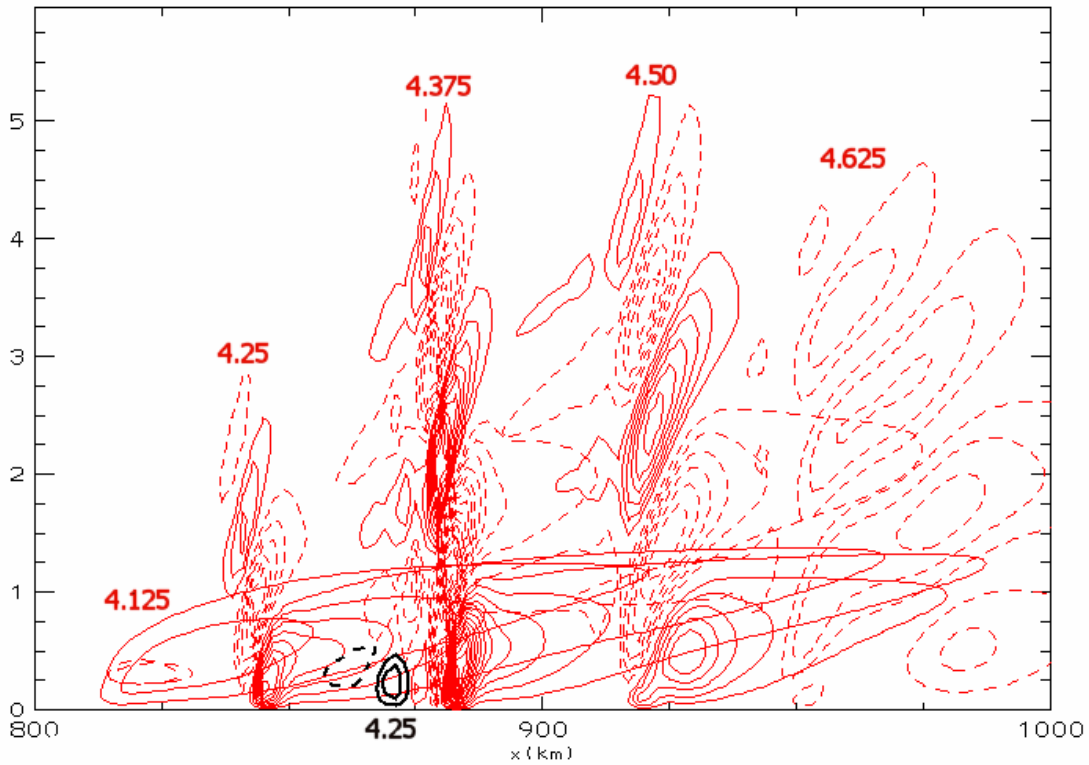

Fig. 25. Temporal snapshots of nondimensionalized vertical velocity at 800-1000 km for ε = 0.50 interior heating simulations at 0º (red) and 45º (black). Contour interval is consistent throughout.

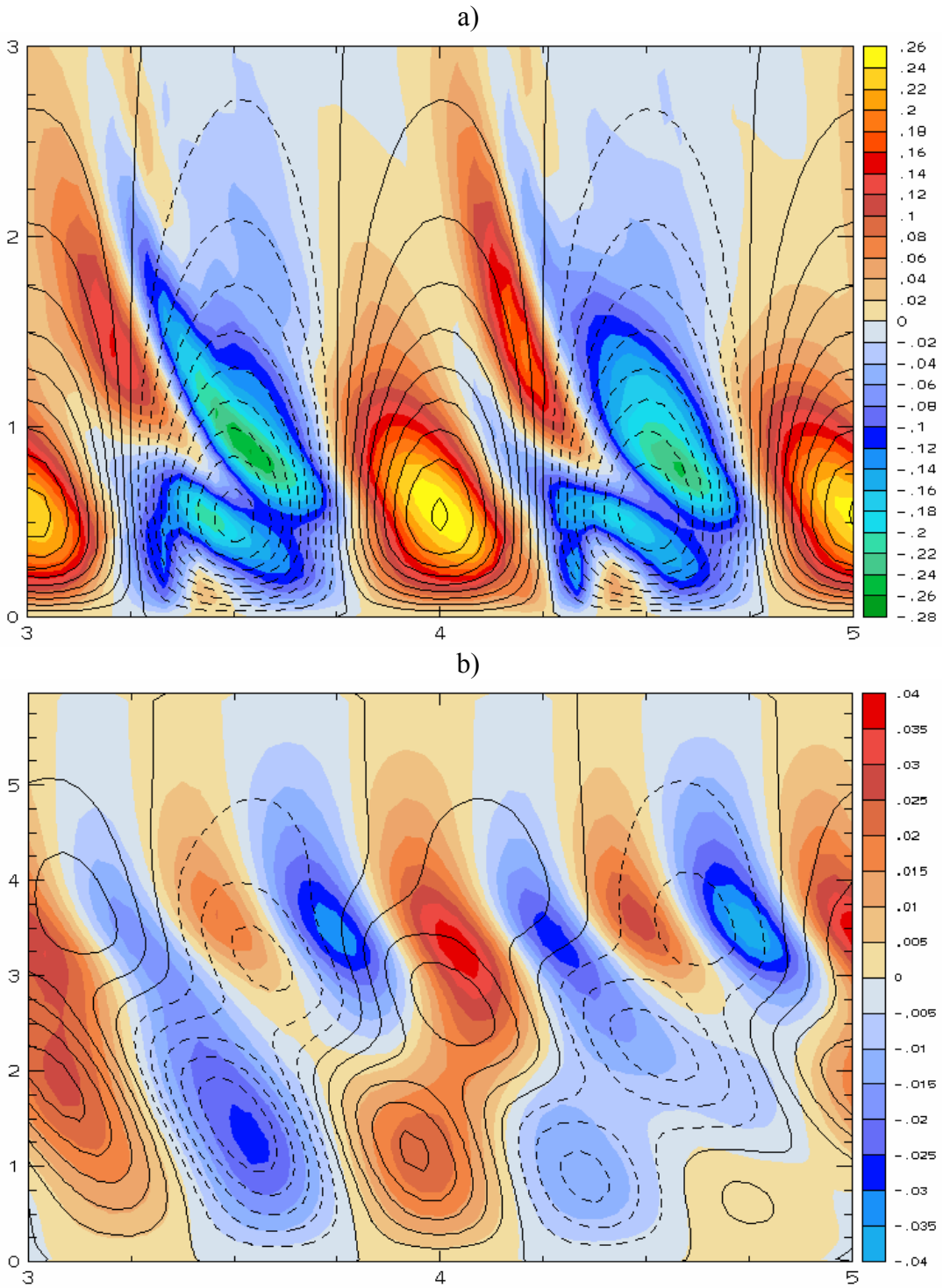

Fig. 26. Nondimensional w velocities from day 3 to day 5 for $\varepsilon = 0.50$ (color) and $\varepsilon = 0.001$ (line) at a) 75 km inland, and b) 400 km inland. 45º latitude. In a) and b), line contour interval is same as color fill for that figure.

iii) Comparison to Observations

It appears that much of the structure in our surface-forced sea-breeze simulation (shown in the preliminary comparison in Chapter III Section iii can be reproduced by increasing the amplitude in the interior heating solution. However, differences remain. The goal of this research is not to correctly simulate the full reality of the sea-breeze circulation, yet it is worthwhile to use real atmospheric data as a guide to steer the next level of complexity for subsequent experiments.

Intuition would lead one to believe that the daytime mixed layer is deeper than the nighttime inversion layer. To compare the thermodynamic evolution in the interior heating simulation with real atmospheric data, we use observed θ (potential temperature) profiles from the TEXAQS (Texas Air Quality Study) 2000 data set. For this data to be as "idealized" as possible, we chose a day in which thermal advection aloft was minimized. The day that met this criterion is August 30, 2000. The site with the best available data is the HOU sounding site, roughly 75 km inland. For direct comparison, all θ soundings from the model were taken from the same distance inland. To compare the temporal evolution of the model data with reality, local daylight times (Central Daylight Time, CDT, in this case) were assigned to model cycle times. For these assignments, see Table 1.

Table 1: Central Daylight Time (CDT) and corresponding model cycle time and heating description.

CDT	Model Cycle Time	Heating
1800	0.25	End of Heating, sunset
0000	0.50	Peak Cooling, midnight
0600	0.75	End of Cooling, sunrise
1200	1.00	Peak Heating, noon

Note that these assignments are approximate, as Houston in August does not see an equal number of daylight and nighttime hours.

Figure 27 shows the sounding from Houston, Texas on August 30, 2000, with Figure 28 focusing on the low level structure for a direct comparison between the lowest 1500 m of the observed sounding and the model sounding for the high-amplitude interior heating case. The background temperature profile in our simulations has a surface temperature of 273 K, much colder than August in Houston, Texas. We are concerned here only with the temporal variation of the temperature profile, and not with absolute quantities. As anticipated, the daytime mixed layer in the observations is much deeper than the nighttime cold layer. In fact, the difference is nearly a factor of two. By contrast, the model sounding shows a cooling layer nearly equal in depth to the daytime warm layer.

The differences between the thermodynamic profiles of the model and observations result from the constraint of the heating and cooling in the interior heating model to a specified shape. In the real atmosphere, the effective heating shape is determined by a complex interaction of convective heat transfer and radiation, with the heating shape having no constraint in time and space. As a next step, we then consider

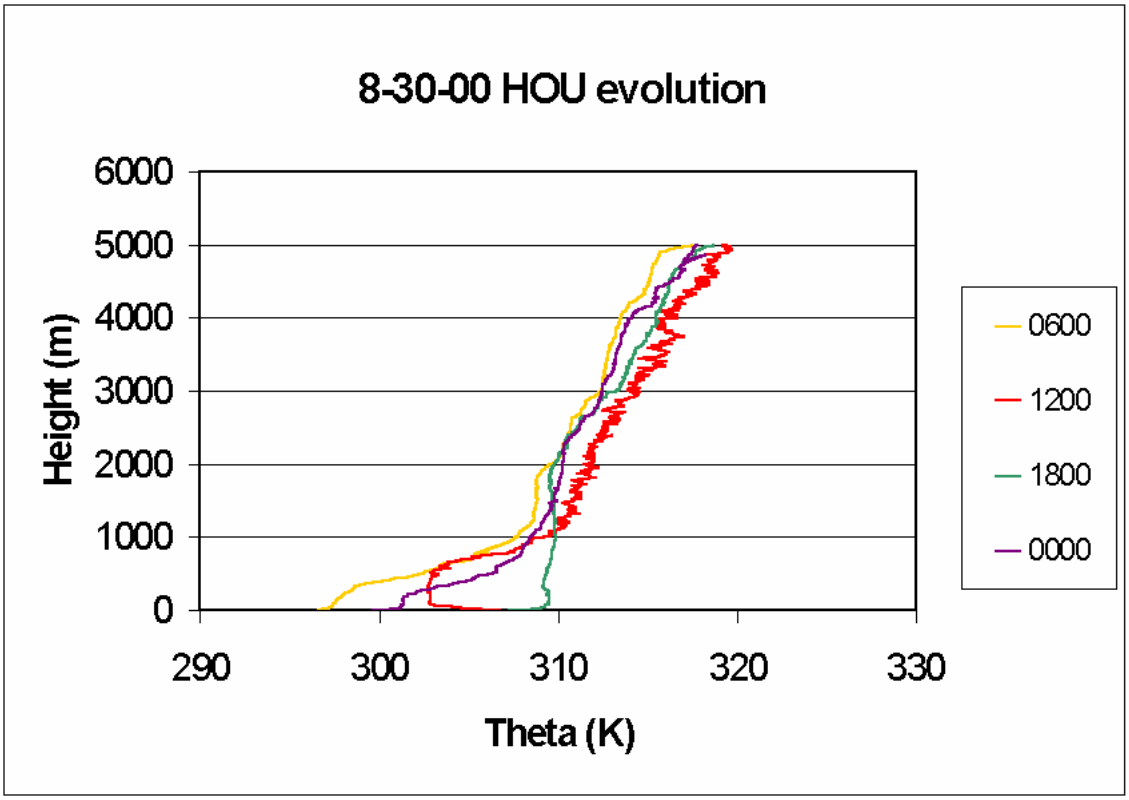

Fig. 27. Evolution of θ profile from Houston, Texas 8-30-00.

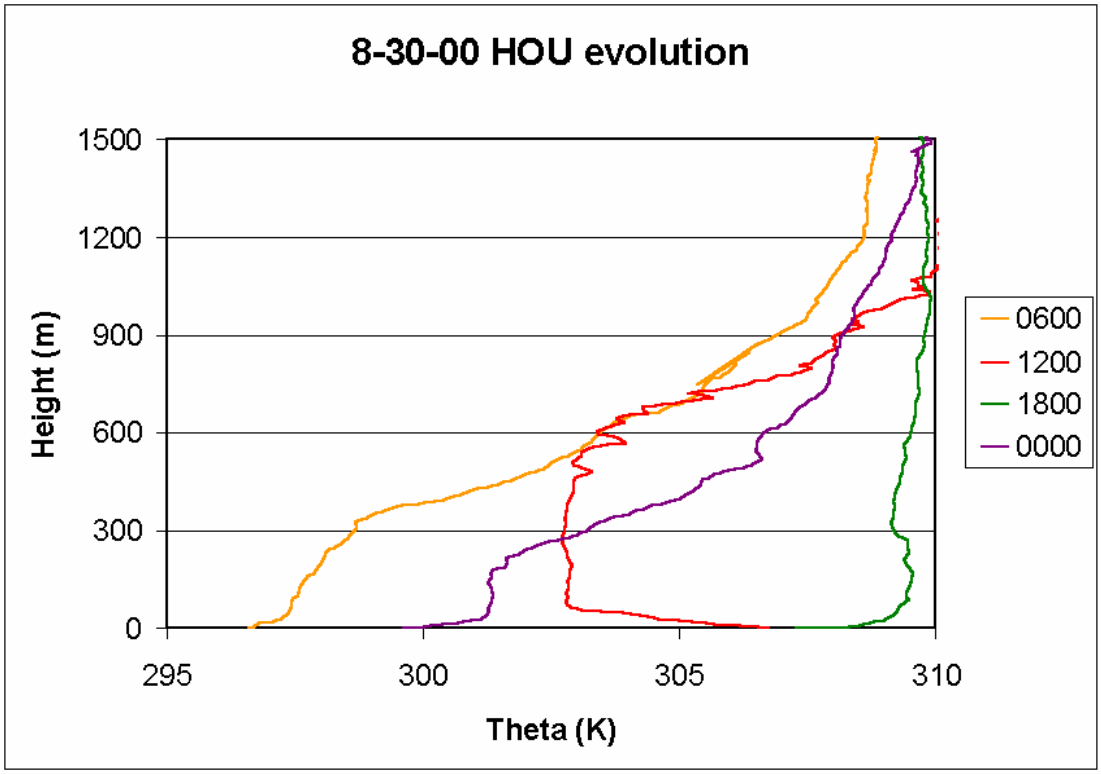

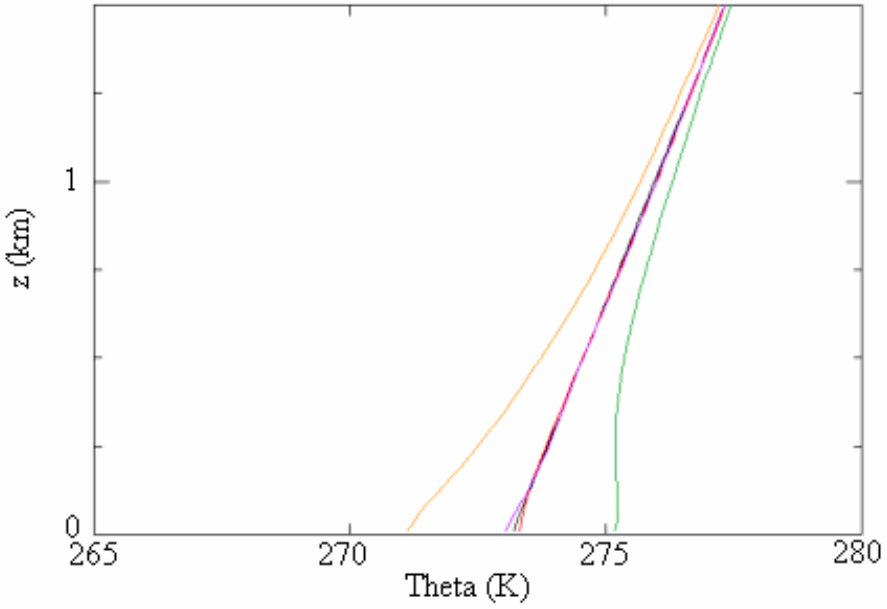

Fig. 28. a) same as Fig. 28 but lowest 1500 m., b) θ profile from 0600 (yellow), 1200 (red), 1800 (green), and 0000 (purple) LST of ε = 0.50 interior heating simulation, 550 km inland. Black line is background profile.

the atmospheric response to a more realistic, but still highly idealized, forcing model. This model will be an oscillating specified heat flux across the lower boundary combined with simple representations of turbulent heat fluxes and radiative damping.

CHAPTER V

SURFACE HEATING

With the interior heating method, the forcing was specified throughout the depth of the domain. In an attempt to experiment with what may be considered a more realistic heating shape, we now consider a model in which an oscillating heat flux is specified at the surface of the model domain. This leaves the vertical distribution of heating to the model's turbulent mixing parameterization. To ensure that the net heat added to the domain will be equal to that applied in the interior heating case, the surface heat flux function is the interior heating function integrated vertically. The surface heat flux is then given by

$$F(\mathrm{x},\mathrm{t}) = z_0 Q_0 \left[\left(\frac{\pi}{2} \right) + \tan^{-1} \left(\frac{x}{x_0} \right) \right] \cos(\omega t) \,. \tag{35}$$

where again Q_0 is linearly ramped from 0 to Q_0 during the first cycle.

Figure 29 shows the evolution of the θ profile in a high-amplitude surface heating simulation. The profile is shown far from the coast to avoid contamination from atmospheric motions. Immediately, it is evident that the surface heating method reproduces the observed shape of the atmospheric temperature profile more accurately than the interior heating case. First, a well-mixed neutrally stratified layer develops in the afternoon hours, followed by a much shallower cold layer at night. Because the net cooling is contained in a shallower layer than the heating, the departure of the surface temperature from the background value is greater at night than during the day.

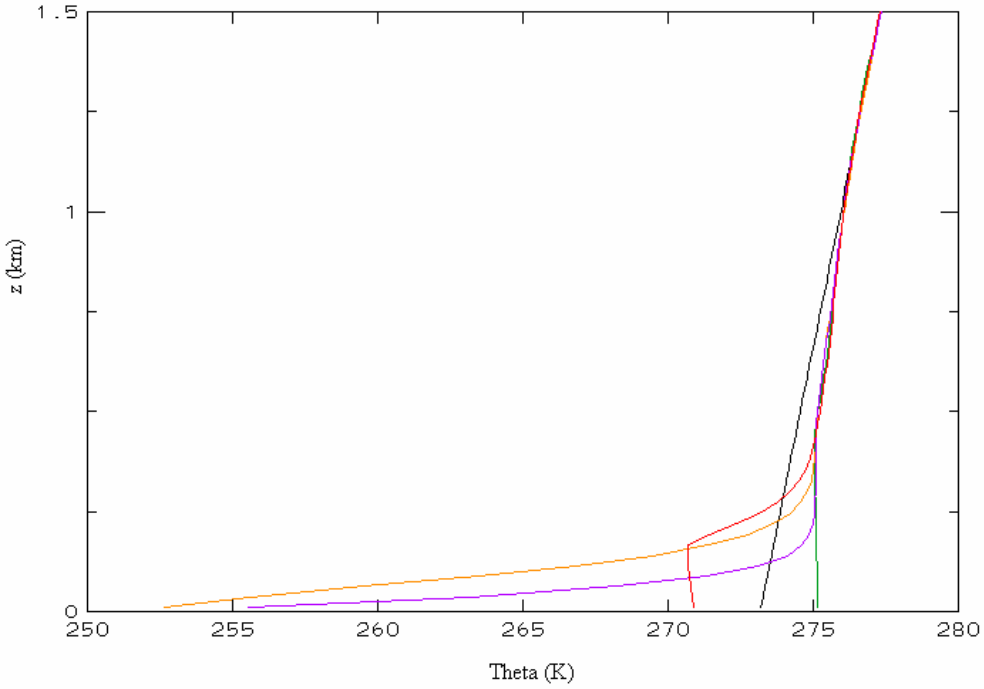

Fig. 29. θ profile from 0600 (yellow), 1200 (red), 1800 (green), and 0000 (purple) of ε = 0.50 surface heating simulation 550 km inland. Black line is background profile.

However, note that the depth of the simulated mixed layer and inversion layer is much shallower than that seen in the observations.

The shallowness of the cool layer in the model relative to observations may be due in some degree to anomalous nocturnal mixing by a low-level jet in the vicinity of the Houston sounding on the night in question. Because of the low level jet maximum, the boundary layer remained somewhat turbulent, resulting in a nocturnal cold layer somewhat deeper than what may be found on a night without a low level jet. The relative shallowness of both the nighttime cold layer and the daytime mixed layer can be partially attributed to the equivalent surface heat flux in these simulations being several times smaller than what may be found in a realistic atmosphere. The shallowness of the daytime neutral layer in the model can also be partially attributed to the lack of any cooling processes in the model aloft.

The first heating cycle after model start-up injects a positive temperature anomaly into the top of the boundary layer near 500-750 m. Since model cooling does not spread as far upward as the heating, the warm layer remains and inhibits subsequent heating cycles from reaching or surpassing that original heating depth. As a result, at high heating amplitudes a further increase in forcing primarily shifts the modeled profile to warmer temperatures and does little to increase the depth of the neutral layer (Figure 30). In the real atmosphere, this warm layer would be acted upon by additional processes such as radiative cooling that are not included in the model. Because the net surface heat flux is zero, the extreme low-level cooling at night is impossible for the daytime heating to overcome, making the creation of a deep mixed-layer during the day

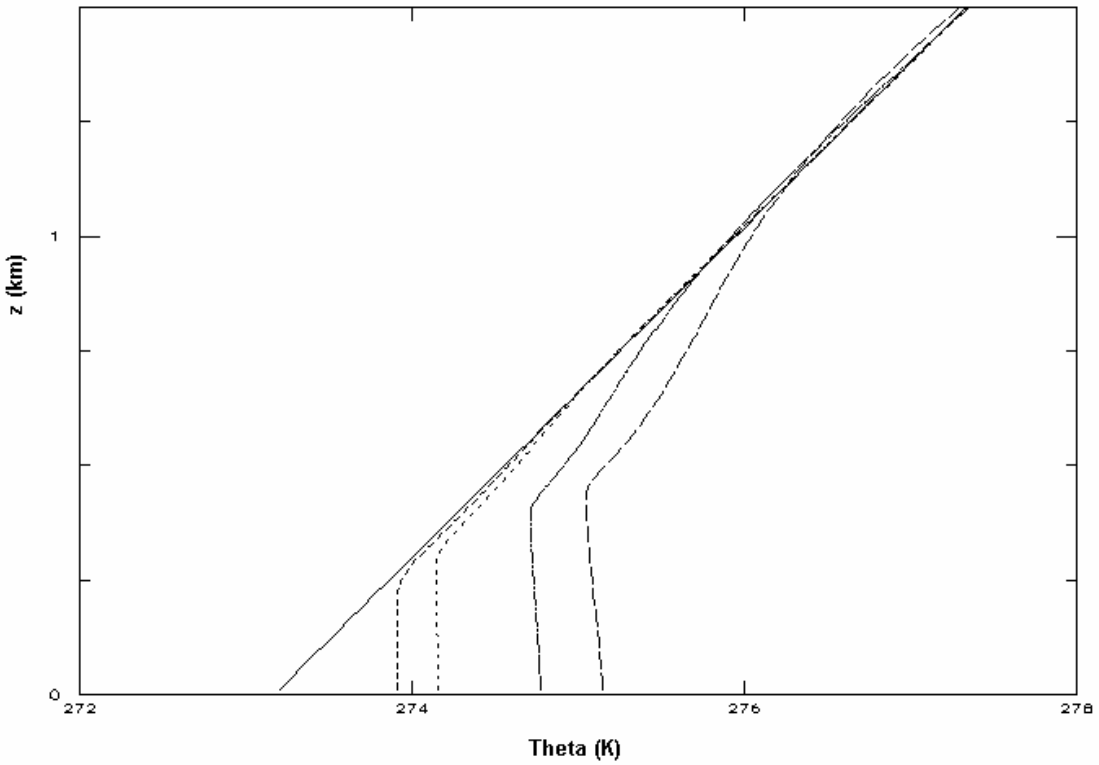

Fig. 30. θ profiles at 4.25 days from 550 km inland, ε = 0.05 (dash), ε = 0.10 (dot), ε = 0.30 (dash-dot), and ε = 0.50 (long-dash). Solid line is background profile.

difficult. A deep neutral layer is desirable here because in the real atmosphere, mixed planetary boundary layers extend to depths on the order of one kilometer or greater.

To simulate a more realistic boundary-layer depth, a Newtonian damping term is added to the heating function to crudely represent the effects of atmospheric radiation. The Newtonian damping acts to relax the simulated profile to the specified background state. The magnitude of this relaxation term must be chosen carefully as to avoid the damping of any gravity wave signal that may be present. A relaxation coefficient of 1.158×10^{-5} (1 per day) was selected. As seen in Figure 31, this minor change decreases the warm layer aloft and leads to a more accurate representation of the planetary boundary layer. And an increase in the heating amplitude now leads to a more significant increase in the depth of the mixed-layer, with the $\varepsilon = 0.50$ case yielding an 800 m planetary boundary layer depth.

To test the extent to which this relaxation coefficient affects the diurnal gravity wave, it is included in a small amplitude interior heating simulation at 0º latitude. As expected, the gravity wave signal is disturbed to some degree. The strength of the vertical velocities due to the gravity wave response are decreased by 25%, while minor distortion of the overland ray path creates an asymmetry in the solution (Figure 32). This asymmetry is expected, because while the damping is applied throughout the entire domain, it has the greatest impact over land where the heating and cooling amplitude is the largest.

Recall that in the quantitative analysis of the interior heating problem the nonlinearity of a simulation was determined by

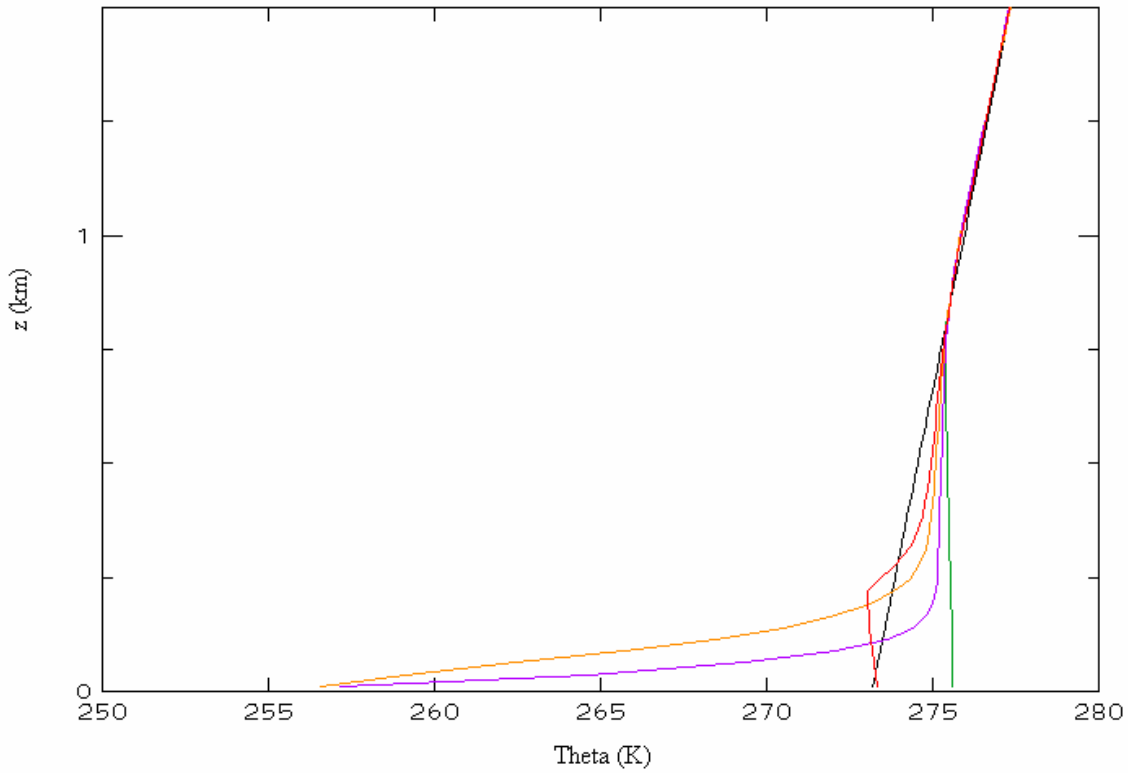

Fig. 31. Same as Fig. 29, except with Newtonian damping.

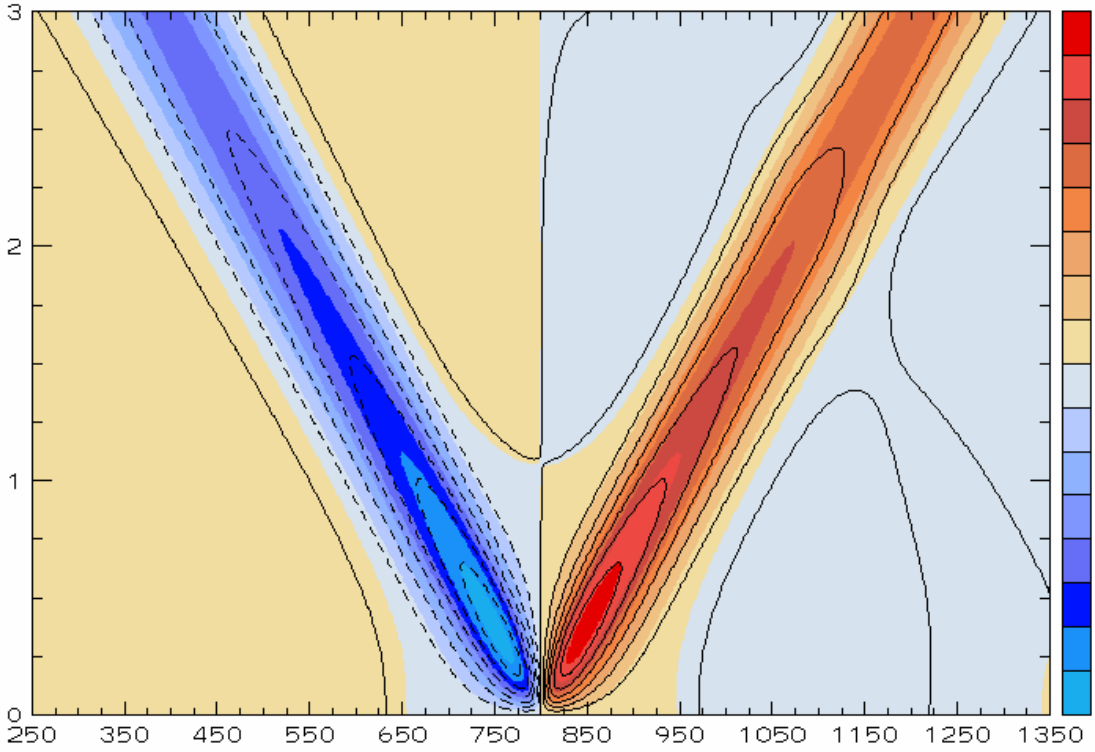

Fig. 32. Nondimensional vertical velocity from day 4.25 of interior heating $\varepsilon = 0.001$ simulation with (line) and without (color fill) Newtonian damping. x and z axes are horizontal and vertical distance in km. Contour interval is consistent for line and color fill.

$$\varepsilon = \frac{Q_0}{N^2 \omega H}.$$

With interior heating, the heating shape was specified such that the average θ profile over one cycle equaled the background temperature profile. In the surface heating problem, the vertical distribution of heat is no longer explicitly set, and there is no such constraint. As a result, the average θ profile over land is not equal to the background stratification. Rather than the constant $N = 0.01$ of the interior heating problem, the average θ profile in the surface heating simulations (shown in Figure 33) has a weakly stratified region aloft due to the remnants of the warm anomaly discussed previously, and a strongly stratified region near the surface due to the shallowness, and thus intensity, of the nocturnal cooling.

To analogously compare the surface heating method with the interior heating method, the resultant effective heating from a high-amplitude surface heating simulation would be specified as an interior heat source. The amplitude of that shape could then be modulated to produce simulations at various levels of nonlinearity (i.e. with various amounts of net heat added to the domain), and could directly be compared to the interior heating simulations. However, since the effective heating is relative to the specified background profile and not the actual average profile, even relatively small amplitude using this method will yield a neutrally stratified lower atmosphere. Nonlinear atmospheric responses will then appear at lower values of the "nonlinearity" parameter ε. Because of this, and because in the surface heating problem the heating depth H is no longer set externally, but rather determined by the boundary layer parameterization,

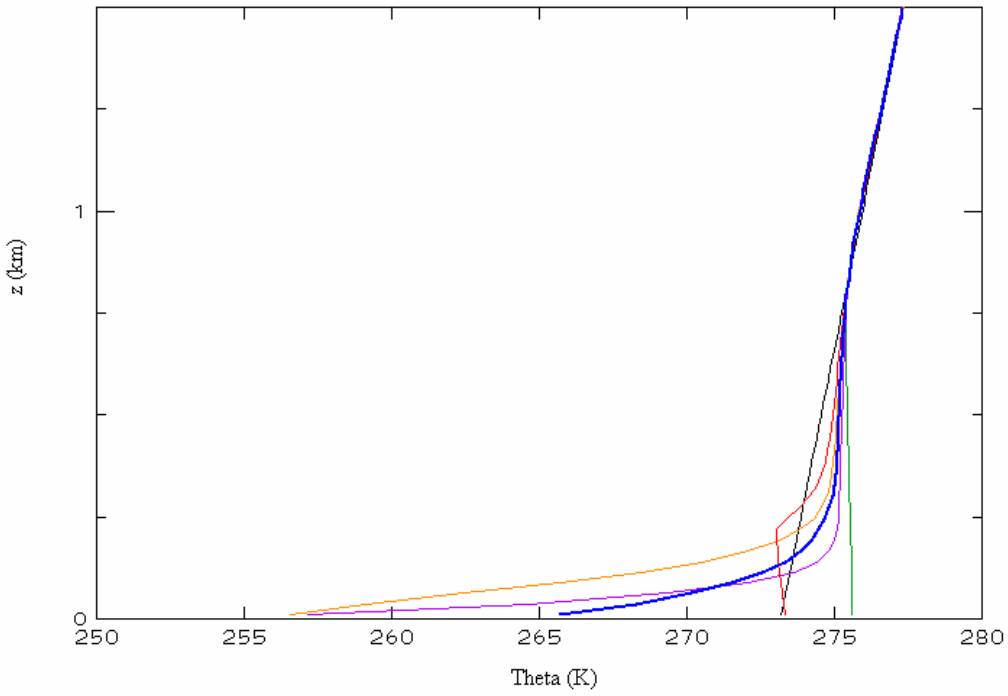

Fig. 33. θ profile from $\varepsilon = 0.50$ surface heating simulation with Newtonian damping at 0600 (yellow), 1200 (red), 1800 (green), 0000 (purple), and averaged over one day (blue). 550 km inland. Black line is background profile.

the scale analysis from Chapter III does not transfer to the surface heating problem. Thus, to perform a complete quantitative analysis on the full progression of the surface heating simulations to nonlinearity, it would be necessary to specify a background θ profile that matched the average θ profile.

The non-applicability of the scale analysis to the surface heating problem does not mean that the simulated atmospheric profiles are to be discarded. In fact, the average of potential temperature profile over all of the available August 30, 2000 sounding data from Houston, TX indicate that this average profile is somewhat realistic. The heavy blue line in Figure 34 shows this average. For comparison, a background state of N = 0.01 (with θ_0=306K) is overlaid on the plot as well. Note that, relative to the background stratification, the average θ profile exhibits a structure generally similar to that seen in the model average, with near constant static stability aloft and a highly stratified region near the surface. Reassignment of the background state is beyond the scope of this thesis. However, clever experiment design will allow us to glean as much analysis as possible from the current model setup. Most notably, we will be able to comment on the affect of changing heating method at small amplitude, as well as the evolution of high-amplitude simulations that produce a neutral or negatively stratified boundary layer.

i) Small Amplitude Surface Heating

At small amplitude, the discrepancy between the background and average temperature profiles is minimized. To analyze the small-amplitude surface heating

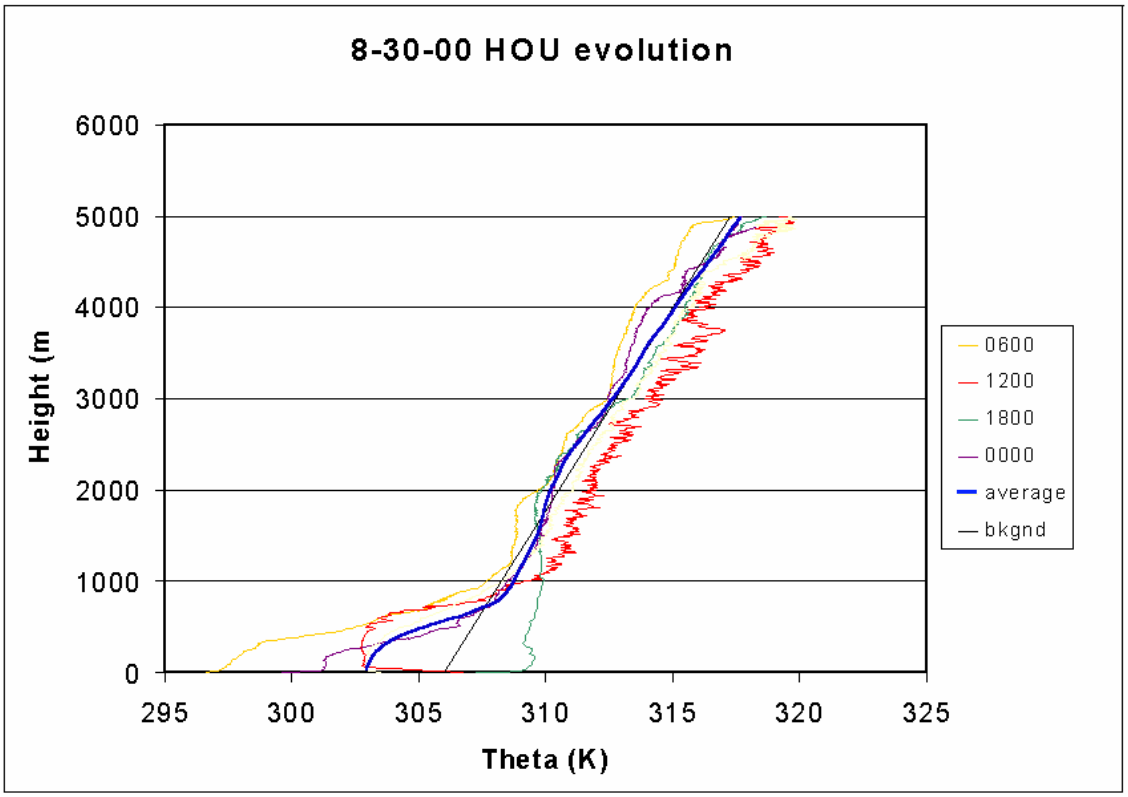

Fig. 34. Evolution of θ profile from Houston, Texas 8-30-00. Average profile is overlaid in blue, background state is estimated in black.

problem, the heating produced by the constant plus parameterized viscosity and the radiation in a large-amplitude surface heating simulation (illustrated in Figure 31) will be reapplied in a separate simulation as an interior heating shape.

As shown in Figure 35, the $\varepsilon = 0.50$ surface heating case (with Newtonian damping) had the deepest daytime mixed layer. However, due to numerical stability constraints, this simulation is much more computationally expensive than the $\varepsilon = 0.30$ case. As a compromise, the surface heating case at $\varepsilon = 0.4$ with Newtonian damping included is chosen to be the base run for specification of the new interior heating shape. The amplitude of that shape can then be modulated to produce a small-amplitude simulation that can be scaled and quantitatively analyzed. For simplicity, these new simulations will be referred to as the SFC-Interior (SFC-I) heating simulations.

Figure 36 shows the small-amplitude equatorial SFC-I solution that is equivalent in heating amplitude to the $\varepsilon = 0.001$ simulations described in the previous chapter. The response is dominated by the diurnal gravity wave signal, as it was in the interior heating problem (Figure 33). However, the difference in the wave fields produced by the two heating methods becomes apparent when large contour values are suppressed (Figure 36e), as higher gravity-wave harmonics are already being forced. These higher harmonic waves are due to the fact that the heat source in this case is not purely monotonic. To extract other differences due to the heating shape, the vertical velocity from the viscous $\varepsilon = 0.001$ interior heating simulation is overlaid on the small-amplitude SFC-I solution (Figure 37 top).

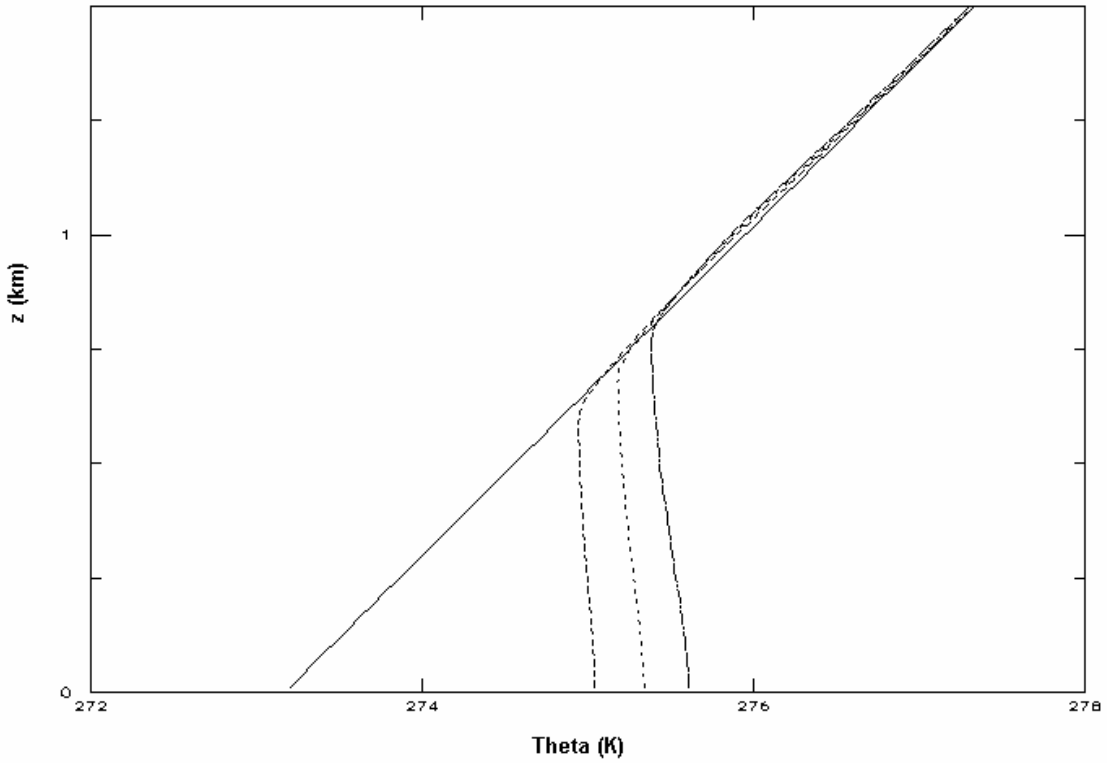

Fig. 35. θ profiles at day 4.25 from 550 km inland, ε = 0.30 (dash), ε = 0.40 (dot), and ε = 0.50 (dash-dot). All simulations include Newtonian damping. Solid line is background profile.

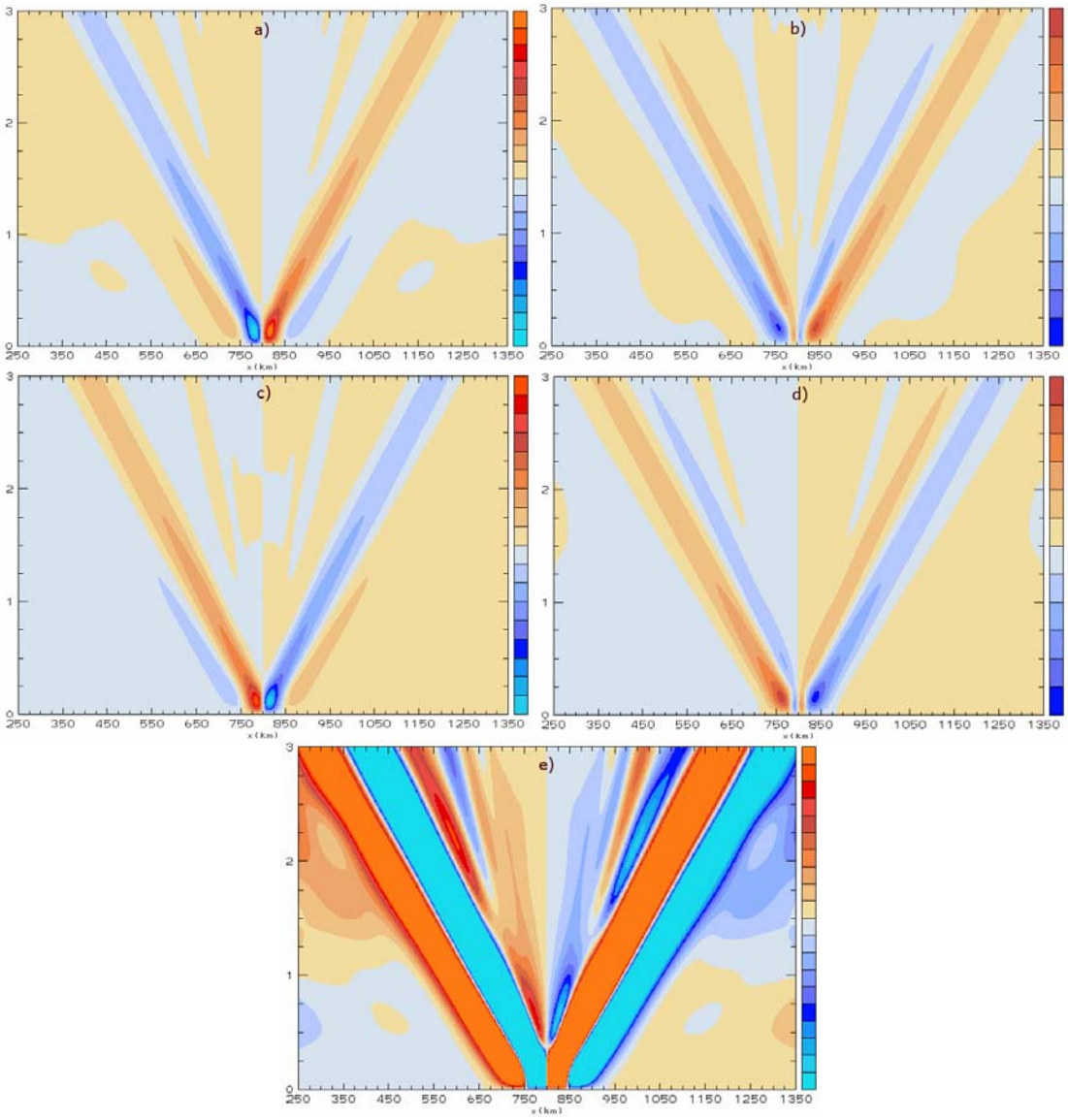

Fig. 36. Vertical velocities for the small-amplitude SFC-I simulation at day a) 4.25, b) 4.50, c) 4.75, and d) 5.00. e) 4.25 cycle time with threshold on larger contours. Horizontal and vertical axes are x and z (respectively) in kilometers. 0º latitude. Contour interval in a) – d) is 0.15. Interval in e) is 2.5 x 10^{-7}.

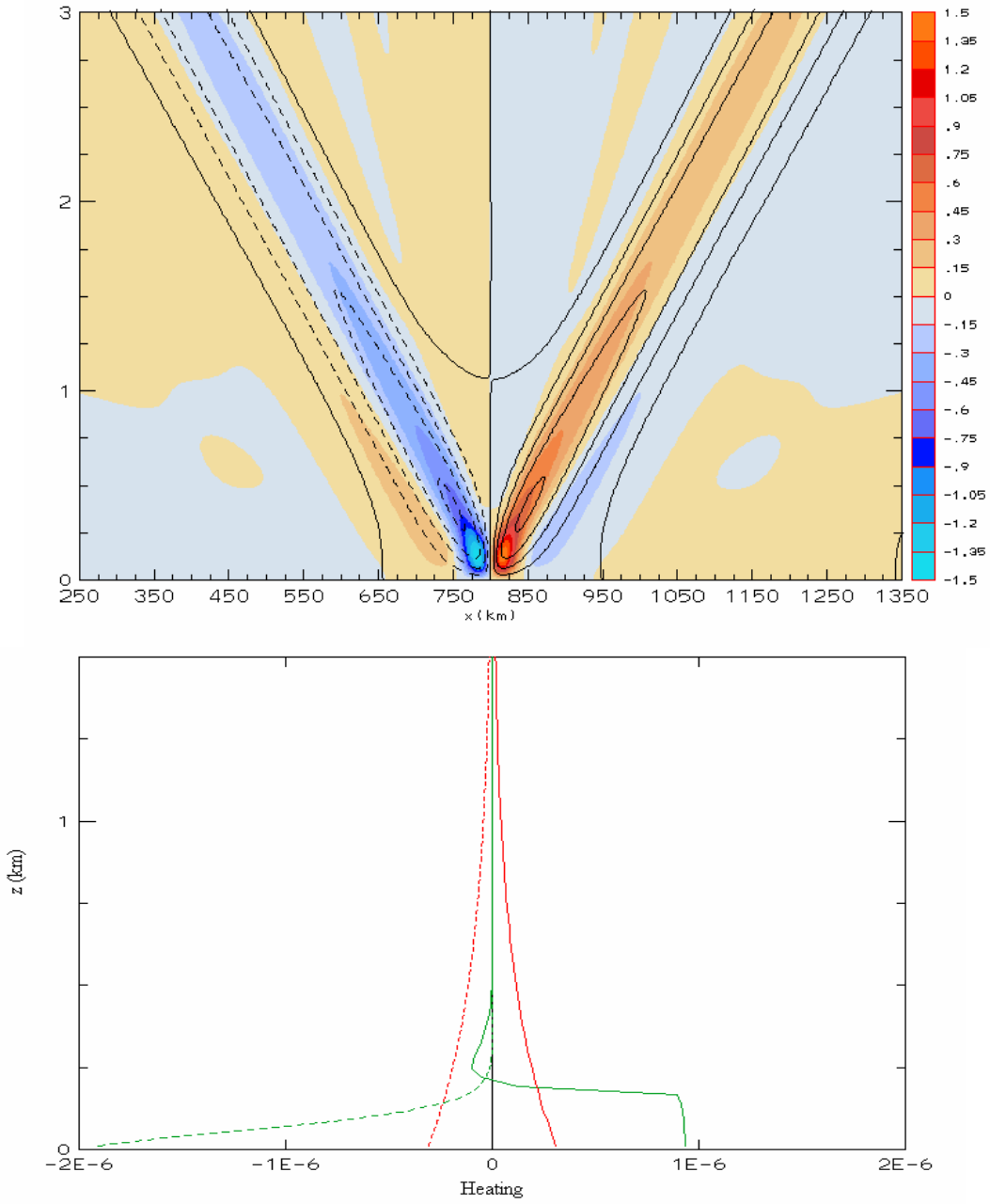

Fig. 37. (Top) Vertical velocities from small-amplitude SFC-I (color fill) and interior heating (line) at day 4.25. (Bottom) Corresponding effective heating for interior heating method (red) and SFC-I (green) simulations at day 4.0 (solid red/green) and 4.5 (dashed red/green). 0º latitude.

The most notable difference between the heating methods is that the maximum response in the SFC-I simulations is contracted vertically at the coast. This is because the effective forcing (Figure 37 bottom) with the SFC-I simulation is concentrated more in the low levels relative to the interior heating problem. The net gravity wave response can be thought of as a summation of gravity wave responses to the horizontal temperature gradient in each of an infinitesimal number of areas. Since the largest gradient is contracted vertically, so then is the maximum response.

Second, the ray path of the interior heating diurnal gravity wave is slightly lower in altitude than the SFC-I response. Since the SFC-I heating shape was formed by a vertical diffusion of heat, there is a slight time lag in the forcing with height due to the time scale of vertical heat transport. This effect is not present in the interior heating problem because the heating is instantaneously specified everywhere in the domain. Because the gravity wave ray paths propagate downward, we hypothesize that this apparent shift is actually the manifestation of the phase lag due to vertical diffusion of the forcing in the SFC-I simulation.

To analyze the time rate of change of the local horizontal temperature gradient, we recall again the frontogenetic forcing terms found in the previous chapter:

(36) $\varepsilon^{(1)}$ system:

$$\frac{\partial}{\partial t}\left|\frac{\partial b^{(1)}}{\partial x}\right| + u^{(0)}\frac{\partial}{\partial x}\left|\frac{\partial b^{(0)}}{\partial x}\right| + w^{(0)}\frac{\partial}{\partial z}\left|\frac{\partial b^{(0)}}{\partial x}\right| = -\frac{\partial u^{(0)}}{\partial x}\left|\frac{\partial b^{(0)}}{\partial x}\right| - \left(\frac{\partial w^{(0)}}{\partial x}\frac{\partial b^{(0)}}{\partial z} + N^2\frac{\partial w^{(0)}}{\partial x}\right)\frac{\dfrac{\partial b^{(0)}}{\partial x}}{\left|\dfrac{\partial b^{(0)}}{\partial x}\right|}$$

Plots of these forcing terms at the surface are shown for several cycle times in Figure 38. As in the interior heating experiment, the contraction term reaches a maximum 3 hours before the end of the heating and is similar in intensity for the sea and land breeze fronts. Also, in a local sense, the contraction term leads the advection term in phase by $-\pi/2$. Interestingly, the contraction term in this heating method is more comparable in magnitude to the advection term. In both cases, sea breeze and land breeze frontogenetic forcing are equal in magnitude.

At 45º latitude (Figure 39), there is no diurnal gravity wave to dominate the signal, so the higher harmonic gravity waves are clearly seen. The most notable of these waves is the semi-diurnal gravity wave, whose response amplitude is only a few times smaller than flows associated with near-coast responses. Similar to the interior heating problem, the maximum upward motion over land occurs at cycle time 4.00. However, this maximum in the upward motion is asymmetric in intensity with the upward motion over water at cycle time 4.50. In the interior heating case, the responses at small-amplitude were symmetric. We hypothesize that this asymmetry is due to asymmetry in the strength of the day/night heating/cooling relative to the background state.

As in the interior heating case, the contraction term (Lagrangian frontogenetic forcing at the surface) is about 50% smaller at 45º than it is at the equator. Again, this result is probably due to the magnitude of the Coriolis force at this high latitude. Similar to the 45º interior heating case, the advection and contraction terms (Figure 40) in the small-amplitude SFC-I simulation at 45º are in phase.

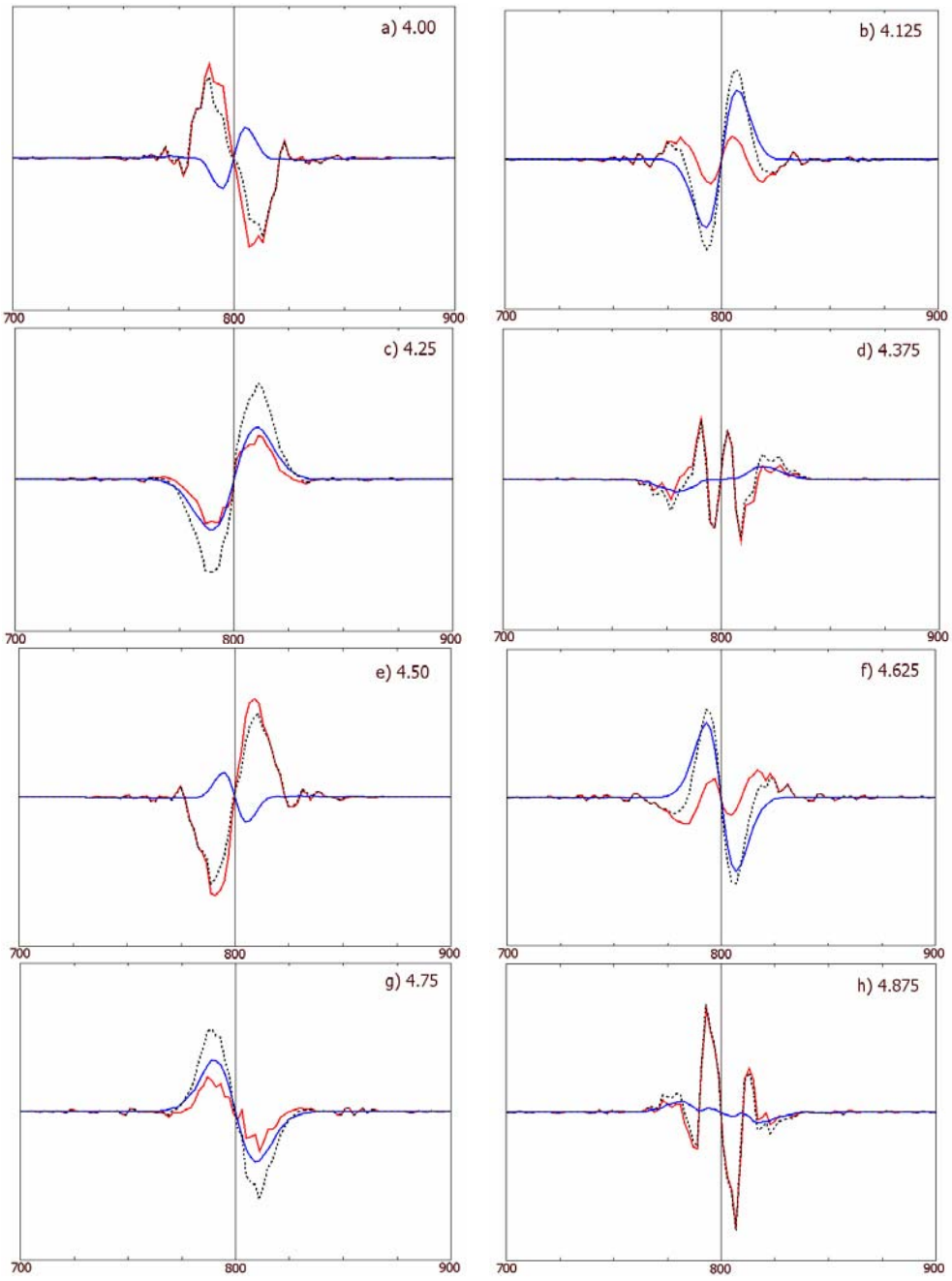

Fig. 38. Surface frontogenetic forcing in the small-amplitude SFC-I simulation due to advection (red) and contraction (blue) at day a) 4.00, b) 4.125, c) 4.25, d) 4.375, e) 4.50, f) 4.625, g) 4.75, and h) 4.875. The sum of both forcing terms is black dash. 0º latitude. Vertical line indicates coast. Vertical axis scale is 1.5 x 10^{-15}.

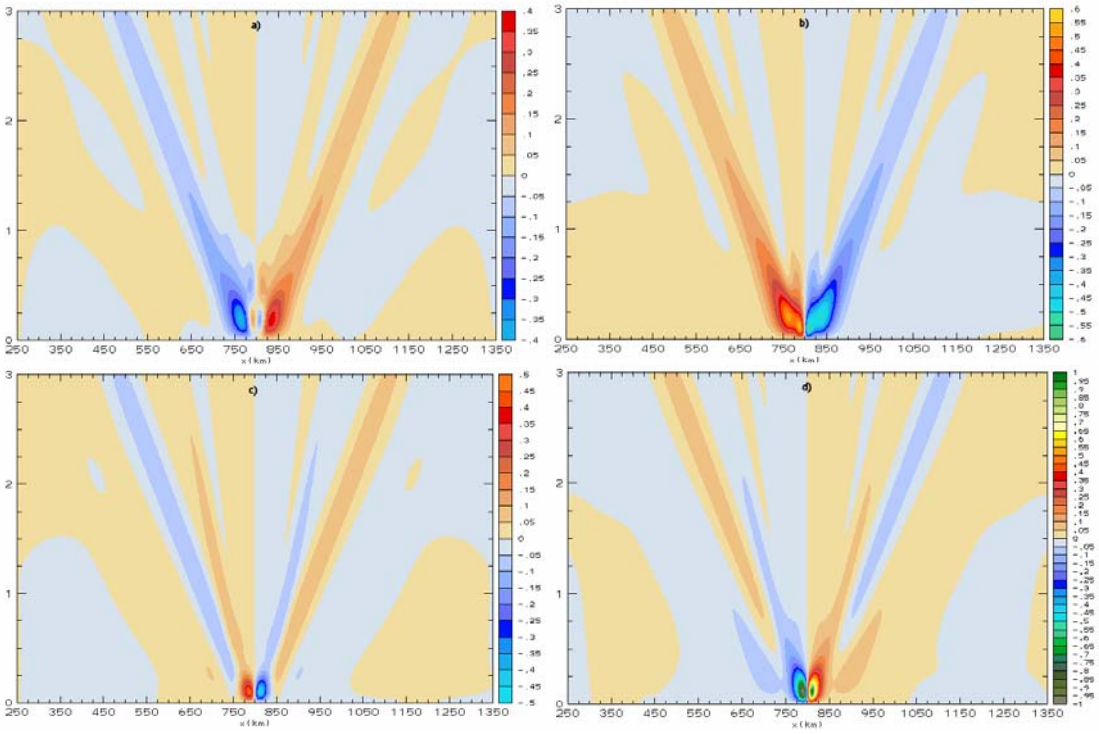

Fig. 39. Vertical velocities for the small-amplitude SFC-I simulation at day a) 4.25, b) 4.50, c) 4.75, and d) 5.00. 45º latitude. Horizontal and vertical axes are x and z (respectively) in kilometers. Contour interval is constant throughout.

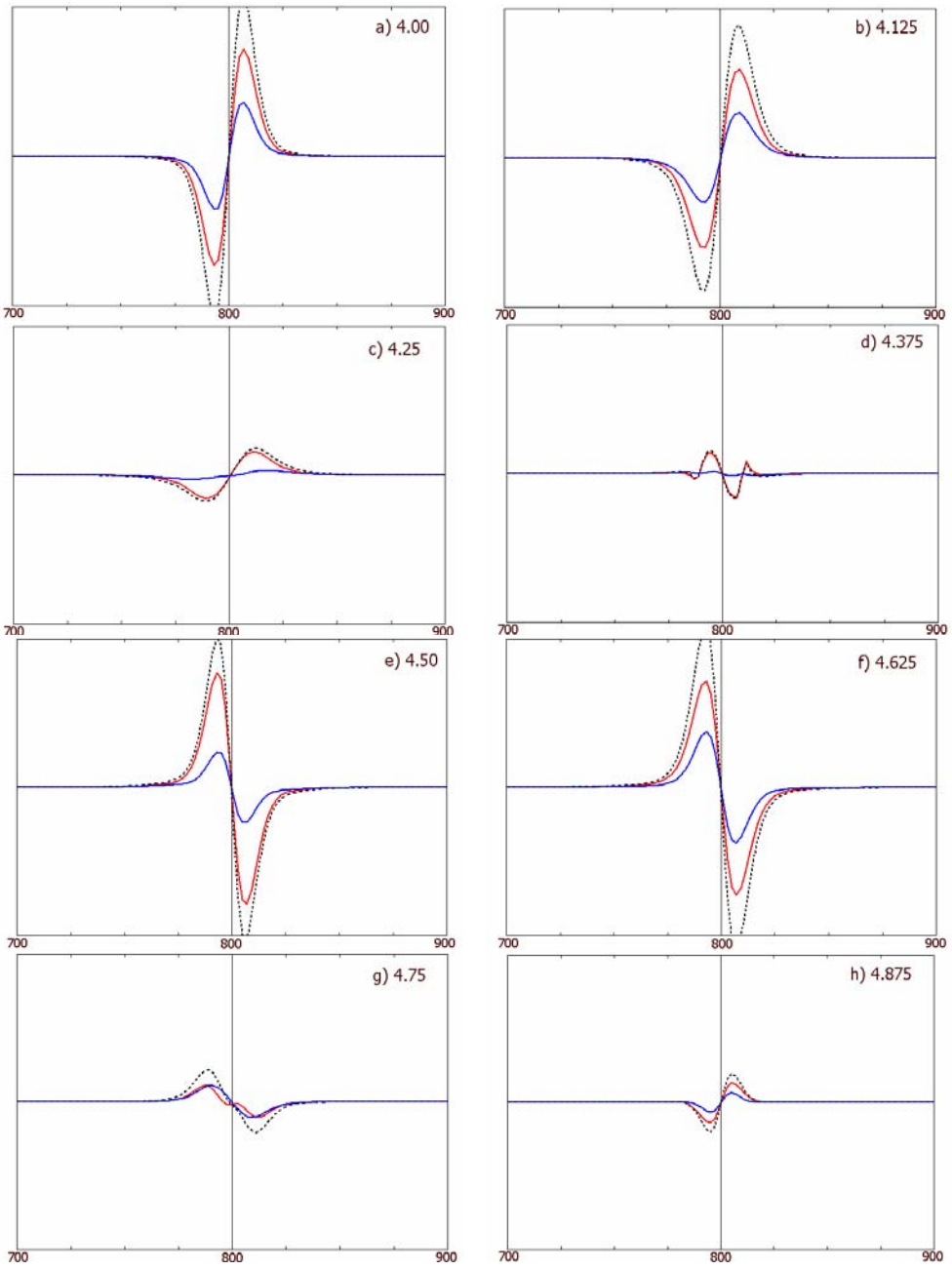

Fig. 40. Surface frontogenetic forcing in the small-amplitude SFC-I simulation due to advection (red) and contraction (blue) at day a) 4.00, b) 4.125, c) 4.25, d) 4.375, e) 4.50, f) 4.625, g) 4.75, and h) 4.875. The sum of both forcing terms is black dash. 45º latitude. Vertical line indicates coast. Vertical axis scale is 1.5 x 10^{-15}.

ii) Large Amplitude Surface Heating

Next, we experiment with the large-amplitude surface heating problem directly (i.e., without re-specifying the convective heating as an interior heating) with radiative damping included as well. In this section, the simulations are performed at a heating amplitude equivalent to that which equaled an $\varepsilon = 0.40$ in the interior heating case. For simplicity, these experiments will simply be referred to as the surface heating simulations.

In the small-amplitude surface heating experiments, we found the maximum of the response to be contracted vertically due to the vertical concentration of the heating with respect to the interior heating method. Due to this higher concentration of heating at low levels, we expect the high-amplitude surface heating case to exhibit much more dramatic low-level heating than the high-amplitude interior heating experiments, and thus a higher degree of nonlinearity than previously obtained.

This expectation appears to be correct, as the high-amplitude surface heating simulations all exhibit a well-mixed boundary layer developing slightly negative static stability through a large portion of the warm cycle (Figure 41). As a result, the motions that are driven in these simulations are very nonlinear (Figure 42). At cycle time 4.25, a strong frontal feature has started to develop just inland from the coast. Progressing through the cycle, the atmospheric response is clearly dominated by frontal discontinuities propagating both onshore and off, away from the coastline.

This negative stability layer appears to have important implications on the development and propagation speed of developing fronts. At the end of the heating

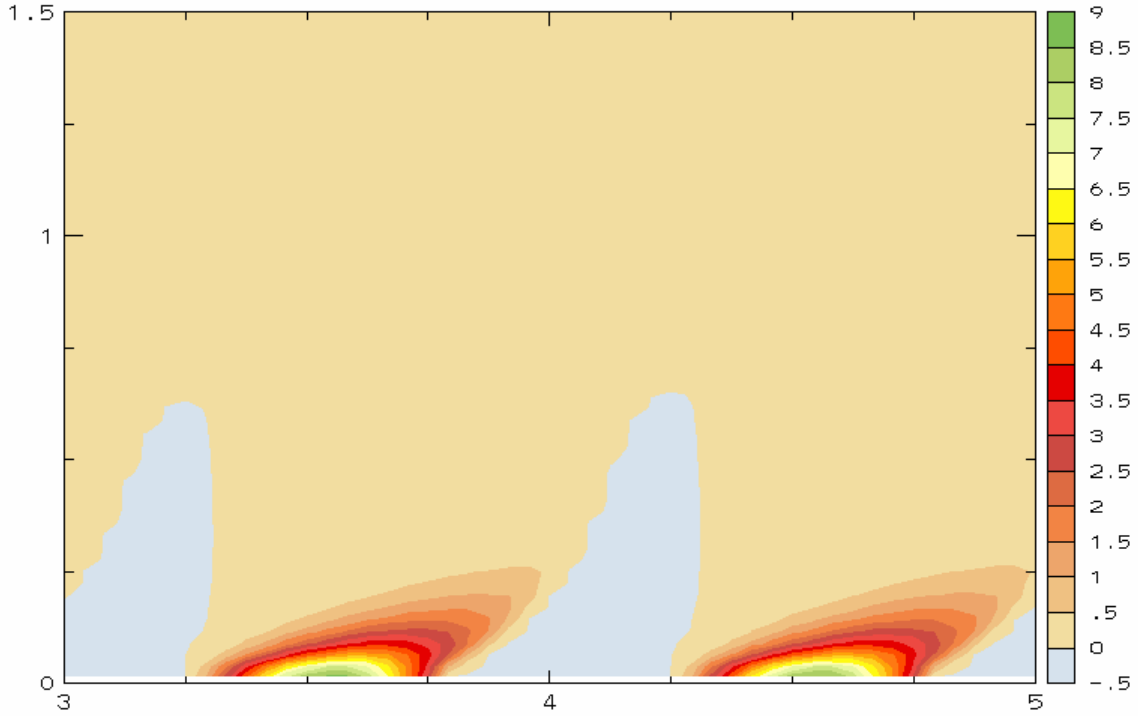

Fig. 41. Brunt-Vaisala frequency ($1x10^{-3}$) vs. height from the large amplitude surface heating simulations. 550 km inland. 0º latitude.

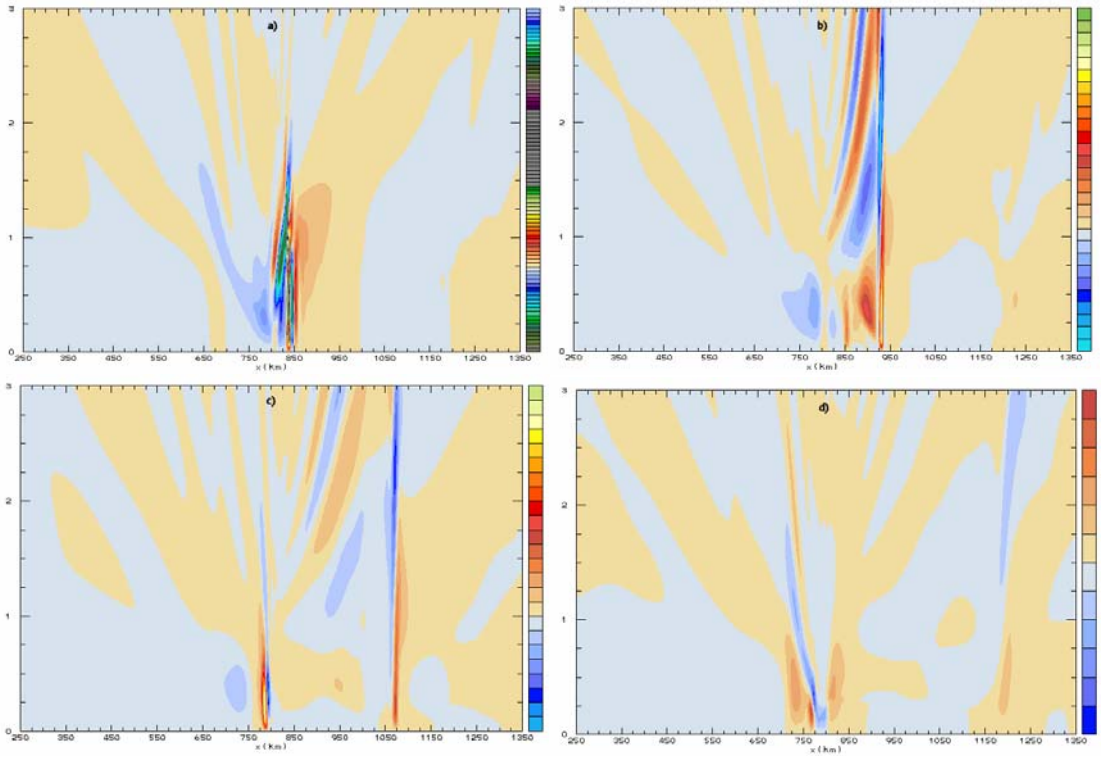

Fig. 42. Vertical velocities for the large-amplitude surface heating simulation at day a) 4.25, b) 4.50, c) 4.75, and d) 5.00. 0º latitude. Horizontal and vertical axes are x and z (respectively) in kilometers. Contour interval is constant throughout.

(cycle time 4.25), a mixed layer nearly 1 km deep has developed just inland from the coast. As cooler air is advected inland behind the developing sea breeze front, the horizontal temperature gradient tightens. As the front begins to intensify, there is a brief period where a wave train develops in the vertical motion field. This wave train, seen in Figure 43, has a wavelength of about $10\Delta x$, and is therefore not believed to be model artifact, but rather vertical motions briefly trapped in the well-mixed layer below the highly stratified background profile aloft.

As shown in Figure 44, the sea breeze front propagates rapidly inland, first at a speed of 14 km/h, then increasing to nearly 25 km/h during the second half of the cooling phase. A distinguishable vertical motion signal associated with the sea breeze front endures for almost one entire cycle, and dissipates at a distance of 400 km inland. The land breeze front at 0º is fairly pronounced initially, but propagates only 75 km offshore over a duration of one-quarter cycle before dissipating. This asymmetry in frontal propagation is also evident in the horizontal wind field. In the high-amplitude surface heating case, the magnitude, horizontal extent, and depth of the onshore flow greatly exceeds that of the offshore flow. Presumably, this asymmetry in the strength of the sea and land breeze fronts is at least partially due to the high static stability of the environment over water. Unlike the sea breeze, the land breeze has no well-mixed negatively stratified layer in which to intensify. As a result, the front is less significant in vertical motion, propagation speed, and duration.

At high-amplitude in the surface heating case, there seems to be little if any discernable diurnal gravity wave signal left in the atmospheric response, as the motions

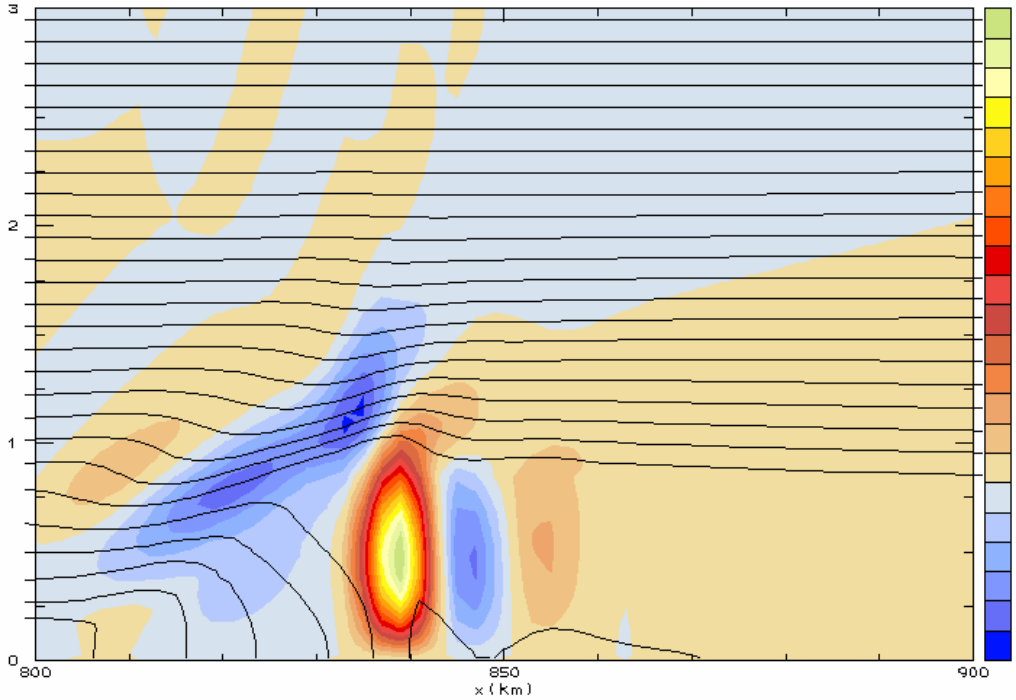

Fig. 43. Vertical velocity (color fill) and θ (line) for the large-amplitude surface heating simulation at day 4.25, 0º latitude. Horizontal and vertical axes are x and z (respectively) in kilometers.

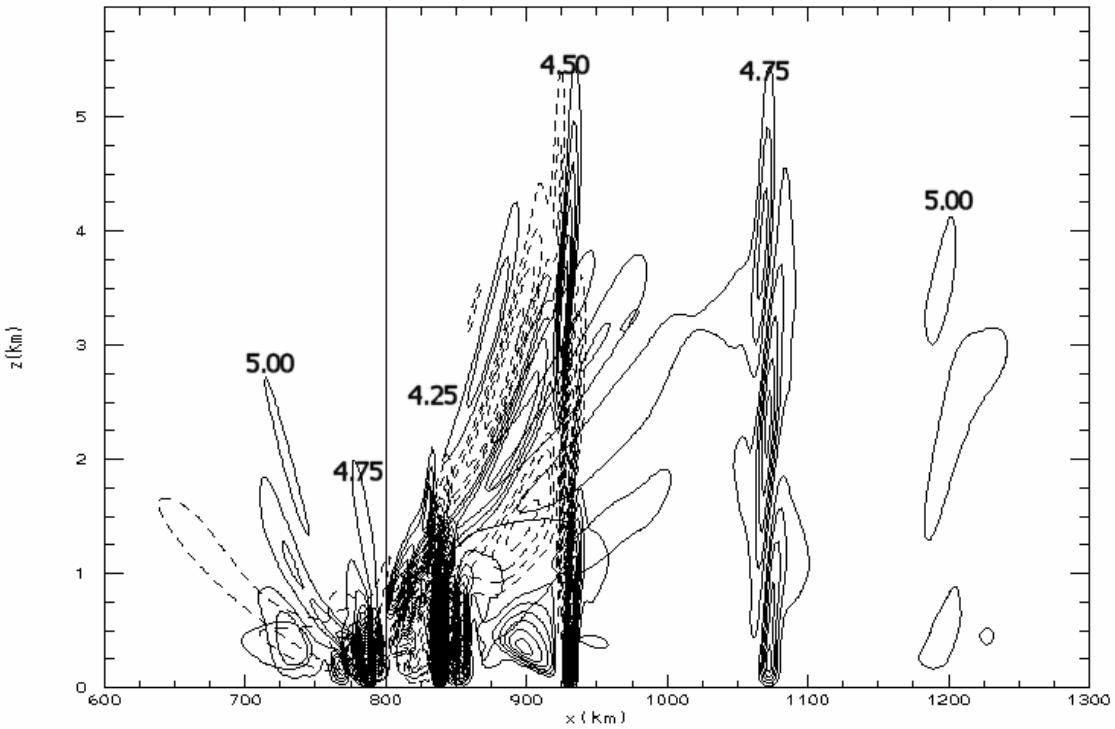

Fig. 44. Temporal snapshots of vertical velocity at 600-1300 km for 0º large-amplitude surface heating simulation. Contour interval is consistent throughout. Vertical line indicates coast.

have become dominated by fronts and higher-harmonic gravity waves. In addition, the horizontal surface wind is dominated by onshore flow. As mentioned, the sea breeze is much more prominent than the land breeze in magnitude and horizontal extent. The asymmetry between the sea and land breezes in the surface heating case is much more dramatic than was seen in the high-amplitude interior heating case.

At 45º latitude (Figure 45), the first indication is that the evolution of the atmospheric response is not very different from the equatorial experiment. During the heating cycle, frontal discontinuities still form near the coast in a weakly unstable planetary boundary layer and propagate inland. At night, they form and propagate offshore. Interestingly, the land breeze front at 45º seems to be strengthened relative to the equatorial case. Presumably, this decrease in sea/land breeze asymmetry from the equatorial case is due to the strong Coriolis force at this latitude, which acts to turn the sea breeze flow and, in effect, convert some of the sea breeze momentum into land breeze momentum. Because of the Coriolis force, the difference between the high-amplitude surface heating case and the high amplitude interior heating case is less at 45º than at the equator.

Zooming in on the development of the daytime sea breeze front (Figure 46) a vertical circulation, ducted by the steep stability gradient at the top of the mixed layer, develops on the nose of a horizontal temperature gradient that marks the inland penetration of marine air. The main difference in this case is that the sea breeze front, being acted upon by the strong Coriolis force at 45º, is confined to roughly 100 km of the coastline, as is the nocturnal land breeze (Figure 47).

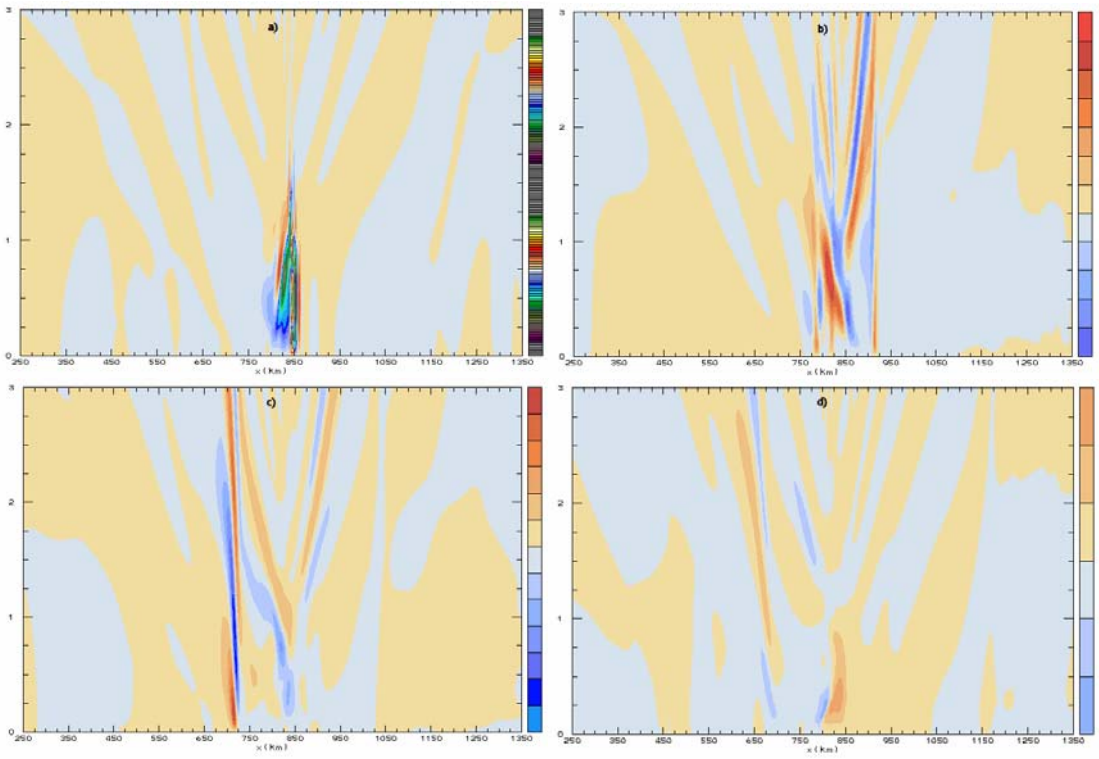

Fig. 45. Vertical velocities for the large-amplitude surface heating simulation at day a) 4.25, b) 4.50, c) 4.75, and d) 5.00. 45º latitude. Horizontal and vertical axes are x and z (respectively) in kilometers. Contour interval is constant throughout.

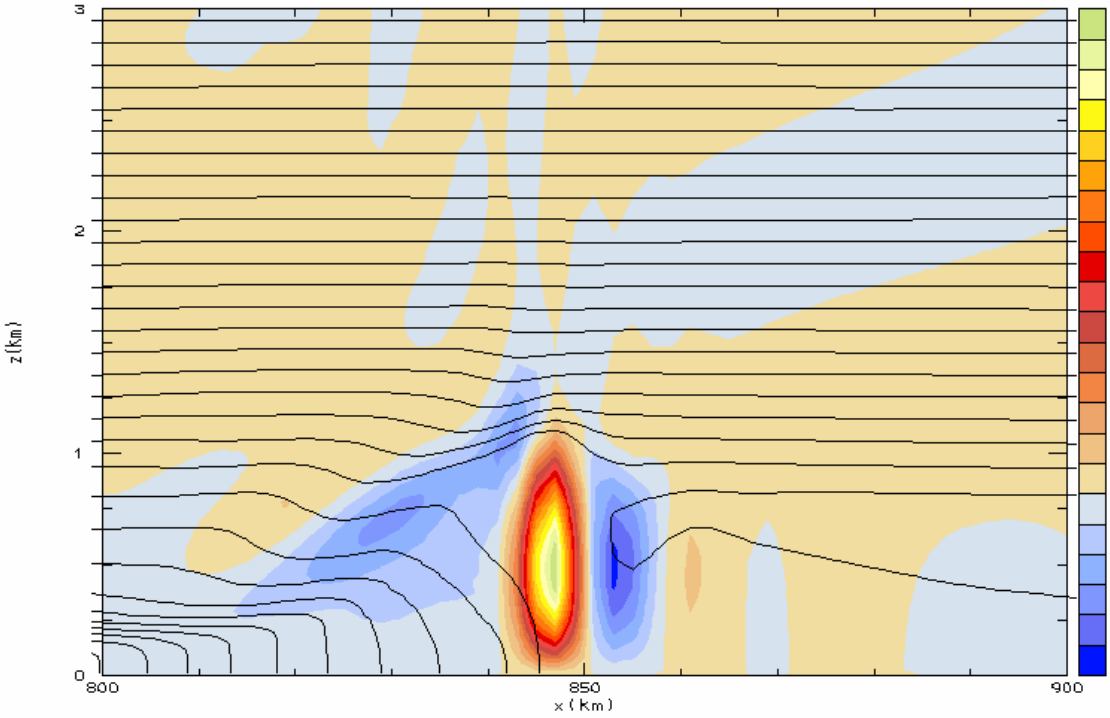

Fig. 46. Vertical velocity (color fill) and θ (line) for the large-amplitude surface heating simulation at day 4.25, 45º latitude. Horizontal and vertical axes are x and z (respectively) in kilometers.

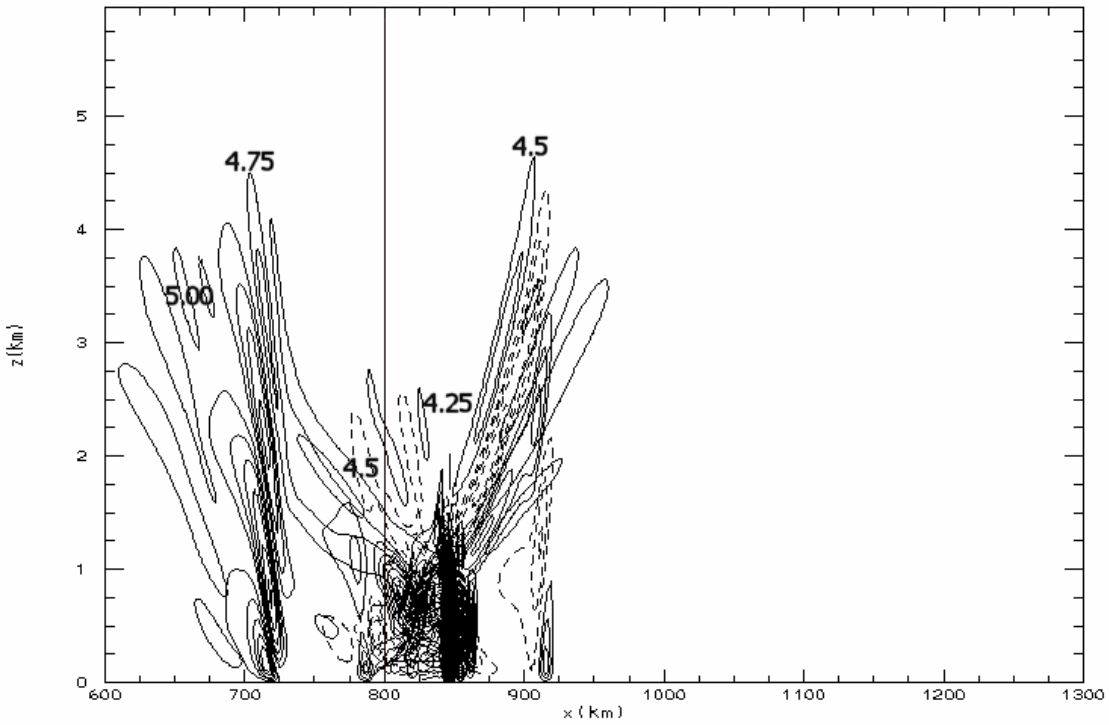

Fig. 47. Temporal snapshots of vertical velocity at 600-1300 km for 45º large-amplitude surface heating simulation. Contour interval is consistent throughout. Vertical line indicates coast.

Finally, we briefly consider the large-amplitude surface heating response near the crossover latitude of 30º, where linear theory predicts an abrupt change in solution type. Figure 48 shows the time evolution of the vertical velocity field at the latitudes of 29º, 30º, and 31º. At all latitudes, frontal discontinuities continue as the dominant atmospheric response to the applied forcing. At forcing amplitudes such as these, where a deep neutral or negative static stability layer develops during the day, there seems to be little sensitivity to crossing the resonant latitude. Only propagation of the front seems to be effected by variations in latitude.

Though these highest amplitude solutions are very nonlinear in their local atmospheric responses, there are still some aspects of the response predicted reasonably well by linear theory. The bulk atmospheric response from the surface heating experiment, as measured by the circulation

$$C = \iint \left(\frac{\partial u}{\partial z} - \frac{\partial w}{\partial x} \right) dA$$

at 0º, 29º, 30º, 31º, and 45º is compared in Figure 49 to the temporal variation of circulation from the high-amplitude interior heating experiments. The circulations at 0º in both the nonlinear interior heating simulations and the nonlinear surface heating simulations both oscillate such that the maximum onshore flow is reached at the time of peak cooling, $-\pi$ out of phase with the forcing. At 45º, the circulations in both heating experiments oscillate such that the maximum onshore flow occurs at the time of peak heating, thus being in phase with the forcing. Both of these results are in agreement with the predictions of linear theory. Perhaps of greater interest in the high-amplitude

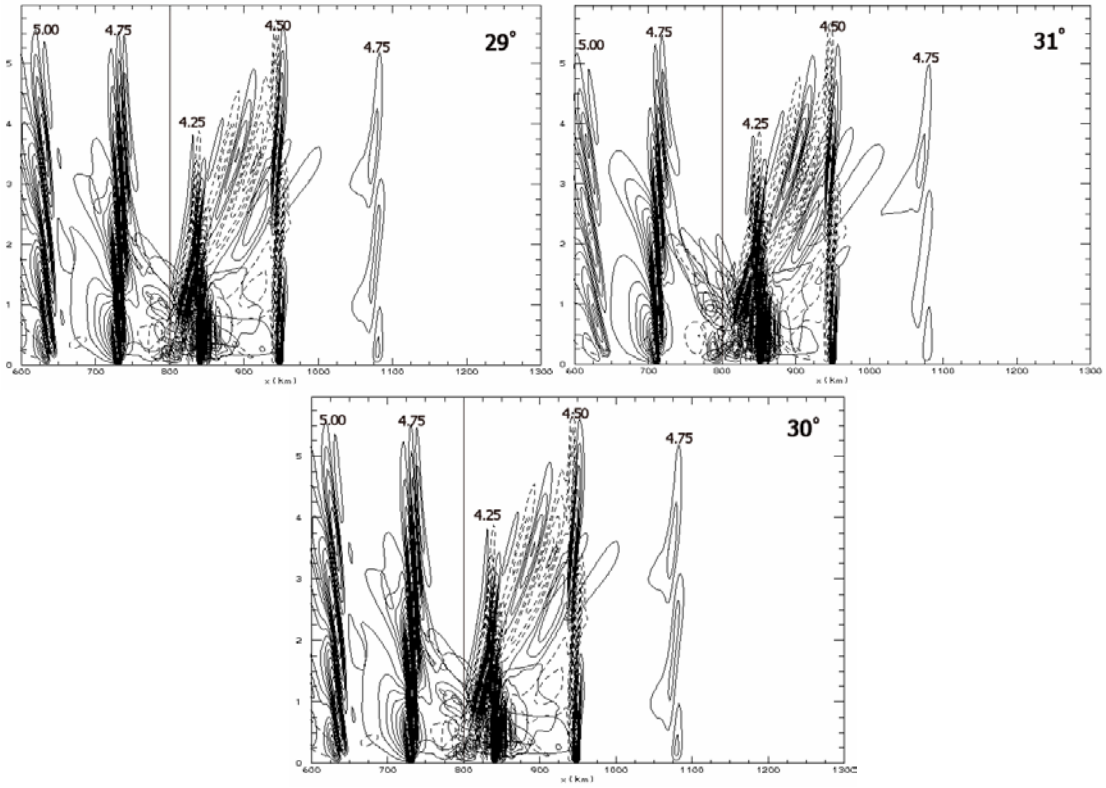

Fig. 48. Temporal snapshots of nondimensionalized vertical velocity at 600-1300 km for 45º large-amplitude surface heating simulation at 29º, 30º, and 31º latitude. Contour interval is consistent throughout. Vertical line indicates coast.

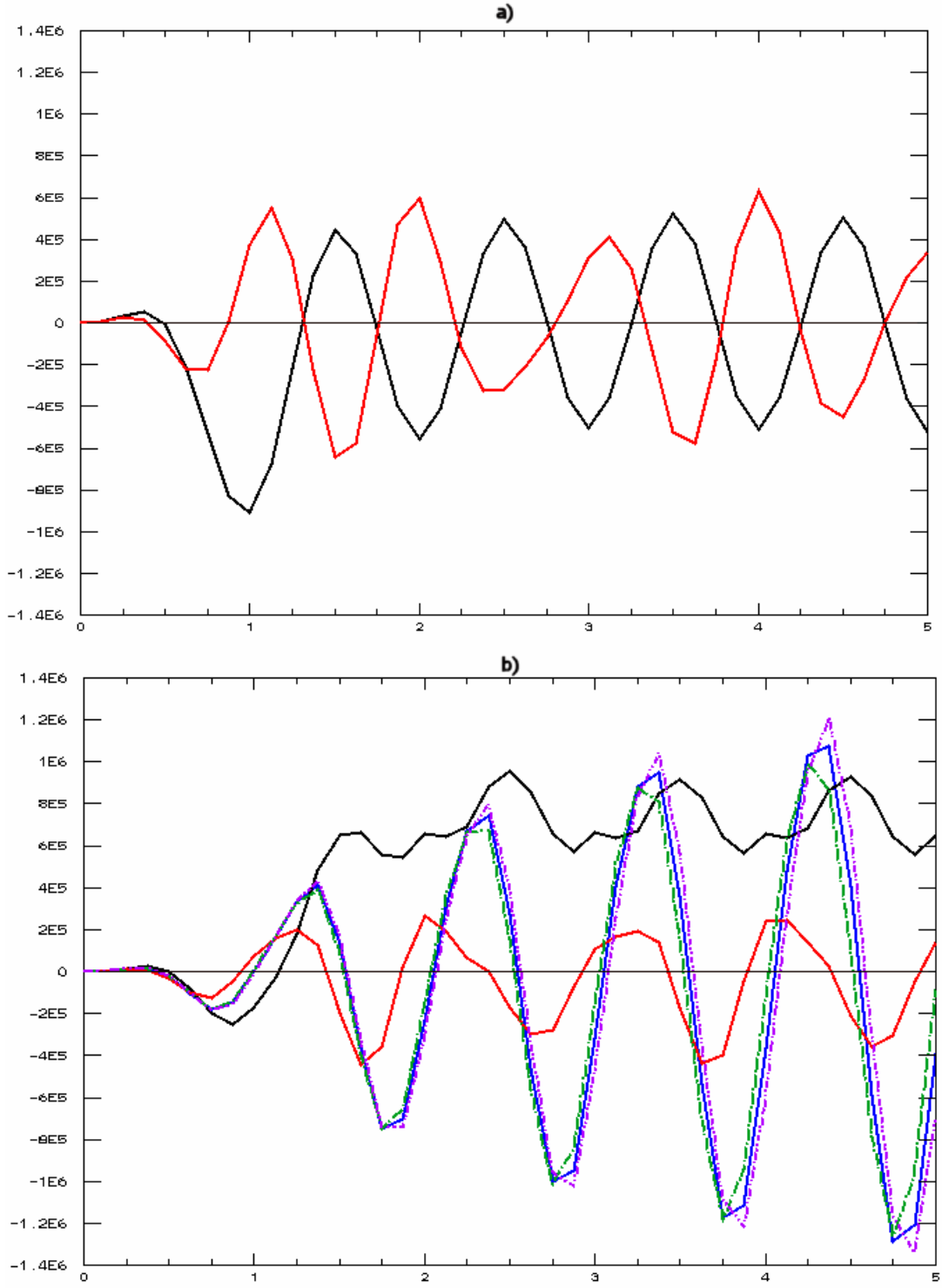

Fig. 49. Circulation (m^2/s) vs. Time (days) for the a) interior heating experiment at 0º (black) and 45º (black), and b) for the surface heating experiment at 0º (black), 29º (violet), 30º (blue), 31º (green), and 45º (red).

surface heating experiments is the net onshore bias of the circulation in the equatorial case. Yan and Anthes (1987) found this same bias and attributed it to the fact that in their simulations the temperature over land never cooled below the temperature of the water. Herein lies the motivation for modulating the amplitude of the heating by $\cos(\omega t)$ rather than $\sin(\omega t)$. This change ensures that the net amount of energy added to the system over one day is exactly zero. Aside from the phase shift, the steady-state solution will remain unchanged. In this work, the cooling over land certainly exceeds that over the water, yet the same result has been obtained. This result also appears not to be due to large heating amplitude or the development of a neutral mixed layer, as the high-amplitude interior heating experiments met both of these criteria and still oscillated about a zero mean. Thus, we hypothesize that this onshore bias either results from the discrepancy between the average and background θ profiles or the inclusion of Newtonian damping in the surface heating experiment. Regardless, the absence of this effect in the high-amplitude interior heating case leads us to believe that the result is somehow related to the fact that net temperature change at any vertical level integrated throughout one day is not constrained to be zero.

CHAPTER VI

CONCLUSIONS AND FUTURE WORK

The response of the land and sea breeze circulation to two highly simplified dynamical models has been presented. For the first simplified model (interior heating), a weakly nonlinear analysis was used to investigate nonlinear tendencies of the solution and their sources. The dependence on latitude was also tested. In the second simplified model (surface heating), a qualitative comparison was used to test the dependence of the response on heating amplitude and latitude.

In the interior heating case, the addition of viscosity causes a 33% decrease in the atmospheric motions of the gravity wave ray path at 0º. This decrease is accompanied by a 25% decrease in domain-wide kinetic energy, however the magnitude of the horizontal surface wind associated with the sea breeze is only reduced by less than 10%.

One manifestation of nonlinearity in the equatorial interior heating case is the introduction of the semi-diurnal gravity wave harmonic, which is due to the semi-diurnal oscillation of cold air advection at the coastline at 0º. At 45º, a semi-diurnal harmonic is initiated by the semi-diurnal oscillation of cold air advection, however it is $-\pi$ out of phase with the net first correction response, leading us to believe that the majority of the forcing for the semi-diurnal gravity wave at 45º is from the remaining nonzero linear advection terms. More interestingly, the net cold-bias of the advection at the coast at both 0º and 45º seems to force a cycle-mean flow that is divergent at the surface and convergent aloft near 250 m. At 45º, the presence of the Coriolis force leads

then to a mean shore-parallel response in addition to the shore-perpendicular surface divergence, and thus dramatically limits the horizontal extent of this mean circulation. This feature is clearly evident not only in the weakly nonlinear analysis, but in the highest amplitude interior heating simulations at both 0º and 45º.

Another manifestation of nonlinearity in the interior heating case is frontogenesis. Though frontogenetic forcing terms are present at even the smallest heating amplitude, fronts that propagate away from the coastline as density currents do not begin to form until ε surpasses the value 0.20. At 45º, frontogenetic forcing is about 50% smaller than the equatorial magnitude because of the phase of maximum shore-perpendicular wind at that latitude. Also, because of the presence of a strong Coriolis force, fronts that form at 45º do not propagate far from the coast, and do not exhibit vertically propagating non-hydrostatic gravity waves. This said, the transition of the simulation set to nonlinearity at 45º is much slower than the transition at 0º, again due to the presence of the Coriolis force. In addition, asymmetries in the strength of the onshore and offshore coast-local flows are found to be due to variations in stratification. Even at high heating amplitude, linear theory still exactly predicts the phase and magnitude of the bulk atmospheric circulation for both 0º and 45º in the interior heating case.

When the heating method is changed to more adequately represent the real atmosphere, it is found that higher-harmonic gravity waves are forced in even the small-amplitude solution at both 0º and 45º. These waves are the result of the non-monotonic heating shape itself. Another direct result of changing the heating shape is a slight

phase-lag in the diurnal gravity waves at 0º. We hypothesize that this phase lag is due to the additional time scale necessary for vertical heat diffusion in the surface heating solution. In addition, the maximum response in the diurnal gravity wave ray paths is contracted vertically. This effect is due to the notable low-level bias in the effective heating profile, which itself is a result of an asymmetric magnitude of surface cooling in the surface heating case. The addition of Newtonian damping in this heating method causes a further damping of the diurnal gravity wave by about 25%. At 45º, no diurnal gravity wave is present. Lagrangian frontogenetic forcing is again shown to be 50% smaller at 45º than at the equator.

At high heating amplitude, the development of a significant neutral or negatively stratified boundary layer permits the generation of significant frontal discontinuities at all latitudes. Comparison of frontal propagation throughout the planetary continuum shows that Coriolis force is significant only in determining the magnitude of frontal propagation, and does not appear to play a role in determining the character of the response as in linear theory. However, even at high heating amplitudes (i.e. in the most nonlinear simulations), linear theory still predicted the phase of the bulk atmospheric circulation perfectly. Consistent with previous studies (Yan and Anthes, 1987), a net onshore bias at 0º and steadily increasing amplitude near 30º was found in the circulation in the surface heating case. We hypothesize this onshore bias to be the result of the net temperature change at any vertical level through one day is not constrained to be zero. Furthermore, the cycle-mean surface divergence (at 0º and 45º) and attendant shore-

parallel circulation (at 45º only) found in the interior heating case are not distinguishable in the high amplitude surface heating simulation.

Future work in this area should include the specification of a background temperature profile that matches the cycle-mean profile for the surface heating case. With this specification, the evolution in linearity of the surface heating simulations could be more quantitatively addressed. In addition, relaxation of a simulation to this mean profile with no diurnal forcing would isolate any resultant cycle-mean circulations. Along those same lines, a high-amplitude interior heating simulation with Newtonian damping included may give insight to the any cycle-mean responses due specifically to the introduction of that parameterization.

Additional research could use experiments similar to those done here to test the effects of factors like background synoptic flow and varied coastal transition zone width on the atmospheric response. In addition, three-dimension (spatial) modeling could investigate the effects of coastline shape and even the presence of significant inland topography, as Mapes et al. (2003) find evidence that gravity wave generation from inland topography may play as much or more of a role than the coastline in the initiation of nocturnal offshore convection. Finally, designing an experiment to track tracers throughout the model domain with time could implicate how the atmospheric responses discussed in this work impact the transport of airborne materials in a coastal environment.

REFERENCES

Dalu, G.A., and R.A. Pielke, 1989: An analytical study of the sea breeze. *J. Atmo. Sci*., **46**, 1815-1825.

Epifanio, Craig C., D.R. Durran, 2001: Three-dimensional effects in high-drag-state flows over long ridges. *J. Atmo. Sci.,* **58**, 1051–1065.

Imaoka, K., and R.W. Spencer, 2000: Diurnal variation of precipitation over the tropical oceans observed by TRMM/TMI combined with SSM/I. *J. Climate*, **13**, 4149-4158.

Klemp, J.B., and R.B. Wilhelmson, 1978: The simulation of three-dimensional convective storm dynamics. *J. Atmo. Sci*., **35**, 1070-1096.

Lilly, D.K., 1962: On the numerical simulation of buoyant convection. *Tellus*, **14**, 148-172.

Mapes, B.E., Thomas T. Warner, and Mei Xu, 2003: Diurnal rainfall in northwestern South America. Part III: Diurnal gravity waves and nocturnal convection offshore. *Mon. Wea. Rev*., **131**, 830-844.

Negri, A.J., R.F. Adler, E.J. Nelkin, and G.J. Huffman, 1994: Regional rainfall climatologies derived from Special Sensor Microwave Imager (SSM/I) data. *Bull. Amer. Meteor. Soc*., **75**, 1165-1182.

Negri, A.J., E.N. Anagnostou, and R.F. Adler, 2000: A 10-yr climatology of Amazonian rainfall derived from passive microwave satellite observations. *J. Appl. Meteor*., **39**, 42-56.

Nielsen-Gammon, J., 2001: Initial modeling of the August 2000 Houston-Galveston ozone episode (Dec. 19, 2001 interim report). Obtained from http://www.met.tamu.edu/results/. Accessed June 2003.

Niino, H., 1987: The linear theory of the sea breeze circulation. *J. Meteor. Soc. Japan*, **65**, 901-920.

Persson, P.O.G., and T.T. Warner, 1991: Model generation of spurious gravity waves due to inconsistency of the vertical and horizontal resolution. *Mon. Wea. Rev*., **119**, 917-935.

Rotunno, R., 1983: On the linear theory of the land and sea breeze. *J. Atmo. Sci*., **40**, 1999-2009.

Yan, H., and R.A. Anthes, 1987: The effect of latitude on the sea breeze. *Mon. Wea. Rev*., **115**, 936-956.

Yang, G.-Y., and J. Slingo, 2001: The diurnal cycle in the tropics. *Mon. Wea. Rev.*, **129**, 784-801.

Supplemental Sources

Adler, R. F., and A. J. Negri, 1988: A satellite infrared technique to estimate tropical convective and stratiform rainfall. *J. Appl. Meteor.,* **27,** 30–51.

Arkin, P. A., and B. N. Meisner, 1987: The relationship between large-scale convective rainfall and cloud cover over the western hemisphere during 1982–1984. *Mon. Wea. Rev.,* **115,** 51–74.

Arritt, R.W., 1992: Effects of the large-scale flow on characteristic features of the sea breeze. *J. Appl. Meteor*., **32**, 116-125.

Arritt, R.W., 1989: Numerical modelling of the offshore extent of sea breezes. *Quart. J. Roy. Meteor. Soc*., **115**, 547-570.

Baker, R.D., B.H. Lynn, A. Boone, W.-K. Tao, and J. Simpson, 2001: The influence of soil moisture, coastline curvature, and land-breeze circulations on sea-breeze-initiated precipitation. *J. Hydrometeor*., **2**, 193-211.

Berberry, E.H., 2001: Mesoscale moisture analysis of the North American monsoon. *J. Climate*, **14**, 121-137.

Buckley, R.L., and R.J. Kurzeja, 1997: An observational and numerical study of the nocturnal sea breeze. Part I: structure and circulation. *J. Appl. Meteor.*, **36**, 1577-1598.

Chen, G.T.-J., S.-Y. Chen, and M.-H. Yan, 1983: The winter diurnal circulation and its influence on precipitation over the coastal area of northern Taiwan. *Mon. Wea. Rev.*, **111**, 2269-2274.

Chen, S.S., and R.A. Houze, 1997: Diurnal variation and life-cycle of deep convective systems over the tropical Pacific warm pool.. *Quart. J. Roy. Meteor. Soc.*, **123**, 357-388.

Dai, A., 2000: Global precipitation and thunderstorm frequencies. Part II: Diurnal variations. *J. Climate*, **14**, 1112-1128.

Dai, Aiguo, and Junhong Wang, 1999: Diurnal and semidiurnal tides in global surface pressure fields**.** *J. Atmo. Sci.*, **56**, 3874–3891.

Durran, D.R., and J.B. Klemp, 1983: A compressible model for the simulation of moist mountain waves. *Mon. Wea. Rev*., **111**, 2341-2361.

Garreaud, R.D., and J.M. Wallace, 1997: The diurnal march of convective cloudiness over the Americas. *Mon. Wea. Rev*., **125**, 3157-3171.

Glickman, T.S., M. Frey, R.G. Hendl, R.T. Podsiadlo, R.C. Taylor, et al. *Glossary of Meteorology, 2nd Edition*. American Meteorological Society*,* 2000.

Gray, W.M., and R.W. Jacobson, Jr., 1977: Diurnal variation of deep cumulus convection. *Mon. Wea. Rev.*, **105**, 1171-1188.

Grossman, R.L., and D.R. Durran, 1984: Interaction of low-level flow with the Western Ghat Mountains and offshore convection in the summer monsoon. *Mon. Wea. Rev.*, **112**, 652-672.

Houze, R.A., Jr., S.G. Geotis, F.D. Marks, Jr., and A.K. West, 1981: Winter monsoon convection in the vicinity of North Borneo. Part I: Structure and time variation of the clouds and precipitation. *Mon. Wea. Rev*., **109**, 1595-1614.

Huffman, G.J., R.F. Adler, P. Arkin, A. Chang, R. Ferraro, A. Gruber, J. Janowiak, A. McNab, B. Rudolf, and U. Schneider, 1997: The Global Precipitation Climatology Project (GPCP) combined precipitation dataset. *Bull. Amer. Meteor. Soc.*, **78**, 5-20.

Imaoka, K., and R.W. Spencer, 2000: Diurnal variation of precipitation over the tropical oceans observed by TRMM/TMI combined with SSM/I. *J. Climate*, **13**, 4149-4158.

Janowiak, J.E., P.A. Arkin, and M. Morrissey, 1994: An examination of the diurnal cycle in oceanic tropical rainfall using satellite and in situ data. *Mon. Wea. Rev*., **122**, 2296-2311.

Kousky, V.E., 1980: Diurnal rainfall variation in northeast Brazil. *Mon. Wea. Rev*., **108**, 488-498.

Kraus, E.B., 1963: The diurnal precipitation change over the sea. *J. Atmo. Sci*., **20**, 546-551.

Krishnamurti, T.N., and Y. Ramanathan, 1982: Sensitivity of the monsoon onset to differential heating. *J. Atmo. Sc*i., **39**, 1290-1306.

Liberti, G.L., F. Cheruy, and M. Desbois, 2001: Land effect on the diurnal cycle of clouds over the TOGA COARE area, as observed from GMS IR data. *Mon. Wea. Rev*., **129**, 1500-1517.

Liu, C., and M.W. Moncrieff, 1998: A numerical study of the diurnal cycle of tropical oceanic convection. *J. Atmo. Sci*., **55**, 2329-2344.

Mapes, B. E., and R. A. Houze Jr., 1993: Cloud clusters and super clusters over the oceanic warm pool. *Mon. Wea. Rev.,* **121,** 1398–1415.

Matsumoto, J., 1992: The seasonal changes in Asian and Australian monsoon regions. *J. Meteor. Soc. Japan*, **70**, 257-273.

Meyer, J.H., 1971: Radar observations of land breeze fronts. *J. Appl. Meteor.*, **10**, 1224-1232.

Mitsumoto, S., H. Ueda, and H. Ozoe, 1983: A laboratory experiment on the dynamics of the land and sea breeze. *J. Atmo. Sci*., **40**, 1228-1240.

Negri, A.J., E.N. Anagnostou, and R.F. Adler, 2000: A 10-yr climatology of Amazonian rainfall derived from passive microwave satellite observations. *J. Appl. Meteor*., **39**, 42-56.

Negri, A.J., R.F. Adler, E.J. Nelkin, and G.J. Huffman, 1994: Regional rainfall climatologies derived from Special Sensor Microwave Imager (SSM/I) data. *Bull. Amer. Meteor. Soc*., **75**, 1165-1182.

Neumann, J., 1951: Land breezes and nocturnal thunderstorms. *J. Meteor*., **8**, 60-67.

Nitta, T., and S. Sekine, 1994: Diurnal variation of convective activity over the tropical western Pacific. *J. Meteor. Soc. of Japan.*, **72**, 627-641.

Oliphant, A.J., A.P. Sturman, and N.J. Tapper, 2001: The evolution and structure of a tropical island sea/land-breeze system, northern Australia. *Meteor. Atmo. Phys*., **78**, 45-59.

Ramage, C.S., 1968: Role of a tropical "maritime continent" in the atmospheric circulation. *Mon. Wea. Rev*., **96**, 365-370.

Randall, D.A., Harshuardhan, and D.A. Dazlich, 1991: Diurnal variability of the hydrologic cycle in a general circulation model. *J. Atmo. Sci*., **48**, 40-62.

Rotunno, R., 1983: On the linear theory of the land and sea breeze. *J. Atmo. Sci*., **40**, 1999-2009.

Schoenberger, L.M., 1984: Doppler radar observation of a land-breeze cold front. *Mon. Wea. Rev.*, **112**, 2456-2464.

Silva Dias, P.L., J.P. Bonatti, and V.E. Kousky, 1987: Diurnally forced tropical tropospheric circulation over South America. *Mon. Wea. Rev*., **115**, 1465-1478.

Sorooshian, S., X. Gao, K. Hsu, R.A. Maddox, Y. Hong, H.V. Gupta, and B. Imam, 2001: Diurnal variability of tropical rainfall retrieved from combined GOES and TRMM satellite information. *J. Climate*, **15**, 983-1001.

Sui, C.-H., K.-M. Lau, Y.N. Takayabu, and D.A.Short, 1997: Diurnal variations in tropical oceanic cumulus convection during TOGA COARE. *J. Atmo. Sci*., **54**, 639-655.

Wang, J.J., R.M. Rauber, H.T. Ochs III, and R.E. Carbone, 1999: The effects of the island of Hawaii on offshore rainband evolution. *Mon. Wea. Rev*., **128**, 1052-1069.

Whiteman, C. David, and Xindi Bian, 1996: Solar semidiurnal tides in the troposphere: detection by radar profilers. *Bull. Amer. Meteor. Soc.*, **77**, 529–542.

Yan, H., and R.A. Anthes, 1987: The effect of latitude on the sea breeze. *Mon. Wea. Rev.*, **115**, 936-956.

Yang, G.-Y., and J. Slingo, 2001: The diurnal cycle in the tropics. *Mon. Wea. Rev*., **129**, 784-801.

Zhong, S., and Eugene S. Takle, 1993: The effects of large-scale winds on the sea-land-breeze circulations in an area of complex coastal heating. *J. Appl. Meteor*., **32**, 1181-1195.

VITA

Kevin Robert Walter is a native of northern Kentucky. In May 2001, he graduated from Thomas More College in Crestview Hills, Kentucky, with a Bachelor's degree in Physics and an Associate's degree in Mathematics. While working on his Master's degree in Atmospheric Sciences at Texas A&M University, he enjoyed participation in the Texas A&M Student Chapter of the American Meteorological Society (TAMSCAMS) and was two-year co-coordinator of Texas A&M Mobile Severe Storms Data Acquisition (TAMMSSDA). On May 29, 2004, he was married in San Antonio, Texas, to Abigail Matlock, a fellow Texas A&M Atmospheric Sciences graduate student. Upon graduation from Texas A&M University in August 2004, Walter will pursue a Ph.D. as an NSF IGERT fellow in the newly formed multi-disciplinary Wind Engineering program at Texas Tech University in Lubbock, Texas. Mr. Walter can be reached at the following address:

Kevin Robert Walter
5639 Dodsworth Lane
Cold Spring, Kentucky 41076